POWER CAPABILITY ESTIMATION ACCOUNTING FOR THERMAL AND ELECTRICAL CONSTRAINTS OF LITHIUM-ION BATTERIES

by

Youngki Kim

A dissertation submitted in partial fulfillment
of the requirements for the degree of
Doctor of Philosophy
(Mechanical Engineering)
in The University of Michigan
2014

Doctoral Committee:

Professor Zoran S. Filipi, Co-Chair
Professor Anna G. Stefanopoulou, Co-Chair
Associate Professor Claus Borgnakke
Assistant Research Scientist Tulga Ersal
Assistant Professor Charles W. Monroe

To my loving family

ACKNOWLEDGEMENTS

First and foremost, I would like to express the deepest gratitude to my advisors, Profs. Zoran Filipi and Anna Stefanopoulou, for their remarkable guidance, encouragement, and support. Prof. Filipi provided me with the opportunity to work on the exciting research topic, hybrid electric vehicles. He always believed in me that I could make it through rough times. Prof. Stefanopoulou introduced me to the new topics on the state-of-the-art lithium-ion batteries. She allowed me freedom to explore various topics in controls and energy systems. She was always willing to provide me with enormously helpful advice.

I am thankful of my committee members, Profs. Claus Borgnakke and Chalse W. Monroe for providing their critical feedback. I truly appreciate their time and effort they volunteered to guide this dissertation work. I believe that their insightful comments have led this dissertation to be more thorough and complete. I would also like to thank the other committee member, Dr. Tulga Ersal, for his excellent questions and constant support throughout the case studies presented at the Annual Automotive Research Center (ARC) conferences.

It has been a pleasure working with all my colleagues in the ARC. Especially, there are several labmates in the past (Hybrid-Z) and the present (Powertrain Control Lab) that I cannot thank enough for their company and ideas - Dr. Tae-Kyung Lee, Dr. Rakesh Patil, Rohit Gupta, William Smith, Dr. Ashwin Salvi, Ingyu Lim, Jihyun Lee, Sungjin Wi, Dr. Jason Siegel, Shankar Mohan, Xinfan Lin, and Boyun Wang.

Very special thanks go to my loving wife, Sunho Yoon. Without her love and support, I would not have completed this Ph.D. journey. Especially, my new-born daughter, Dana, has been one of my sources of inspiration in completing this thesis. I am extremely thankful of my family for their unconditional and perennial support.

Finally, I would like to recognize support from the Automotive Research Center at the University of Michigan, the Rackham Graduate School, and the University of Michigan College of Engineering and Department of Mechanical Engineering.

TABLE OF CONTENTS

LIST OF FIGURES

Figure

LIST OF TABLES

Table

LIST OF APPENDICES

Appendix

ABSTRACT

Power Capability Estimation Accounting for Thermal and Electrical Constraints of Lithium-ion Batteries

by

Youngki Kim

Co-Chairs: Zoran S. Filipi, Anna G. Stefanopoulou

Lithium-ion (Li-ion) batteries have become one of the most critical components in vehicle electrification due to their high specific power and energy density. The performance and longevity of these batteries rely on constraining their operation such that voltage and temperature are regulated within prescribed intervals. Enforcement of constraints on the power capability is a viable solution to protect Li-ion batteries from overheating as well as over-charge/discharge. Moreover, the ability to estimate power capability is vital in formulating power management strategies that account for battery performance limitations while minimizing fuel consumption and emissions.

To estimate power capability accounting for thermal and electrical constraints, the characterization of thermal and electrical system behavior is required. In the course of addressing this problem, first, a computationally efficient thermal model for a cylindrical battery is developed. The solution of the convective heat transfer problem is approximated by polynomials with identifiable parameters that have physical meaning. The parameterized thermal model is shown to accurately predict the measured core and surface temperatures.

The model-based thermal estimation methodology is augmented for cases of unknown cooling conditions. The proposed method is shown with experimental data to accurately provide estimates of the core temperature even under faults in the cooling system.

To jointly account for the thermal and electrical constraints, we utilize time scale separation, and propose a real-time implementable method to predict power capability of a Li-ion battery. The parameterized battery thermal model and estimation

algorithms are integrated into a power management system for a series hybrid electric vehicle. An algorithm for sequential estimation of coupled model parameters and states is developed using sensitivity-based parameter grouping. The fully integrated co-simulation of the battery electro-thermal behavior and the on-line adaptive estimators reveal that the power management system can effectively determine power flow among hybrid powertrain components without violating operational constraints.

CHAPTER I

Introduction

1.1 Motivation

Reducing dependence on imported oil and minimizing vehicular emission are strong motivations to develop a fuel-efficient, clean, and sustainable transportation system. Figure 1.1(a) shows that world crude oil prices have increased considerably over the past years. This trend occurs mostly due to the fact that oil production does not grow and reserves are limited while oil demand grows strongly as the global economy marches towards recovery. The gap between oil supply and demand (Fig. 1.1(b)) will be widened without adequate efforts to reduce the dependence of vehicles on petroleum. While Fig. 1.2(a) shows the numbers of light-duty vehicles in the United States, Fig. 1.2(b) presents similar data from a basket of countries. Even though the number of registered vehicles reached a maximum in 2008 in the U.S., Sivak expects an improving economy and a growing population to lead to continuation of overall trend [1]. Limited oil reserves are a critical factor that may aggregate economic dependence on other oil-supplying countries. Moreover, growing concerns about tailpipe emissions of both pollutants and greenhouse gases, declared a threat to public health and the natural environment by the Environmental Protection Agency (EPA), lead to stringent emissions regulations.

Vehicle electrification, one of the promising technologies for improved fuel economy, tailpipe emissions, and sustainability, has been extensively studied over the past decade. The number of electrified vehicles including hybrid electric vehicles (HEVs), Plug-in hybrid electric vehicles (PHEVs) and Electric Vehicles (EVs) is expected to increase rapidly whereas that of petroleum-based vehicles is expected to decrease [5]. To realize vehicle electrification, various different topologies for hybrid electrified vehicles have been explored; e.g. series [6–9], parallel [10–12], and power split (or series-parallel) [13–15]. Any of these hybrid electric architectures requires an energy

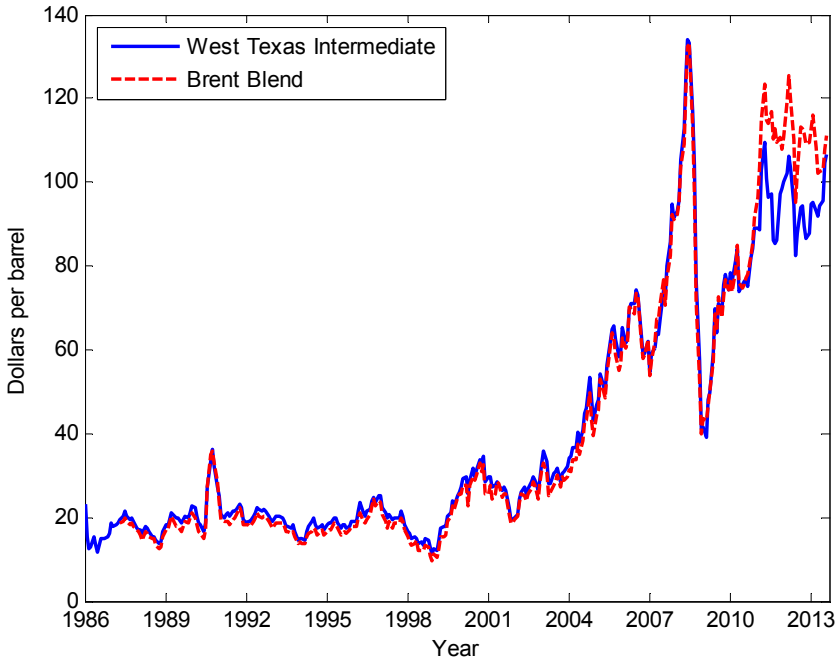

(a)

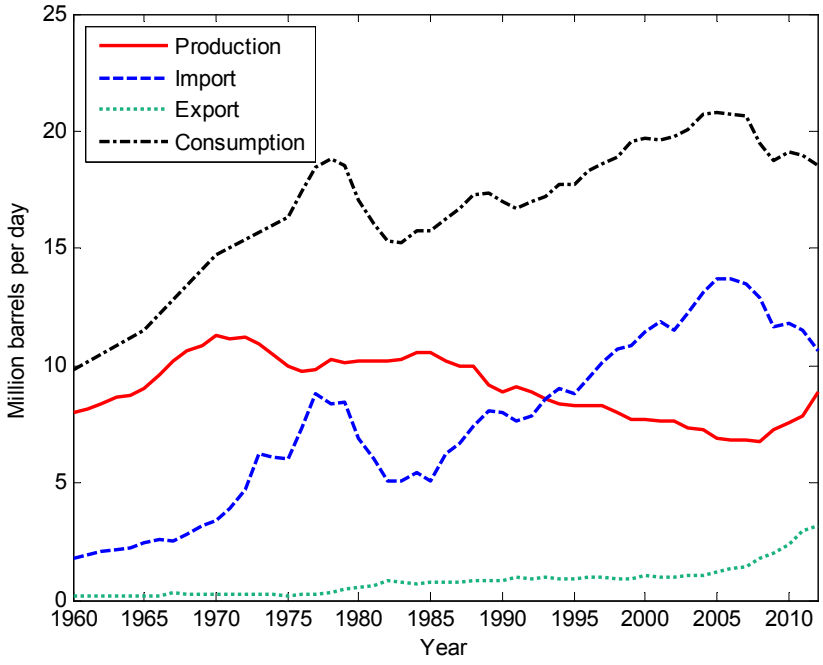

(b)

Figure 1.1: (a) Spot prices for crude oil [2], (b) Petroleum production, import, export, and consumption in United States [3]

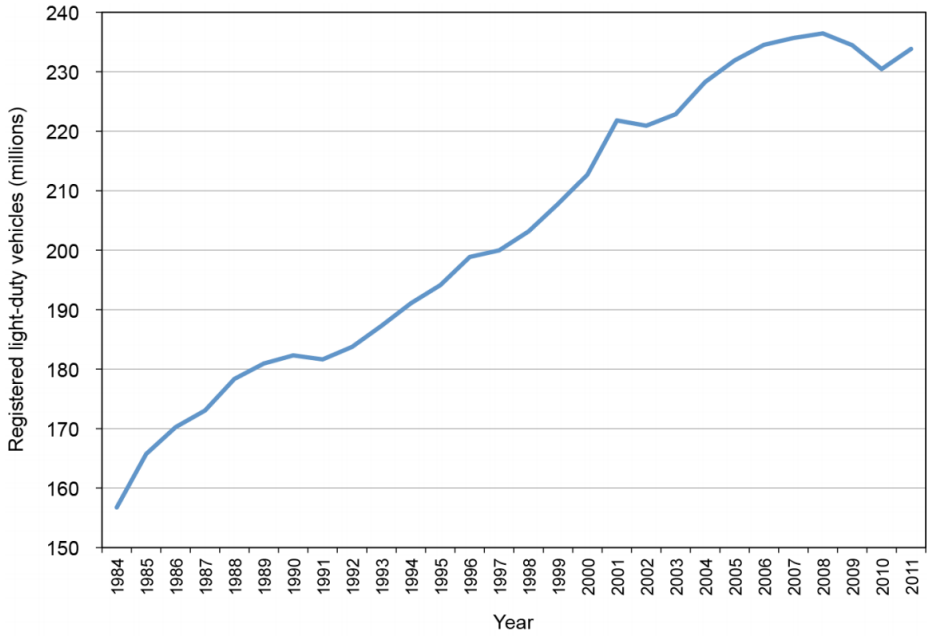

(a)

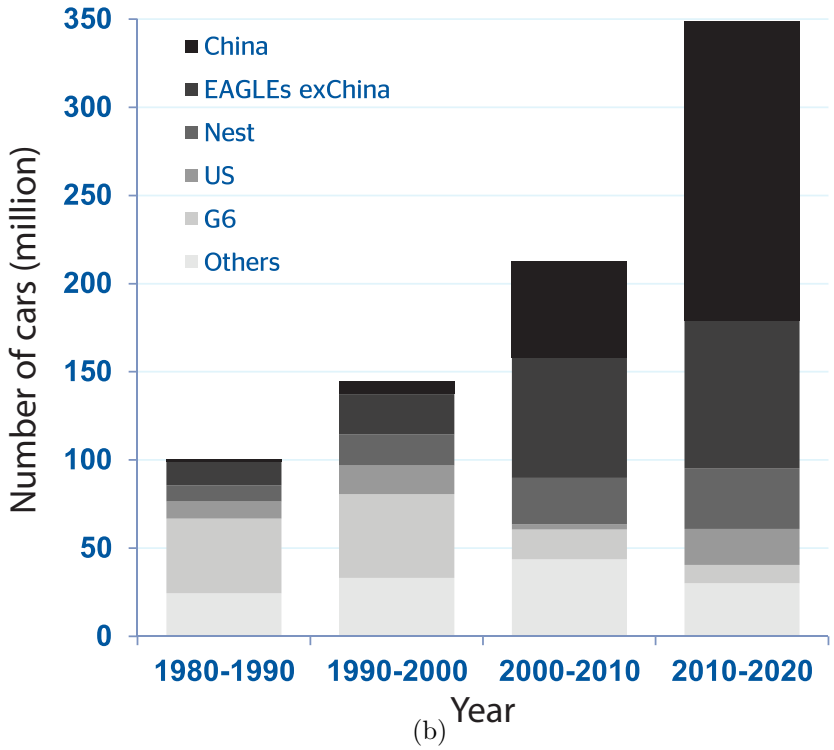

(b)

Figure 1.2: (a) Registered light-duty vehicles in United States from 1984 to 2011 [1], (b) Increase of world car fleet by decades (EAGLEs: Russia, Turkey, Brazil, Mexico, China, India, Indonesia, Korea, Taiwan; Nest: Poland, Ukraine, Argentina, Chile, Colombia, Peru, Bangladesh, Malaysia, Pakistan, Philippines, Thailand, Vietnam, Egypt, Nigeria, S.Africa; G7: France, Germany, Italy, UK, Canada, USA, Japan; Other: Spain, Australia, Iran, S.Arabia [4]

Table 1.1: Typical characteristics of battery technologies [16, 17]

Technology	Specific Energy [Wh/kg]	Energy Density [Wh/L]	Specific Power [W/kg]	Cycle life* [cycles]
Lead-acid	30–50	60–100	200-400	400–800
Ni-Fe	30–55	60–110	25–110	1200–4000
Ni-Zn	60–65	120–130	150–300	100–300
Ni-MH	∼75	∼240	∼1000	750–1200
Li-ion	100-200	100–600	350–1500	1000–4000

* Typical cycle life at deep depth of discharge

storage system and Li-ion batteries have become one of the most critical components over the past decade.

Li-ion batteries have superior performance compared to other battery technologies for applications requiring high rates, high energy density, and deep discharge as shown in Table 1.1. Moreover, Li-ion batteries benefit from minimal memory effects and relatively broad operating temperature ranges [16, 18]. Table 1.2 illustrates that Li-ion batteries have been widely used in the realization of state-of-art of electrified vehicles, such as the Tesla Roadster, Chevrolet Volt, Ford CMAX, etc. However, the Li-ion battery has the drawback that, as shown in Figures 1.3(a) and (b), its cycle life is considerably decreased when operating at high or low temperatures. This presents a problem in automotive applications where high current rates needed for vehicle acceleration cause internal heating of the battery. The battery capacity and the available power decrease considerably during operations at high temperatures due to irreversible chemical reactions [19]. In addition, the performance of the cooling system can degrade generally due to various reasons such as dust on fan blades and heat exchanger, partial blockage in pipes, motor/pump ageing, and motor/pump failure. If cell temperature is not monitored and controlled, a battery can experience a thermal runaway, with the possible risk of explosion [20, 21].

Thus, accurate knowledge of the battery temperature as well as the battery state-of-charge and voltage should be considered in power management for robust vehicle operation.

Table 1.2: Li-ion battery cell/pack specification of electrified vehicles

Type	Vehicle	Positive Electrode Material	Size(mm) /Number	Voltage(V) /Capacity(Ah)	Pack Capacity(kWh)	Cooling Method
EV	Tesla Roadster	$LiCoO_2$	18-65 /6831	3.6 /2.9	53	Liquid
	Tesla Model S	$LiCoO_2$	18-65 /∼5000	3.6 /2.9	60	Liquid
	Daimler Smart	$LiMO_2$	208-248-11 /∼120	3.6 /40	17.6	Liquid /Metal
	Nissan Leaf	$LiMn_2O_4$+$LiMO_2$	290-216-7.1 /192	3.8 /33.1	24	Air
	Mitsubishi i-MiEV	Li_2TiO_3	113.5-171-43.8 /88	3.7 /50	16	Air
PHEV	Chevrolet Volt	$LiMn_2O_4$+$LiMO_2$	162-230-6 /288	3.7 /15	16	Liquid
	Toyota PRIUS Plug-In	$LiMO_2$	148-106-27 /56	3.7 /22	4.6	Air
HEV	Ford CMAX hybrid	$LiMO_2$	120-85-12.7 /76	3.5 /5	1.4	Air

M = Co, Ni, Mn

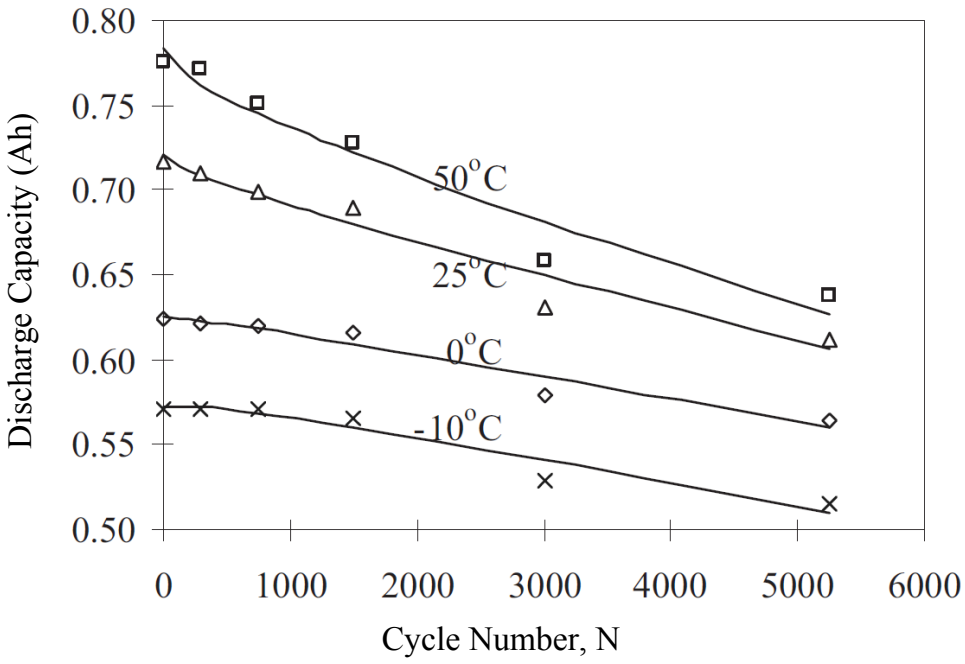

(a)

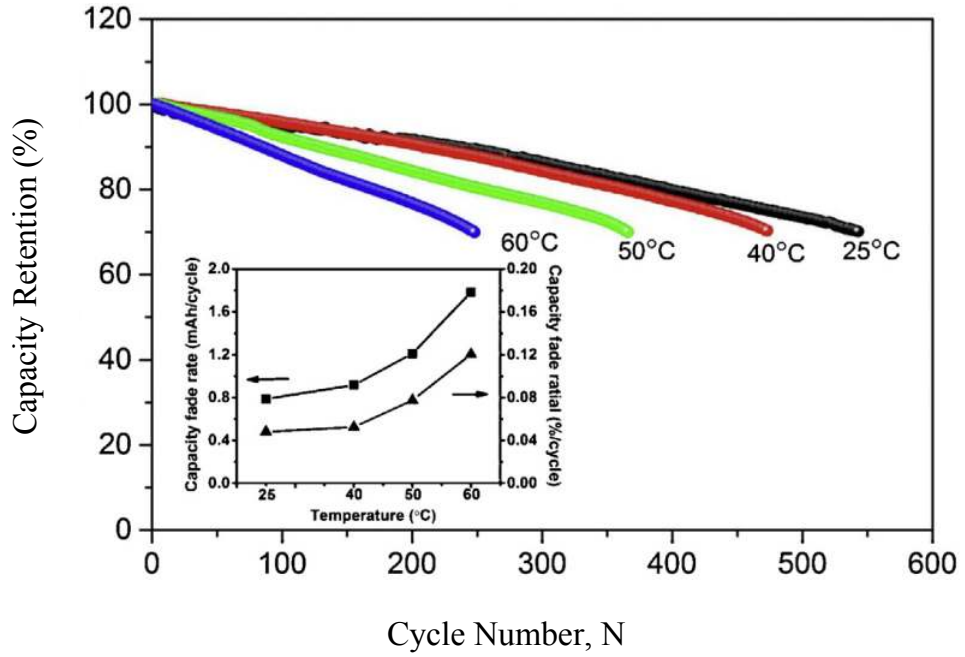

(b)

Figure 1.3: Temperature dependence of cycle life performance of Li-ion batteries: (a) Discharge capacity at different temperatures as a function of cycle number ($LiNi_{0.8}Co_{0.15}Al_{0.05}O_2$/graphite) [22], (b) Discharge curves of a fresh cell from 4.1 to 3.0 V at 1C rate measured at different temperatures ($LiFePO_4$/graphite) [23]

1.2 Battery Models in Literature

The power capability of a battery refers to the constant power that can be drawn safely from the battery over a finite window of time; information on the power capability is critical in making control decisions. In applications such as automotive, aerospace, and robotics, decisions are made by supervisory controllers that manage power or energy flow [24]. Model-based methods to estimate power capability in real-time have been addressed in [25–30] wherein algorithms accounting for electrical and electrochemical constraints such as terminal voltage and battery state-of-charge (SOC) are developed. It is necessary to include temperature as a constraint in the estimation of power capability since battery capacity fade can be accelerated by operation outside battery manufacturers' recommended temperature ranges. Thus, limits on the operating temperatures of Li-ion batteries must be enforced so as to ensure safe and reliable operation.

Temperature regulation can be achieved by using active thermal management systems or limiting the peak current drawn from the batteries. These strategies increase the rate of heat rejection or limit the rate of internal heat generation, respectively [31]. Since Li-ion batteries for applications such as laptop computers, satellites and mobile robots usually have limited cooling, it is critical to control discharge currents so that operating temperatures do not exceed the maximum permissible value. Traditionally, thermostatic or proportional-integral-derivative (PID) controllers are used to limit current or power drawn from the battery when the measured temperature exceeds the predefined limits. However, calibrating thermostatic thresholds, dead-bands, and PID gains and integrating them with the overall power allocation strategies in battery management systems, is a non-trivial problem.

Many approaches have been proposed to predict the electrical and thermal behavior of Li-ion batteries, not only for understanding internal dynamics of the battery system, but also for developing model-based estimation and control algorithms. In this section, a literature review of electrical and thermal modeling along with power capability estimation is presented. First, battery models that capture electrical dynamics are explained. A so-called *electrochemical* model and an *equivalent-circuit* model will be described. Thermal modeling which is used to describe the heat generation in battery systems and the evolution of the temperature distribution within them will be presented.

1.2.1 Electrochemical Model

Electrochemical models are phenomenological in the sense that they rely on parameters that cannot be computationally identified from first principles, but must be characterized experimentally. Fuller *et al.* were the first to develop a detailed Li-ion battery cell model based on porous electrode and concentrated solution theories, Ohm's law, and intercalation kinetics [32]. This pseudo-two-dimensional (P2D) model developed by Fuller *et al.* is useful for understanding the influence of various parameters in transport limitations such as intercalation diffusion or electrolyte conductivity. Ramadass *et al.* extended the Fuller model by providing simple mathematical relations to capture capacity fade, hence enabling the simulation of Li-ion batteries to study degradation in performance as a consequence of aging [33].

Even though the developed model is capable of predicting the instantaneous distribution of lithium, as well as the distributions of potential and current in the solid and liquid phases, computational expense makes the P2D model less attractive in control applications. To reduce the computational burden, Smith *et al.* developed a 12th order control-oriented model from a 313th order nonlinear CFD model by applying a residue grouping-based model reduction [34]. The accuracy of the reduced order model was validated against the CFD model within 1% for pulse and constant current profiles at rates up to 50C. Forman *et al.* used infinite dimensional Páde approximation and quasi-linearization so that the number of states in the P2D model were reduced by 98% without significant sacrifice in accuracy [35]. On the other hand, Ning and Popov applied the single particle (SP) model to Li-ion batteries [36]. The SP model was originally proposed by Haran *et al.* for Nickel Metal Hydride batteries [37]. In the SP model approach, the detailed distribution of concentration in the liquid phase is ignored and the liquid phase potential is simplified. Subramanian *et al.* introduced a high-order polynomial approximation to simplify the solid diffusion dynamics [38], whereas Di Domenico *et al.* used the finite difference method (FDM) with even discretization [39]. Lee *et al.* explored further simplification by uneven discretization while utilizing the SP model with FDM for the battery power management [40, 41]. The SP model requires low computational power, and hence the model is appropriate for real-time applications. However, assumptions and simplifications in the SP model restrict it to low-current operation (e.g. $<$5C). In addition, the identification of a large number of parameters is not an easy task [42].

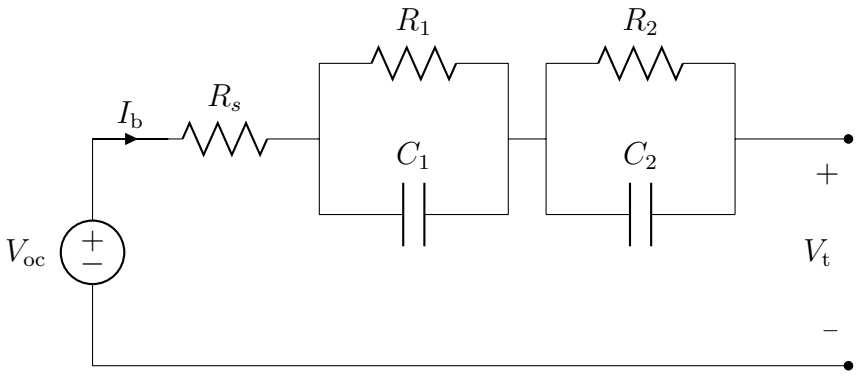

Figure 1.4: An example of the equivalent-circuit model: OCV-R-RC-RC

1.2.2 Equivalent-Circuit Model

Equivalent-circuit models (ECMs), which do not consider fundamental physics, have been widely used to provide relationships between the input and output battery systems while balancing model fidelity and complexity [25, 26, 43–49]. As seen from Fig. 1.4, equivalent-circuit models consist of an open circuit voltage (OCV) included as a voltage source in the circuit, an ohmic resistance and several pairs of parallel resistances and capacitances. Prasad and Rahn showed the explicit relationships between resistances and capacitances and electrochemical parameters of a Li-ion battery [50]. These relationships were derived by investigating the impedance of the Páde approximated Single Particle model. These virtual components are usually parameterized as functions of battery SOC and/or temperature using experimental data. Equivalent-circuit models are computationally efficient, which motivates their use in the development of real-time model-based SOC, state-of-health (SOH) and state-of-power (SOP) estimators and power management strategies for HEVs.

Hu *et al.* compared 12 different equivalent-circuit models of Li-ion batteries from open literature [25, 26, 43–49] in terms of accuracy of voltage prediction [51]. Two typical commercial Li-batteries, namely Sony's $LiCoO_2$/graphite and A123's $LiFePO_4$/graphite, were tested by using standard hybrid vehicle drive cycles. The authors suggested that the inclusion of RC dynamics is critical to improve the voltage prediction but increased model complexity does not necessarily lead to reduced errors.

Therefore, an ECM is used to capture the current-voltage relationship for control-oriented design in this dissertation. In particular, the model's order is chosen to meet the level of accuracy contextually warranted.

- To model the battery as a plant, an OCV-R-RC-RC model is used as parame-

terized in [49].

- To model the battery in development of a state-parameter estimator, an OCV-R-RC model is used as suggested in [51].
- To model the battery in development of a power management strategy, an OCV-R model is used similarly to [11, 30, 52].

1.2.3 Thermal Coupling

The need for an accurate thermal model for Li-ion batteries is significant since the performance, life, and safety are influenced by their temperature. The generation of heat associated with internal resistance of the battery is unavoidable and particularly substantial at high current. In 1985, Bernardi *et al.* presented a general expression for battery heat generation using a thermodynamic energy balance on a single cell, in which they considered the processes relating to electrochemical reactions, phase changes, and mixing [53]. In a simplified form, the equation by Bernardi *et al.* has since been used widely to simulate the thermal response of Li-ion batteries. Thomas and Newman found that the contribution of heat of mixing to total heat generation is small, and that the entropy of reaction accounting for reversible heat effect may be comparable to the Joule heating [54].

Pals and Newman developed a thermal model for both a cell and a cell stack by applying Bernardi's energy balance equation [55, 56]. Smith and Wang studied thermal effects on power capability by neglecting reversible heat since irreversible heat dominates at the high currents (large magnitude) encountered in HEV applications [57]. Guo *et al.* developed a simplified thermal-electrochemical model, in which the SP model was coupled with a simplified energy balance equation [58]. Guo and White used this model to simulate the electrical and thermal behaviors of a satellite battery pack [59].

In the aforementioned modeling approaches, the battery cell is assumed to be isothermal; thus, the spatial temperature distribution within the battery is neglected. This assumption is acceptable for small batteries operating at low rates. However, spatial temperature distribution can be significant for large format cells and high current operation.

To address spatial temperature distribution in a heat transfer problem, Gu and Wang developed a thermal-electrochemical coupled battery model [60]. The porous electrode model was coupled with a lumped thermal model to predict the internal

temperature distribution, as well as the evolution of average cell temperature. Moreover, temperature-dependent physicochemical properties were introduced to couple the thermal model with the models of multiphase mass transport and electrochemical kinetics. In a similar vein, Kumaresan *et al.* applied Gu and Wang's model to simulate the behaviors of $LiCoO_2$/meso-carbon micro-beads (MCMB) pouch cells discharging at different temperatures [61].

Even though physics-based models enable a detailed prediction of the spatial temperature distribution, they are not easy to be implemented in control applications because of computational cost. Thus, much effort has been invested into the development of reduced-order models for prismatic and cylindrical cells with a balance between accuracy and computational cost. In [62], a one-plus-one-dimensional (1+1-D) modeling approach was proposed to solve the thermal dynamics in a prismatic battery; this model was an an extension of the solution to the 1-D spatial heat transfer problem. Muratori *et al.* developed a reduced-order model for a cylindrical battery to predict battery temperatures at core and surface [63]. For model reduction, a balanced truncation method was used to approximate the analytical solution to a heat transfer problem with uniform heat generation in a cylindrical battery. This reduced-order model was validated against a three-dimensional Finite Element Method (FEM). However, this approach has a drawback that an extra calculation for model reduction is required when cooling condition changes. In addition, the states in the reduced-order system do not carry any physical meaning in the original system.

Park and Jaura developed a two-state thermal model using lumped parameters such as thermal capacitance and resistance, and incorporated the lumped-parameter thermal model into an equivalent-circuit battery model [64]. Forgez *et al.* adopted a simplified heat generation equation for a lumped-parameter thermal model and experimentally demonstrated a significant difference between core and surface temperatures in a cylindrical battery cell [65]. Lin *et al.* developed an adaptive observer to estimate unmeasurable core temperatures and battery state-of-health via a lumped-parameter thermal model [66]. This lumped-parameter thermal model is appropriate to design a battery management system (BMS) since low computational power is required. Nevertheless, the assumption that the heat is generated at the core of the battery cell may lead to an overestimation of the core temperature.

Therefore, in this dissertation, a new modeling approach is proposed in Chapter II to derive a reduced-order thermal model for a cylindrical battery by applying polynomial approximation to solve the convective heat transfer problem governed by a partial differential equation.

1.3 Contributions

The contributions in this dissertation and relevant publications are summarized as follows.

In Chapter II, a computationally efficient thermal model for a cylindrical battery is developed. For model reduction, the solution of the convective heat transfer problem is approximated by polynomials. The proposed thermal model with identified thermal properties is shown to accurately predict the core and surface temperatures alongside volume-averaged temperature and volume-averaged temperature gradient of a cylindrical Li-ion battery.

> *Y. Kim, J. B. Siegel, and A. G. Stefanopoulou, "A computationally efficient thermal model of cylindrical battery cells for the estimation of radially distributed temperatures," in Proceedings of the American Control Conference, (Washington, DC, USA), pp. 698-703, Jun 17-19, 2013.*

In Chapter III, a method to estimate the radial temperature distribution inside a cylindrical Li-ion battery under unknown cooling conditions is proposed. The proposed method is shown with experimental data to accurately provide estimates of the core temperature and convection coefficient under uncertain operating conditions.

> *Y. Kim, S. Mohan, J. B. Siegel, A. G. Stefanopoulou, and Y. Ding, "The Estimation of Radial Temperature Distribution in Cylindrical Battery Cells under Unknown Cooling Conditions," IEEE Conference on Decision and Control, (Firenze, Italy), Dec 10-13, 2013*

> *Y. Kim, S. Mohan, J. B. Siegel, A. G. Stefanopoulou, and Y. Ding, "The Estimation of Temperature Distribution in Cylindrical Battery Cells under Unknown Cooling Conditions," Control Systems Technology, IEEE Transactions on, accepted with minor revisions*

In Chapter IV, a real-time implementable method is proposed to compute power capability accounting for thermal and electrical constraints. The proposed method is based on the time scale separation of the electrical and thermal dynamics.

> *Y. Kim, S. Mohan, J. B. Siegel, and A. G. Stefanopoulou, "Maximum Power Estimation of Lithium-ion Batteries Accounting for Thermal and Electrical Constraints," in ASME Dynamic Systems Control Conference, (Palo Alto, CA, USA), Oct 22-24, 2013*

T. Ersal, Y. Kim, J. Broderick, T. Guo, A. Sadrpour, A. Stefanopoulou, J. Siegel, D. Tilbury, E. Atkins, H. Peng, J. Jin and G. Ulsoy, "Keeping Ground Robots on the Move through Better Battery and Mission Management," ASME Dynamic Systems and Control Magazine, submitted

In Chapter V, the proposed battery thermal model and estimation algorithms from the previous chapters are integrated into a power management system for a series hybrid electric vehicle. An algorithm for sequential estimation of coupled model parameters and states is developed. For the electrical system, parameter grouping based on sensitivity is utilized to formulate the state-parameter estimation problem. The estimated states and parameters of the battery are used to compute the maximum allowable power of the battery. The results of the model-in-the-loop simulation reveal that the power management system can effectively determine power flow among hybrid powertrain components without violating operational constraints with information about battery state-of-charge, internal resistance, and power capability.

1.4 Dissertation Organization

This dissertation is organized as follows. Chapter II describes the reduced-order thermal model for a cylindrical battery. The developed model is used for the design of an adaptive estimator in Chapter III. Chapter IV develops a computationally efficient method to predict the power capability of a Li-ion battery accounting for thermal and electrical constraints. A procedure to measure the entropy change of a Li-ion battery and to identify thermal properties is presented. Chapter V discusses a case study – applying the developed battery state-parameter estimation algorithms to a series hybrid electric vehicle. Finally, Chapter VI summarizes the main results of this dissertation, its original contributions, and possible future research directions.

CHAPTER II

Development of a Computationally Efficient Thermal Model of Cylindrical Battery Cells

2.1 Introduction

This chapter presents a computationally efficient thermal model of a cylindrical Li-ion battery for real-time applications. Such a model can be used for thermal management of the battery system in electrified vehicles. The thermal properties are modeled by volume averaged lumped values under the assumption of a homogeneous and isotropic volume. A polynomial approximation is then used to estimate the radial temperature distribution that arises from heat generation inside the cell during normal operation. Unlike previous control oriented models which use discretization of the heat equation, this model formulation uses two states to represent the average value of temperature and its gradient. The model is parameterized and validated using experimental data from a 2.3 Ah 26650 Lithium-Iron-Phosphate ($LiFePO_4$ or LFP) battery cell.

This chapter is organized as follows. Section 2.2 presents the convective heat transfer problem for a cylindrical battery cell. The two-state thermal model using polynomial approximation is addressed. The frequency responses of the transfer function of the proposed model are compared to those of the analytical solution and the numerical solution, showing the accuracy of the proposed model. Then, the lumped thermal properties of the battery, namely the thermal conductivity, the specific heat capacity and the convection coefficient are experimentally identified in Section 2.3. Finally, conclusions are drawn in Section 2.4.

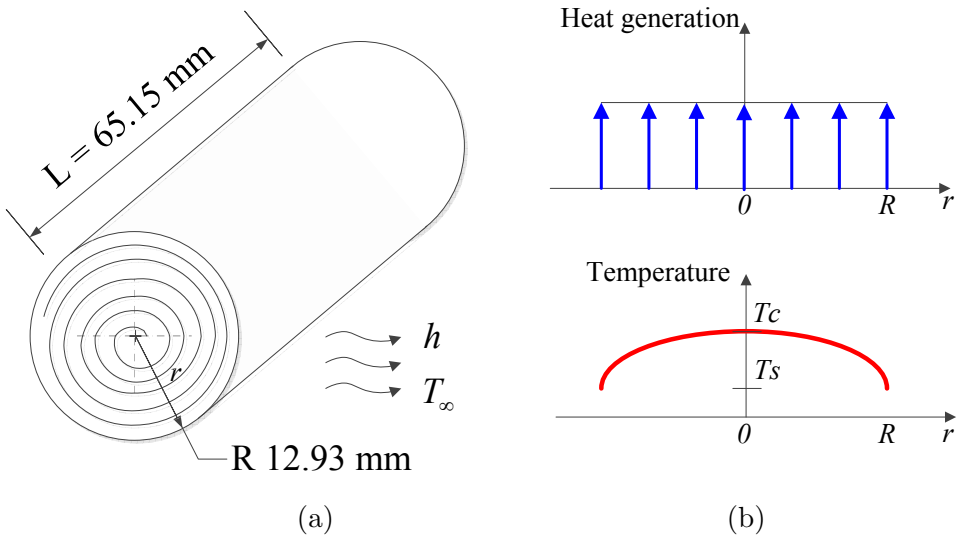

(a) (b)

Figure 2.1: (a) Schematic for a A123 26650 cylindrical battery, (b) parabolic temperature profile under uniform heat generation

2.2 Heat Transfer Problem in Cylindrical Batteries

This section considers the radially distributed one dimensional (1-D) thermal behavior of a cylindrical battery cell with convective heat transfer boundary condition as illustrated in Fig. 2.1(a) [67]. A cylindrical Li-ion battery, a so-called jelly-roll, is fabricated by rolling a stack of cathode/separator/anode layers. The individual layered sheets are thin, therefore, lumped parameters are used so that material properties such as the thermal conductivity k_t, density ρ, and specific heat capacity c_p are assumed to be constant in a homogeneous and isotropic body. For spiral wound current collectors with multiple connections to the battery tab, it is reasonable to assume uniform heat generation along the radial direction as illustrated in Fig. 2.1(b) [68]. The thermal conductivity is one or two orders of magnitude higher in the axial direction than in the radial direction [69]. Therefore, the temperature distribution in the axial direction will be more uniform. The equation that governs the 1-D temperature distribution $T(r,t)$ is

$$\rho c_p \frac{\partial T(r,t)}{\partial t} = k_t \frac{\partial^2 T(r,t)}{\partial r^2} + \frac{k_t}{r}\frac{\partial T(r,t)}{\partial r} + \frac{\dot{q}(t)}{V_\mathrm{b}}, \tag{2.1}$$

and boundary conditions (BCs) are given by

$$\frac{\partial T(r,t)}{\partial r}\Big|_{r=0} = 0, \tag{2.2a}$$

$$\frac{\partial T(r,t)}{\partial r}\Big|_{r=R} = -\frac{h}{k_t}(T(R,t) - T_\infty(t)), \tag{2.2b}$$

where t represents the time. The radius of the battery is R, $\dot{q}$ is the heat generation inside the battery, and V_b is the volume of battery. The ambient temperature for convection is denoted by T_∞. The boundary condition in Eq. (2.2a) represents the symmetric structure of the battery about the core. The other boundary condition shown in Eq. (2.2b) indicates convective heat transfer at the battery surface.

In the following subsections, several approaches to solving PDE (2.2) are presented. Then, a computationally efficient reduced-order model is developed. Specifically, analytical and numerical solutions can be considered as references to be compared to the proposed method.

2.2.1 Analytical Solution

An analytical solution of PDE (2.2) can be obtained by applying a Laplace Transform as suggested in [62]. In the complex domain, the PDE system is converted to an ODE system under the zero initial conditions as following:

$$\frac{d^2\Theta(r,s)}{dr^2} + \frac{1}{r}\frac{d\Theta(r,s)}{dr} - \frac{s}{\alpha}\Theta(r,s) = -\frac{Q(s)}{k_t V_\mathrm{b}}, \tag{2.3a}$$

$$\frac{d\Theta(r,s)}{dr}\Big|_{r=0} = 0, \tag{2.3b}$$

$$\frac{d\Theta(r,s)}{dr}\Big|_{r=R} = -\frac{h}{k_t}\left(\Theta(R,s) - \Theta_\infty(s)\right), \tag{2.3c}$$

where s is the frequency variable in the complex domain and the thermal diffusivity is defined by $\alpha = k_t/\rho c_p$. The variables Θ, Θ_∞ and Q are the transformed battery temperature, ambient temperature, and heat generation rate, respectively.

The homogeneous problem associated with equation (2.3a) is Bessel's equation. The only solution consistent with BC (2.3b) is

$$\Theta(r,s) = CJ_0(\zeta r) + \frac{Q(s)}{k_t V_\mathrm{b}\zeta^2}, \tag{2.4}$$

where J_0 is the 0_th order Bessel function of the first kind. The coefficient C is

determined using Eq. (2.3c):

$$C = \frac{-\dfrac{h}{k_t}\left(\dfrac{Q(s)}{k_t V_\mathrm{b}\zeta^2} + \Theta_\infty(s)\right)}{\dfrac{h}{k_t}J_0(\zeta R) - \zeta J_1(\zeta R)}, \tag{2.5}$$

where $\zeta^2 = s/\alpha$.

Specifically, transfer functions H^a, the frequency responses of the battery at the core and surface to the inputs of heat generation rate and ambient temperature, are given by

$$\begin{bmatrix} \Theta(0,s) \\ \Theta(R,s) \end{bmatrix} = \begin{bmatrix} H^\mathrm{a}_{11} & H^\mathrm{a}_{12} \\ H^\mathrm{a}_{21} & H^\mathrm{a}_{22} \end{bmatrix} \begin{bmatrix} Q(s) \\ \Theta_\infty(s) \end{bmatrix} \tag{2.6}$$

where

$$H^\mathrm{a}_{11} = \frac{\dfrac{h}{k_t}\left(-1 + J_0\left(R\sqrt{\dfrac{s}{\alpha}}\right)\right) - \sqrt{\dfrac{s}{\alpha}}J_1\left(R\sqrt{\dfrac{s}{\alpha}}\right)}{\dfrac{h}{k_t}J_0\left(R\sqrt{\dfrac{s}{\alpha}}\right) - \sqrt{\dfrac{s}{\alpha}}J_1\left(R\sqrt{\dfrac{s}{\alpha}}\right)}\frac{\alpha}{k_t V_\mathrm{b} s} \tag{2.7a}$$

$$H^\mathrm{a}_{12} = \frac{\dfrac{h}{k_t}}{\dfrac{h}{k_t}J_0\left(R\sqrt{\dfrac{s}{\alpha}}\right) - \sqrt{\dfrac{s}{\alpha}}J_1\left(R\sqrt{\dfrac{s}{\alpha}}\right)} \tag{2.7b}$$

$$H^\mathrm{a}_{21} = \frac{-\sqrt{\dfrac{s}{\alpha}}J_1\left(R\sqrt{\dfrac{s}{\alpha}}\right)}{\dfrac{h}{k_t}J_0\left(R\sqrt{\dfrac{s}{\alpha}}\right) - \sqrt{\dfrac{s}{\alpha}}J_1\left(R\sqrt{\dfrac{s}{\alpha}}\right)}\frac{\alpha}{k_t V_\mathrm{b} s} \tag{2.7c}$$

$$H^\mathrm{a}_{22} = \frac{\dfrac{h}{k_t}J_0\left(R\sqrt{\dfrac{s}{\alpha}}\right)}{\dfrac{h}{k_t}J_0\left(R\sqrt{\dfrac{s}{\alpha}}\right) - \sqrt{\dfrac{s}{\alpha}}J_1\left(R\sqrt{\dfrac{s}{\alpha}}\right)} \tag{2.7d}$$

It is noted that these transfer functions are not algebraic but transcendental. Therefore, a model reduction technique is required to extract a finite number of states to predict thermal behaviors of the battery in time domain. A balanced truncation method is applied for model reduction in [62] where Muratori *et al.* showed the accuracy of the model in comparison with results from the numerical method, namely Finite Element Method. Nevertheless, this model has two drawbacks that make it

difficult to be used in real-time application: (1) extra calculation for model reduction is required when cooling condition changes, (2) the states of the reduced-order model do not have physical meanings. This analytical solution is used to validate the proposed reduced-order model presented in Section 2.2.3.

2.2.2 Numerical Solution: Finite Difference Method

The PDE (2.2) with its initial conditions can be also numerically solved to predict the temperature distribution in the battery using the finite difference method. By dividing the radius of the cylindrical battery in N intervals (or, $N+1$ nodes) with the incremental size of $\Delta r = R/N$, the first and the second partial derivatives in the PDE at i_{th} node can be approximated with the finite difference equations as following:

$$\frac{\partial T_i}{\partial r} = \frac{T_{i+1} - T_{i-1}}{2\Delta r}, \tag{2.8a}$$

$$\frac{\partial^2 T_i}{\partial r^2} = \frac{T_{i-1} - T_i + T_{i+1}}{\Delta r^2}, \tag{2.8b}$$

where $i \in \{1, 2, \ldots, N-1\}$.

By substituting Eq. (2.8) into the PDE (2.2), the heat transfer problem at i_{th} node can be expressed by

$$\frac{dT_i}{dt} = \frac{\alpha}{(\Delta r)^2} \frac{(2i-1)T_{i-1} - 4iT_i + (2i+1)T_{i+1}}{2i} + \frac{\alpha}{k_t V_{\text{b}}} \dot{q}. \tag{2.9}$$

Using symmetric and convective boundary conditions, temperatures at the core ($i = 0$) and the surface ($i = N$) are described by

$$T_0 = T_1, \tag{2.10a}$$

$$T_N = \frac{k_t T_{N-1} + h\Delta r T_\infty}{k_t + h\Delta r}. \tag{2.10b}$$

Finally, a set of ordinary differential equations to predict the temperature distribution in the battery is generated using Eqs. (2.9) and (2.10) as given by

$$\dot{\vartheta} = A_n \vartheta + B_n u \tag{2.11a}$$

$$y_n = C_n \vartheta + D_n u \tag{2.11b}$$

where $\vartheta = [T_1\, T_2\, \ldots T_{N-1}]^T$, $u = [\dot{q}\, T_\infty]^T$ and $y_n = [T_0\, T_N]^T$ are states, inputs and outputs, respectively.

System matrices are defined as following:

$$A_n = \xi_1 \begin{bmatrix} -\frac{3}{2} & \frac{3}{2} & 0 & \dots & \dots & 0 \\ \frac{3}{4} & -2 & \frac{5}{4} & 0 & \dots & \vdots \\ \vdots & \ddots & \ddots & \ddots & \dots & 0 \\ \vdots & \dots & 0 & \frac{2N-5}{2(N-2)} & -2 & \frac{2N-3}{2(N-2)} \\ 0 & \dots & \dots & 0 & \frac{2N-3}{2(N-1)} & -2+\frac{2N-1}{2(N-1)}\xi_1 \end{bmatrix}, \tag{2.12a}$$

$$B_n = \xi_2 \begin{bmatrix} 1 & \dots & \dots & 1 \\ 0 & \dots & 0 & \frac{2N-1}{2(N-1)}\frac{\xi_4}{\xi_2} \end{bmatrix}^T, \tag{2.12b}$$

$$C_n = \begin{bmatrix} 1 & 0 & \dots & 0 \\ 0 & \dots & 0 & \xi_3 \end{bmatrix}, \tag{2.12c}$$

$$D_n = \begin{bmatrix} 0 & \dots & \dots & 0 \\ 0 & \dots & 0 & \xi_4 \end{bmatrix}^T, \tag{2.12d}$$

where $\xi_1 = \dfrac{\alpha}{(\Delta r)^2}$, $\xi_2 = \dfrac{\alpha}{k_t V_b}$, $\xi_3 = \dfrac{k_t}{k_t + h\Delta r}$ and $\xi_4 = \dfrac{h\Delta r}{k_t + h\Delta r}$.

Therefore, transfer functions H^{n}, frequency responses of the battery core and its surface to inputs from the numerical solution, can be obtained by

$$H^{\mathrm{n}}(s) = C_n(sI - A_n)^{-1}B_n + D_n. \tag{2.13}$$

where the variable I is the identity matrix.

For a sufficiently large number of discretization N, it is expected that frequency responses from the numerical method converge to analytical solutions'

$$\lim_{N\to\infty} H^{\mathrm{n}}_{ij}(s) \approx H^{\mathrm{a}}_{ij}(s), \tag{2.14}$$

where $i, j \in \{1, 2\}$.

Unlike the reduced-order model obtained from the analytical solution, no extra calculation are required and the influence of change in parameters can be predicted since system matrices are computed using physical parameters. Nevertheless, a large number of states makes this model challenging to be implemented in real-time application. These drawbacks can be resolved by the computationally efficient model proposed in the following section.

2.2.3 Model Reduction via Polynomial Approximation

With evenly distributed heat generation, the temperature distribution along r-direction of the battery is assumed to satisfy the following polynomial approximation proposed in [38]

$$T(r,t) = a(t) + b(t)\left(\frac{r}{R}\right)^2 + d(t)\left(\frac{r}{R}\right)^4, \tag{2.15}$$

where $a(t)$, $b(t)$, and $d(t)$ are time-varying coefficients. To satisfy the symmetric boundary condition at the core of the battery, Eq. (2.15) contains only even powers of r. Thus, the temperatures at the core and the surface of the battery can be expressed as

$$T_{\mathrm{c}} = a(t), \tag{2.16a}$$

$$T_{\mathrm{s}} = a(t) + b(t) + d(t), \tag{2.16b}$$

where subscripts c and s denote core and surface, respectively.

The volume-averaged temperature $\bar{T}$ and temperature gradient $\bar{\gamma}$ are introduced as follows:

$$\bar{T} = \frac{2}{R^2}\int_0^R rT\,dr, \tag{2.17a}$$

$$\bar{\gamma} = \frac{2}{R^2}\int_0^R r\left(\frac{\partial T}{\partial r}\right)dr. \tag{2.17b}$$

These volume-averaged values are used as the states unlike existing approaches in [64], [65], and [66].

By substituting Eq. (2.15) into Eq. (2.17), $\bar{T}$ and $\bar{\gamma}$ can be expressed in terms of coefficients as

$$\bar{T}(t) = a(t) + \frac{b(t)}{2} + \frac{d(t)}{4}, \tag{2.18a}$$

$$\bar{\gamma}(t) = \frac{4b(t)}{3R} + \frac{8d(t)}{5R}. \tag{2.18b}$$

By rearranging Eqs. (2.16) and (2.18), time-varying coefficients $a(t)$, $b(t)$, and

$d(t)$ can be written as

$$a(t) = 4T_{\mathrm{s}} - 3\bar{T} - \frac{15R}{8}\bar{\gamma}, \tag{2.19a}$$

$$b(t) = -18T_{\mathrm{s}} + 18\bar{T} + \frac{15R}{2}\bar{\gamma}, \tag{2.19b}$$

$$d(t) = 15T_{\mathrm{s}} - 15\bar{T} - \frac{45R}{8}\bar{\gamma}. \tag{2.19c}$$

The temperature distribution can be expressed as a function of T_{s}, $\bar{T}$, and $\bar{\gamma}$ using Eqs. (2.19) in Eq. (2.15),

$$\begin{aligned} T(r,t) = 4T_{\mathrm{s}} - 3\bar{T} - \frac{15R}{8}\bar{\gamma} + \left[-18T_{\mathrm{s}} + 18\bar{T} + \frac{15R}{2}\bar{\gamma}\right]\left(\frac{r}{R}\right)^2 \\ + \left[15T_{\mathrm{s}} - 15\bar{T} - \frac{45R}{8}\bar{\gamma}\right]\left(\frac{r}{R}\right)^4. \end{aligned} \tag{2.20}$$

By substituting Eq. (2.20) into the following volume-averaged equations,

$$\int_0^R \left(\rho c_p \frac{\partial T(r,t)}{\partial t} - k_t \frac{\partial^2 T(r,t)}{\partial r^2} - \frac{k_t}{r}\frac{\partial T(r,t)}{\partial r} - \frac{\dot{q}(t)}{V_{\mathrm{b}}}\right) dr = 0, \tag{2.21a}$$

$$\int_0^R \frac{\partial}{\partial r}\left(\rho c_p \frac{\partial T(r,t)}{\partial t} - k_t \frac{\partial^2 T(r,t)}{\partial r^2} - \frac{k_t}{r}\frac{\partial T(r,t)}{\partial r} - \frac{\dot{q}(t)}{V_{\mathrm{b}}}\right) dr = 0, \tag{2.21b}$$

PDE (2.1) can be converted into two ODEs expressed as

$$\frac{d\bar{T}}{dt} + \frac{48\alpha}{R^2}\bar{T} - \frac{48\alpha}{R^2}T_{\mathrm{s}} + \frac{15\alpha}{R}\bar{\gamma} - \frac{\alpha}{k_t V_{\mathrm{b}}}\dot{q} = 0, \tag{2.22a}$$

$$\frac{d\bar{\gamma}}{dt} + \frac{320\alpha}{R^3}\bar{T} - \frac{320\alpha}{R^3}T_{\mathrm{s}} + \frac{120\alpha}{R^2}\bar{\gamma} = 0. \tag{2.22b}$$

Using boundary condition (2.2b), the surface temperature T_{s} can be rewritten as

$$T_{\mathrm{s}} = \frac{24k_t}{24k_t + Rh}\bar{T} + \frac{15k_t R}{48k_t + 2Rh}\bar{\gamma} + \frac{Rh}{24k_t + Rh}T_\infty. \tag{2.23}$$

Finally, a two-state thermal model can be given by the following form:

$$\frac{dx}{dt} = Ax + Bu, \tag{2.24a}$$

$$y = Cx + Du, \tag{2.24b}$$

where $x = [\bar{T}\ \bar{\gamma}]^T$, $u = [\dot{q}\ T_\infty]^T$ and $y = [T_\mathrm{c}\ T_\mathrm{s}]^T$ are states, inputs and outputs respectively. System matrices A, B, C, and D are defined as follows:

$$A = \begin{bmatrix} \dfrac{-48\alpha h}{R(24k_t + Rh)} & \dfrac{-15\alpha h}{24k_t + Rh} \\ \dfrac{-320\alpha h}{R^2(24k_t + Rh)} & \dfrac{-120\alpha(4k_t + Rh)}{R^2(24k_t + Rh)} \end{bmatrix}, \tag{2.25a}$$

$$B = \begin{bmatrix} \dfrac{\alpha}{k_t V_\mathrm{b}} & \dfrac{48\alpha h}{R(24k_t + Rh)} \\ 0 & \dfrac{320\alpha h}{R^2(24k_t + Rh)} \end{bmatrix}, \tag{2.25b}$$

$$C = \begin{bmatrix} \dfrac{24k_t - 3Rh}{24k_t + Rh} & -\dfrac{120Rk_t + 15R^2h}{8(24k_t + Rh)} \\ \dfrac{24k_t}{24k_t + Rh} & \dfrac{15Rk_t}{48k_t + 2Rh} \end{bmatrix}, \tag{2.25c}$$

$$D = \begin{bmatrix} 0 & \dfrac{4Rh}{24k_t + Rh} \\ 0 & \dfrac{Rh}{24k_t + Rh} \end{bmatrix}. \tag{2.25d}$$

This state-space representation is used for the parametrization in Section 2.3 and the estimation of the core temperature and convection coefficient using Kalman Filters in Chapter III.

2.2.4 Frequency Domain Analysis

The frequency response functions of the reduced-order model, $H^\mathrm{p}(s) = D + C(sI - A)^{-1}B$, are compared to those of the analytical solution and the finite difference method with N=30, i.e. Eqs. (2.6) and (2.13), respectively. Parameters used to generate the plots in Fig. 2.2 are adopted from [62] and are summarized in Table 2.1. The heat transfer coefficient of h=5W/m^2/K is chosen since this value is typical of natural convection condition [70].

Figure 2.2 shows that the effects of heat generation on the core and the surface temperatures, denoted by $H^\mathrm{p}_{11}(s)$ and $H^\mathrm{p}_{21}(s)$ respectively, can be accurately predicted over the whole range of frequency. On the other hand, the responses of the core and the surface temperatures excited by the ambient temperature, $H^\mathrm{p}_{12}(s)$ and $H^\mathrm{p}_{22}(s)$, are nearly identical to the analytical solution for frequencies below 10^{-2} Hz. In general, the temperature of cooling media does not change rapidly. Thus, the prediction of temperature distribution using the proposed approach can be considered sufficiently accurate.

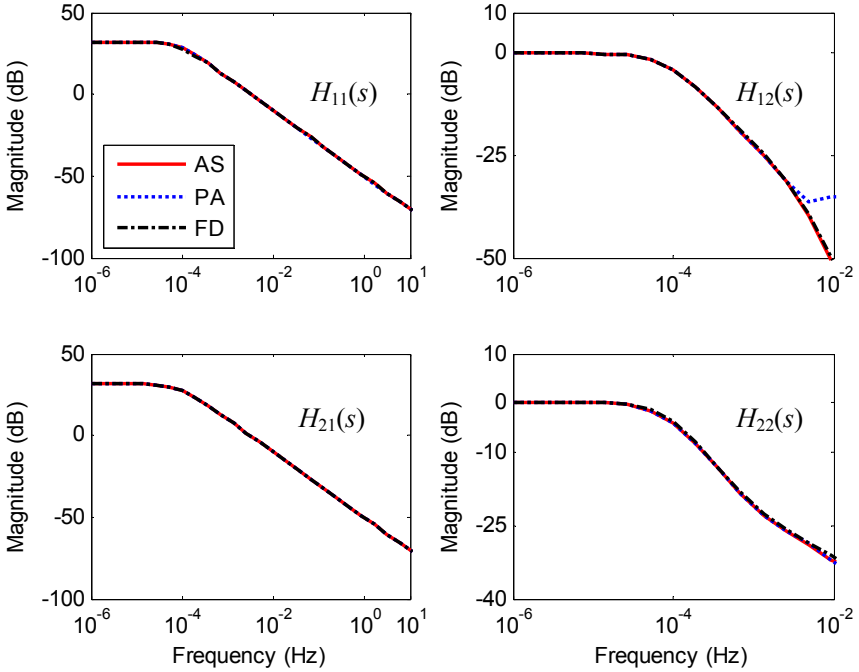

(a)

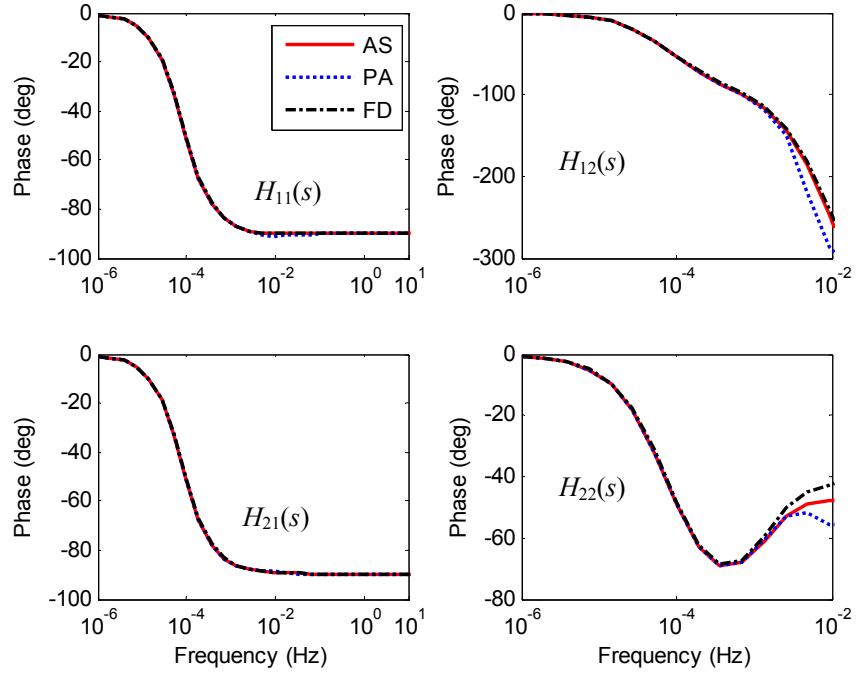

(b)

Figure 2.2: Comparison of frequency response functions obtained by analytical solution (AS), polynomial approximation (PA), and finite difference method (FD): (a) magnitude, (b) phase

Table 2.1: Parameters of the battery [62]

Parameter	Symbol	Value	Unit
Density	ρ	1824	kg/m^3
Specific heat coeff.	c_p	825	J/kg/K
Thermal conductivity	k_t	0.488	W/m/K
Convection coeff.	h	5	W/m^2/K
Radius	R	12.93e-3	m
Height	L	65.15e-3	m
Volume	V_b	3.4219e-5	m^3

2.2.5 Heat Generation Calculation

Heat generation $\dot{q}$ is the main input to the battery thermal model. It needs to be accurately calculated from measurement data, such as current and voltage during operation. From the first law of thermodynamics, the energy balance equation is written as

$$\frac{dH}{dt} = \dot{q}_\mathrm{sur} - I_\mathrm{b} V_\mathrm{t}, \tag{2.26}$$

where H is the enthalpy, $\dot{q}_\mathrm{sur}$ is the heat added from surroundings, I_b is the current, and V_t is the terminal voltage. The term $I_\mathrm{b}V_\mathrm{t}$ denotes the rate of electrical work.

In [53], Bernardi *et al.* proposed a simplified energy balance equation considering enthalpy change associated with electrochemical reactions. Under assumptions such as isothermal body, constant system volume and pressure, and neglecting heat generation due to enthalpy-of-mixing and phase-change, the energy balance equation is expressed as

$$Mc_p \frac{dT}{dt} = \dot{q} + \dot{q}_\mathrm{sur}, \tag{2.27a}$$

$$\dot{q} = I_\mathrm{b}(V_\mathrm{oc} - T\frac{\partial V_\mathrm{oc}}{\partial T}) - I_\mathrm{b}V_\mathrm{t}, \tag{2.27b}$$

where V_oc represents the open-circuit voltage (OCV). The OCV is a function of the battery state-of-charge (SOC) and temperature. As shown in Fig 2.3, the OCV at room temperature, i.e. 25°C, is experimentally obtained by averaging the measured terminal voltages during charging and discharging a battery with C/20[1] current rate

[1]A 1C current corresponds to the magnitude of current that discharges/charges the battery completely in one hour.

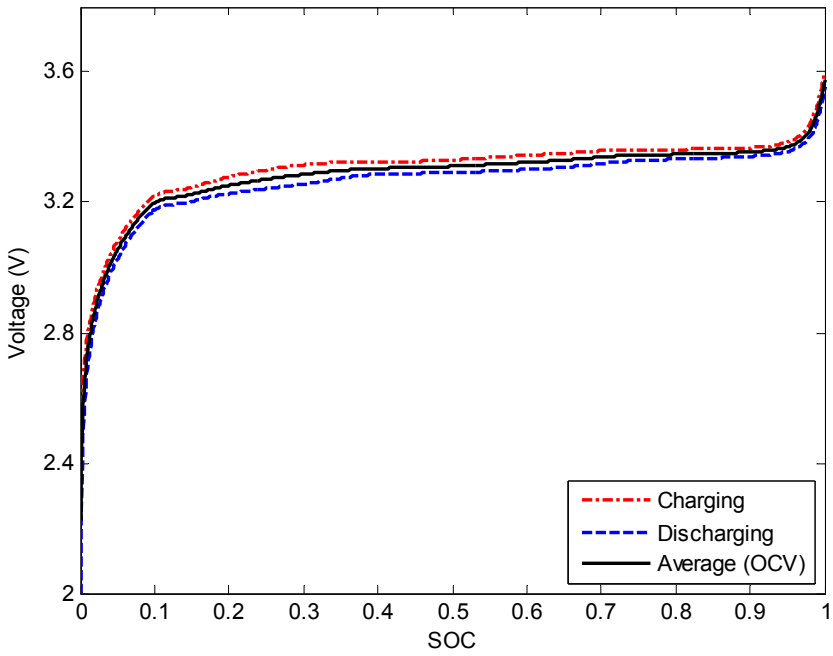

Figure 2.3: Open Circuit Voltage of a 2.3 Ah 26650 LFP battery approximately obtained by averaging terminal voltages during charging and discharging a battery with C/20 rate at room temperature

under a Constant Current Constant Voltage (CCCV) charging protocol. The OCV is then calculated at the estimated SOC value by integrating measured current with respect to time as

$$\dot{\mathrm{SOC}} = -\frac{I_\mathrm{b}}{3600 C_\mathrm{b}}, \tag{2.28}$$

where C_b is the battery capacity in Ah. The sign convention is such that positive current denotes battery discharging.

The term $I_\mathrm{b} T \frac{\partial V_\mathrm{oc}}{\partial T}$ is the reversible heat generation and can be calculated simply from the entropy of reaction [71]. In this study, this reversible heat generation is neglected for simplicity. This simplification is warranted since the typical SOC range of HEV operation is narrow in which $\frac{\partial V_\mathrm{oc}}{\partial T}$ of the battery is insignificant as shown in [65] for this chemistry. In addition, the reversible heat generation would have zero mean value when the battery is operating in charge-sustaining mode, typical of HEV operation; the OCV becomes a function of battery SOC only.

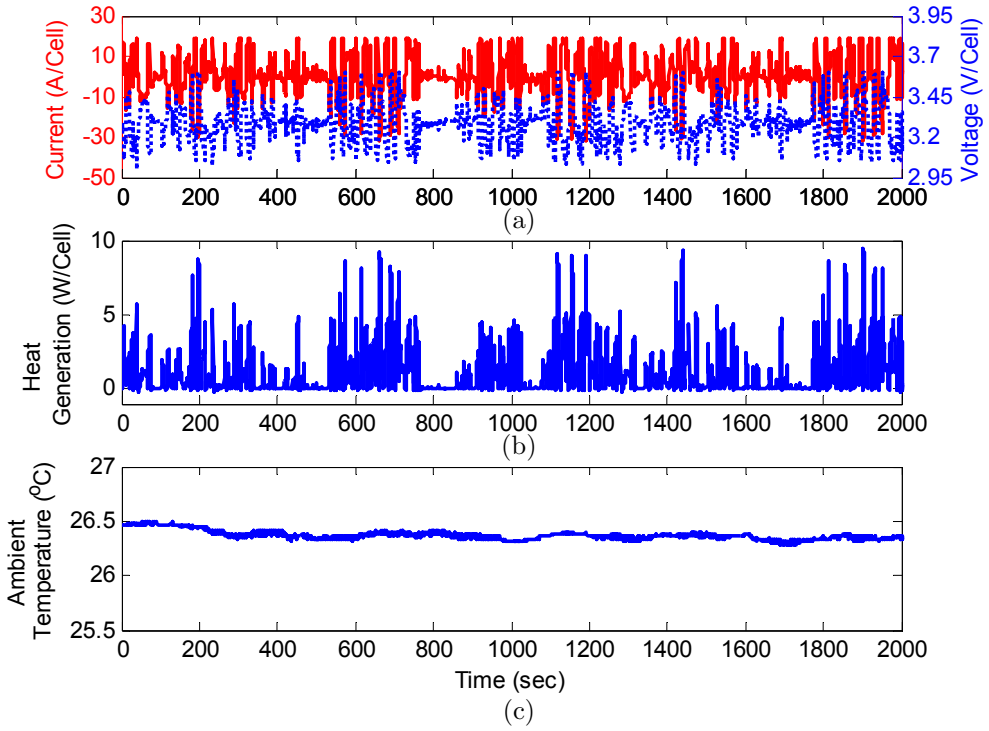

Figure 2.4: Data set during Urban-Assault Cycle used for parameter ID: (a) current and voltage, (b) heat generation rate, (c) ambient temperature

2.3 Parameter Identification

In this section, the value of the lumped parameters in Eq. (2.24) for a 2.3 Ah 26650 LFP battery by A123 are identified through experimentation using the proposed model. Figure 2.4 shows the current, the voltage, the calculated heat generation rate and the ambient temperature profiles over the Urban-Assault Cycle (UAC) in [66] that is used for the parametrization. It is noted that this cycle used for simulating military ground vehicles has significantly high power demands. The parameterized model is then validated using measurement data over a different HEV driving cycle.

2.3.1 Identifying Thermal Properties

Parameter identification is important for accurately predicting the temperature distribution inside a battery. Since density is measurable, only three parameters, namely k_t, c_p, and h are considered for parameter identification, i.e. $\theta = [k_t,\, c_p,\, h]^T$.

To study the feasibility of accurately estimating the parameters, as a first step, identifiability analysis is performed. Parameters in a model are *structurally* identifiable if and only if a unique set of parameters for the model is determined using perfect noise-free data [72]. In this study, the linearization approach proposed by

Ben-Zvi [73] is used for its computational efficiency compared to other methods such as Taylor series expansion [74] and Generating series [75].

The transfer function of the reduced-order model, $H^{\mathrm{p}}(s)$, is defined as follows:

$$H^{\mathrm{p}}(s) = \begin{bmatrix} H^{\mathrm{p}}_{11}(s) & H^{\mathrm{p}}_{12}(s) \\ H^{\mathrm{p}}_{21}(s) & H^{\mathrm{p}}_{22}(s) \end{bmatrix}. \tag{2.29}$$

Each transfer function is expressed in the following fractional form:

$$H^{\mathrm{p}}_{11}(s) \triangleq \frac{T_{\mathrm{c}}(s)}{Q(s)} = \frac{\kappa_4 s + \kappa_5}{\kappa_1 s^2 + \kappa_2 s + \kappa_3}, \tag{2.30a}$$

$$H^{\mathrm{p}}_{21}(s) \triangleq \frac{T_{\mathrm{s}}(s)}{Q(s)} = \frac{\kappa_6 s + \kappa_7}{\kappa_1 s^2 + \kappa_2 s + \kappa_3}, \tag{2.30b}$$

$$H^{\mathrm{p}}_{12}(s) \triangleq \frac{T_{\mathrm{c}}(s)}{T_{\infty}(s)} = \frac{\kappa_8 s^2 + \kappa_9 s + \kappa_{10}}{\kappa_1 s^2 + \kappa_2 s + \kappa_3}, \tag{2.30c}$$

$$H^{\mathrm{p}}_{22}(s) \triangleq \frac{T_{\mathrm{s}}(s)}{Q_{\infty}(s)} = \frac{\kappa_{11} s^2 + \kappa_{12} s + \kappa_{10}}{\kappa_1 s^2 + \kappa_2 s + \kappa_3}, \tag{2.30d}$$

where

$$\kappa_1 = V_{\mathrm{b}} k_t R^3 (hR + 24k_t), \tag{2.31a}$$

$$\kappa_2 = 24 V_{\mathrm{b}} \alpha R (7hR + 20k_t), \tag{2.31b}$$

$$\kappa_3 = 960 V_{\mathrm{b}} \alpha^2 k_t h, \tag{2.31c}$$

$$\kappa_4 = 3\alpha R^3 (8k_t - hR), \tag{2.31d}$$

$$\kappa_5 = 240 \alpha^2 R (hR + 2k_t), \tag{2.31e}$$

$$\kappa_6 = 24 \alpha k_t R^3, \tag{2.31f}$$

$$\kappa_7 = 480 \alpha^2 k_t R, \tag{2.31g}$$

$$\kappa_8 = 4 V_{\mathrm{b}} \alpha k_t h R^4, \tag{2.31h}$$

$$\kappa_9 = -72 V_{\mathrm{b}} \alpha k_t h R^2, \tag{2.31i}$$

$$\kappa_{10} = 960 V_{\mathrm{b}} \alpha^2 k_t h, \tag{2.31j}$$

$$\kappa_{11} = V_{\mathrm{b}} k_t h R^4, \tag{2.31k}$$

$$\kappa_{12} = 168 V_{\mathrm{b}} \alpha k_t h R^2. \tag{2.31l}$$

Define a vector of coefficients, Φ, as follows:

$$\Phi(\theta) = [\kappa_1(\theta) \;\; \kappa_2(\theta) \; \cdots \kappa_{12}(\theta)]. \tag{2.32}$$

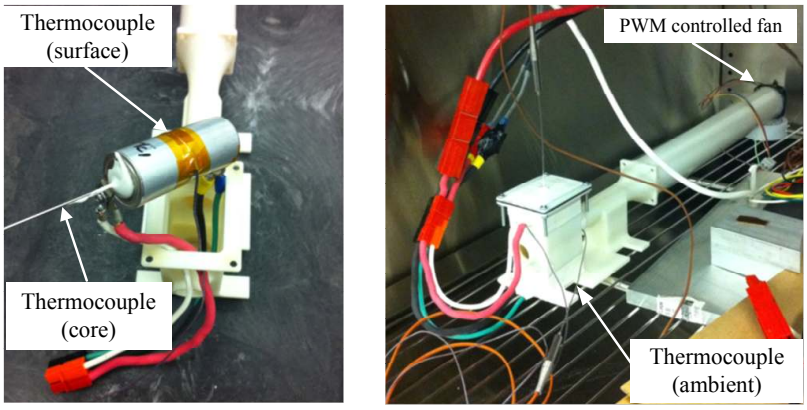

Figure 2.5: Experimental setup for temperature measurement

The rank of the Jacobian of Φ with respect to parameter θ is used to determine if all the elements of θ are identifiable. If and only if the Jacobian of Φ is full rank, then all elements of θ are said to be identifiable. The rank of $\frac{\partial \Phi(\theta)}{\partial \theta}$ is found be to three which is the same as $\dim(\theta)$. Therefore, it can be concluded that parameters of the thermal model are *structurally* identifiable.

Having established identifiability, experiments similar to [66] are conducted to identify parameters. An experimental set-up is shown in Fig. 2.5. Measured signals such as the current, the terminal voltage, the surface and the core temperatures of the battery along with the ambient temperature are used for the parameter identification. Thermocouples used for temperature measurements are T-type whose accuracy is the maximum of 0.5°C or 0.4% according to technical information from the manufacturer, OMEGA. Specifically, convection coefficient h is controlled by the fan speed based on Pulse Width Modulation (PWM) control and ambient temperature inside the thermal chamber.

Let the error between the measured temperatures and model outputs at each time step k in vector form be

$$e(k,\theta) = [T_{\mathrm{c,p}}(k,\theta) \;\; T_{\mathrm{s,p}}(k,\theta)]^T - [T_{\mathrm{c,m}}(k) \;\; T_{\mathrm{s,m}}(k)]^T, \tag{2.33}$$

where subscripts p and m denote model prediction and measurement, respectively. The battery is allowed to rest at ambient temperature to equilibrate; that is, $x(0) = [T_\infty \; 0]^T$.

Parameters are identified by minimizing the Euclidean norm of the difference

Table 2.2: Identified thermal properties

Parameter	Symbol	Value	Reference
Density	ρ	2047*	2118 [76]
Specific heat capacity	c_p	1109.2	1004.9–1102.6 [65, 66]
Thermal conductivity	k_t	0.610	0.488–0.69 [62, 76]
Convection coefficient.	h	58.6	65.99 [66]

* calculated using measured mass and volume

between the measured and simulated temperatures as given by

$$\theta^* = arg\min_{\theta} \sum_{k=1}^{N_f} ||e(k,\theta)||_2, \tag{2.34}$$

where N_f is the number of measurement points. The minimization problem is solved by using the *fmincon* function in MATLAB. The parameters in Table 2.1 are used as initial guesses for the identification.

Table 2.2 presents the identified thermal properties for the 26650 battery. These identified values of the parameters are close to the values reported in the literature. The identified specific heat capacity c_p is five percent larger than the mean value determined in [65] where c_p was determined by measuring transient responses of the battery under current pulses at different rates. Forgez *et al.* in [65] suggested that the deviation in identified value of c_p might be caused by measurement uncertainty in temperature and the temperature dependency of the heat capacity. The identified thermal conductivity k_t is within the range of values presented in literature [62, 76].

Despite using similar experimental data and setup, the identified convection coefficient is 11% smaller than the coefficient calculated by using thermal resistance and battery surface area in [66]. This difference between our identified value and the one in [66] may be due to the two different model structures. Lin *et al.* in [66] considered two different materials, namely one for the core and the other for the surface, whereas we assume the battery is a homogeneous and isotropic body. In order to accurately determine the convection coefficient, the temperature measurements of a pure metal during thermal relaxation can be used. For instance, the specific heat capacity of copper at 25°C is known to be 385 J/kg/K. For more detailed description about the experiment, the interested reader is referred to [77].

Figure 2.6 shows the measured and simulated temperatures at the core and the

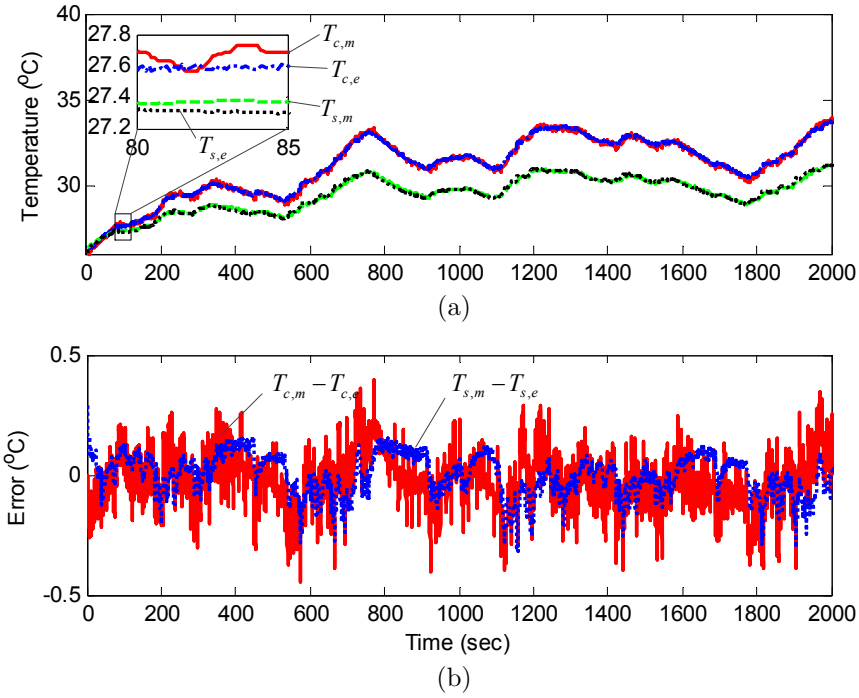

Figure 2.6: Comparison between measurement and simulation: (a) core and surface temperatures, (b) errors

surface of the battery. The error between the measurements and simulated temperature is less than the sensor accuracy of 0.5°C. Using Eq. (2.20), the temperature distribution inside the battery can be predicted as presented in Fig. 2.7(a).

Figure 2.7(b) shows the volume-averaged temperature and its gradient of the battery respectively. There is no significant difference between the volume-averaged temperature and the linear average of the core and the surface temperatures, i.e. $(T_{\mathrm{s}}+T_{\mathrm{c}})/2$. Existing approaches in [64,65,78] have the capability of predicting the core temperature and have shown the efficacy of their proposed methods on the prediction of temperature inside the battery under consideration in this work. However, the phenomena may differ in the case of a battery with larger radius [79]. The volume-averaged temperature gradient is different from the linear temperature gradient, i.e. $(T_{\mathrm{s}} - T_{\mathrm{c}})/R$. In particular, the volume-averaged temperature gradient is 1.36 times greater than linear temperature gradient under the UAC test. Since non-uniform temperature distribution can lead to accelerated capacity losses of inner core [79], the volume-averaged temperature gradient is an important metric to describe severity of temperature inhomogeneity inside the battery.

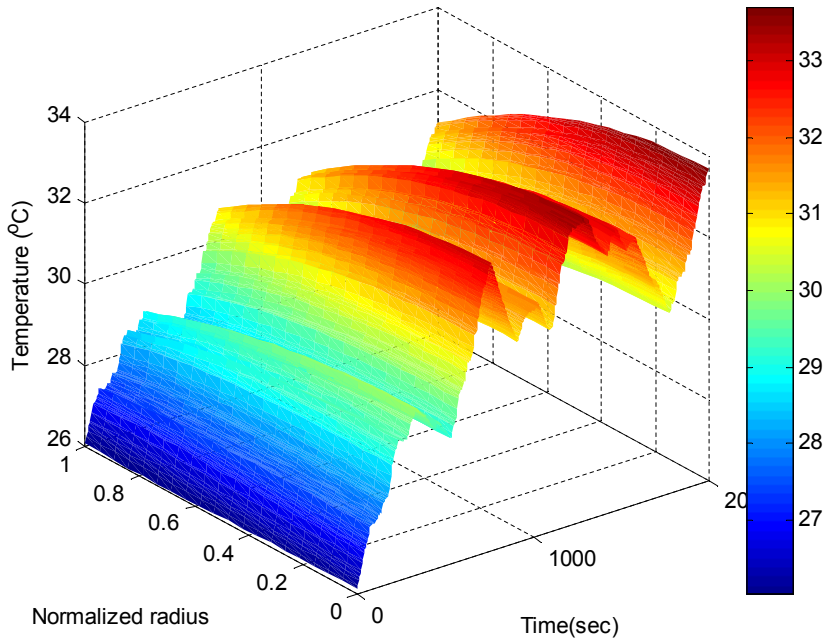

(a)

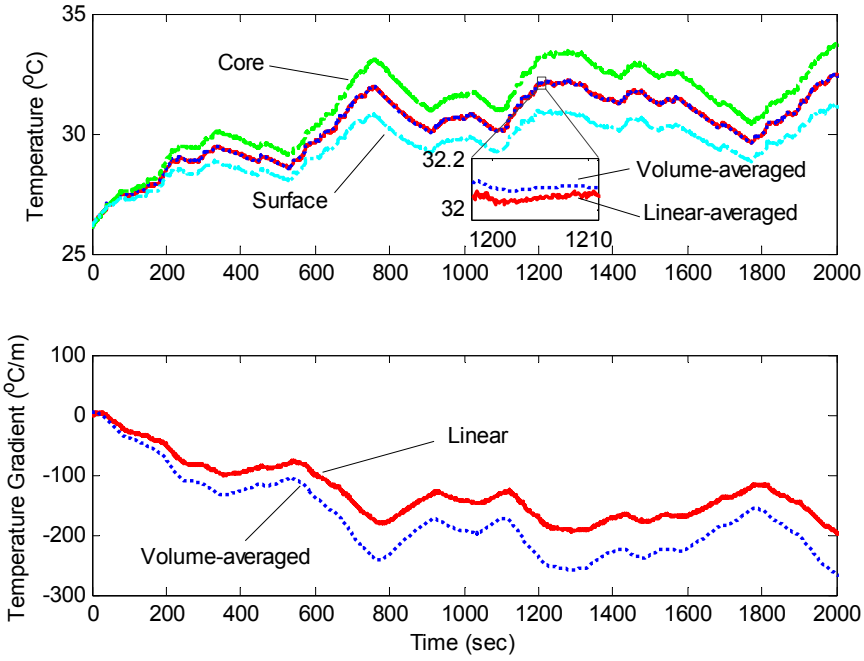

(b)

Figure 2.7: (a) Expected temperature distribution along the normalized radius (r/R) using polynomial approximation, (b) battery temperature (top) and temperature gradient (bottom)

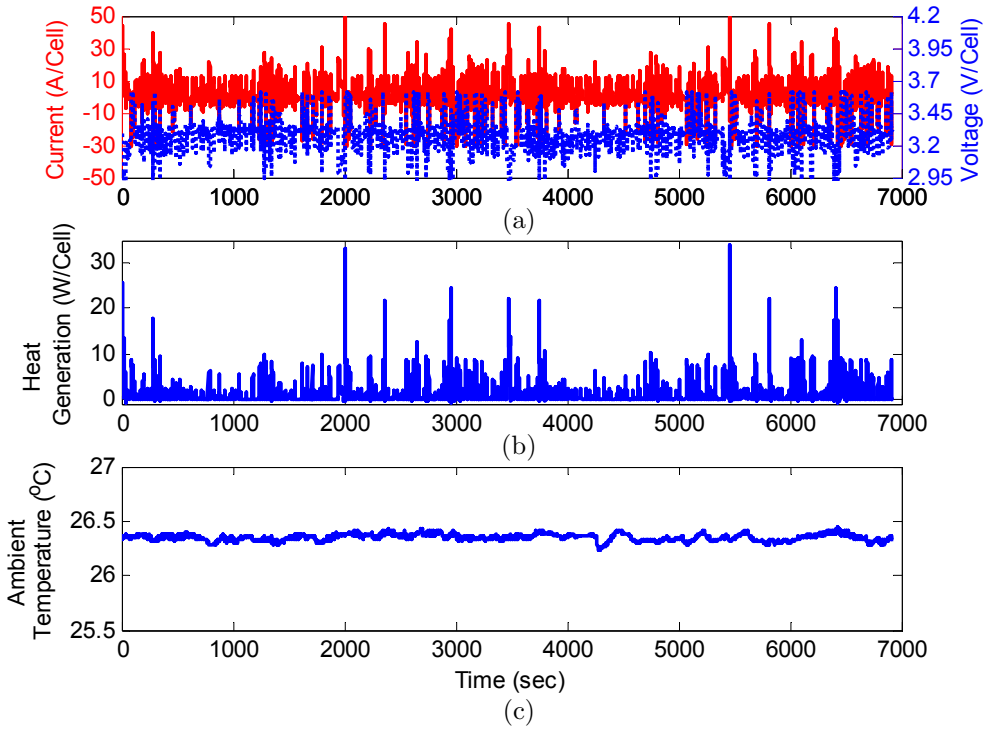

Figure 2.8: Data set during Escort-convoy Cycle used for model validation: (a) current and voltage, (b) heat generation rate, (c) ambient temperature

2.3.2 Model Validation

To validate the performance of the proposed model with the identified parameters, the battery was tested under a different HEV drive cycle, the Escort Convoy Cycle (ECC) [66]. The current and voltage profiles for this cycle are illustrated in Fig. 2.8. Figure 2.9 shows that there are slight differences between the measured and simulated temperatures; in particular, the root-mean-square errors (RMSEs) of the core and the surface temperatures are 0.4°C and 0.3°C, respectively. These differences may be explained with the assumption of radially uniform heat generation and high conductivity in the axial direction. Additionally, the entropy change of the LFP battery is not properly considered in the heat generation formulation (2.27b), which might introduce error in the calculation of heat generation rate. Nevertheless, since the comparison of temperatures shows good agreement and reasonably small RMSEs, it can be concluded that the proposed model with identified thermal properties is sufficiently accurate for thermal management during HEV drive cycles.

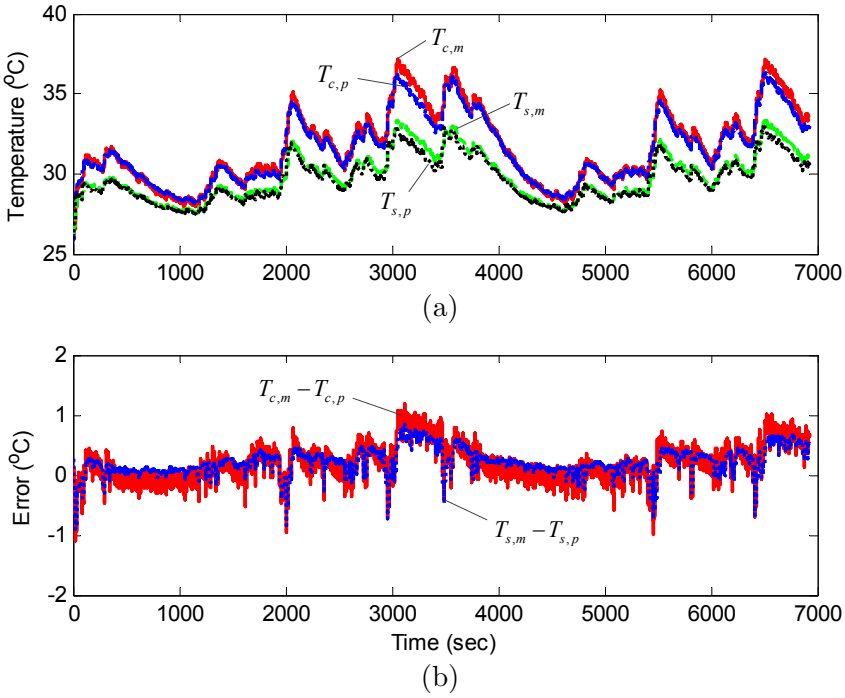

Figure 2.9: Comparison between measurement and simulation: (a) core and surface temperatures, (b) errors

2.4 Conclusion

In this chapter, a radially distributed 1-D thermal modeling approach for a cylindrical battery is proposed. Polynomial approximation is applied to obtain a reduced-order model. Frequency domain analysis shows that the proposed model provides sufficiently accurate prediction of the core and the surface temperatures with a reasonable assumption that the temperature of cooling media does not change rapidly.

The proposed model is used to identify thermal properties and convective coefficient for a 2.3 Ah 26650 LFP battery using a set of measured data: the current, the voltage, the core and the surface temperatures along with the ambient temperature over the UAC test. The identified parameters are found to be close to the values in literature. The proposed thermal model can accurately predict the core and the surface temperatures along with the volume-averaged temperature and the volume-averaged temperature gradient of a cylindrical Li-ion battery. Particularly, the volume-averaged temperature gradient captures the imbalance of temperature distribution which is useful for controlling battery cooling system.

CHAPTER III

The Estimation of Temperature Distribution in Cylindrical Battery Cells under Unknown Cooling Conditions

3.1 Introduction

The performance of Li-ion batteries is highly affected by operation temperature. The battery temperature depends on the convection coefficient which in turn is influenced by the flow rate of the cooling system. This flow rate can be actively controlled by variable speed motors and pumps. However, the performance of the cooling system can degrade generally due to various reasons such as dust on fan blades, partial blockage in pipes, motor/pump ageing, and motor/pump failure. Even though such degradation or failure can be detected by a fault detection system via pressure and temperature sensors, the battery management system still needs to identify the convection coefficient in real-time for an accurate estimation of the core temperature.

This chapter presents a model-based approach for estimating the temperature distribution inside cylindrical batteries under unknown convective cooling conditions. The reduced order thermal model developed in Chapter II is used. Two state and parameter estimation methods, namely a Dual Kalman Filter and a joint Extended Kalman Filter, are then applied for the identification of the convection coefficient and the estimation of the temperature distribution within the battery. Experimental results show that the proposed Kalman Filter-based estimation methods can provide an accurate prediction of core temperature under unknown cooling conditions.

This chapter is organized as follows: Section 3.2 presents the reduced order thermal model for a cylindrical battery with convective cooling. The sensitivity of parameters on prediction temperature is numerically analyzed in Section 3.3. In Section 3.4, temperature estimators applying a Dual Kalman filter and a Joint Extended Kalman

Filter by using the proposed model are developed for estimating the core temperature and identifying the convection coefficient. Section 3.5 presents and discusses experimental results and conclusions are drawn in Section 3.6.

3.2 Reduced-Order Thermal Model

Two-state thermal model for a cylindrical battery with convective cooling developed in Chapter II is adopted and reproduced below for convenience:

$$\frac{dx}{dt} = Ax + Bu, \tag{3.1a}$$

$$y = Cx + Du, \tag{3.1b}$$

where $x = [\bar{T}\ \bar{\gamma}]^T$, $u = [\dot{q}\ T_\infty]^T$ and $y = [T_\mathrm{c}\ T_\mathrm{s}]^T$ are states, inputs and outputs respectively. The states are given by:

$$\bar{T} = \frac{2}{R^2}\int_0^R rT dr, \tag{3.2a}$$

$$\bar{\gamma} = \frac{2}{R^2}\int_0^R r\left(\frac{\partial T}{\partial r}\right) dr, \tag{3.2b}$$

where R is the radius of the battery.

System matrices A, B, C, and D are defined as follows:

$$A = \begin{bmatrix} \dfrac{-48\alpha h}{R(24k_t + Rh)} & \dfrac{-15\alpha h}{24k_t + Rh} \\ \dfrac{-320\alpha h}{R^2(24k_t + Rh)} & \dfrac{-120\alpha(4k_t + Rh)}{R^2(24k_t + Rh)} \end{bmatrix}, \tag{3.3a}$$

$$B = \begin{bmatrix} \dfrac{\alpha}{k_t V_\mathrm{b}} & \dfrac{48\alpha h}{R(24k_t + Rh)} \\ 0 & \dfrac{320\alpha h}{R^2(24k_t + Rh)} \end{bmatrix}, \tag{3.3b}$$

$$C = \begin{bmatrix} \dfrac{24k_t - 3Rh}{24k_t + Rh} & -\dfrac{120Rk_t + 15R^2h}{8(24k_t + Rh)} \\ \dfrac{24k_t}{24k_t + Rh} & \dfrac{15Rk_t}{48k_t + 2Rh} \end{bmatrix}, \tag{3.3c}$$

$$D = \begin{bmatrix} 0 & \dfrac{4Rh}{24k_t + Rh} \\ 0 & \dfrac{Rh}{24k_t + Rh} \end{bmatrix}, \tag{3.3d}$$

Table 3.1: Parameters of the battery

Parameter	Symbol	Value	Unit
Density	ρ	2047	kg/m^3
Specific heat capacity	c_p	1109.2	J/kg/K
Thermal conductivity	k_t	0.610	W/m/K
Radius	R	12.93e-3	m
Volume	V_b	3.4219e-5	m^3

where k_t and h represent thermal conductivity of the battery and convection coefficient, respectively. The thermal diffusivity is defined by $\alpha = k_t/\rho c_p$ where ρ is volume-averaged density of the battery. The volume of the battery is denoted by V_b. Parameters of a cylindrical battery under consideration are summarized in Table 3.1.

This state-space representation is used for sensitivity analysis of parameters on prediction temperature in Section 3.3 and the estimation of the core temperature and convection coefficient using Kalman Filters such as a Dual Kalman Filter and a Joint Extended Kalman Filter in Section 3.4

3.3 Parameter Sensitivity Analysis

Parameters of a model may not be *practically* identifiable or estimable since information available in the experimental data is insufficient. Parameter inestimability is attributed to two reasons: (1) the output predicted by the model is not sensitive to parameter variations, (2) the influence of one parameter on the output is not distinguishable from the influence of other parameters.

Parameter estimability must be assessed to measure whether or which parameters among thermal conductivity k_t, specific heat capacity c_p, and convection coefficient h are estimable with given noisy data such as current and voltage. Sensitivity analysis is a good method for this assessment. In particular, two approaches are considered, namely One-Factor-At-A-Time (OFAT) [80] and the Fisher Information Matrix (FIM) based approach [81].

First, to investigate the impact of variations in parameters on the performance of temperature prediction, each parameter is varied from the known value at a time while holding the other parameters fixed. Current and terminal voltage over the Urban Assault Cycle (UAC) are used as inputs to the thermal model. Figure 3.1 shows that parameters such as thermal conductivity k_t and specific heat capacity c_p

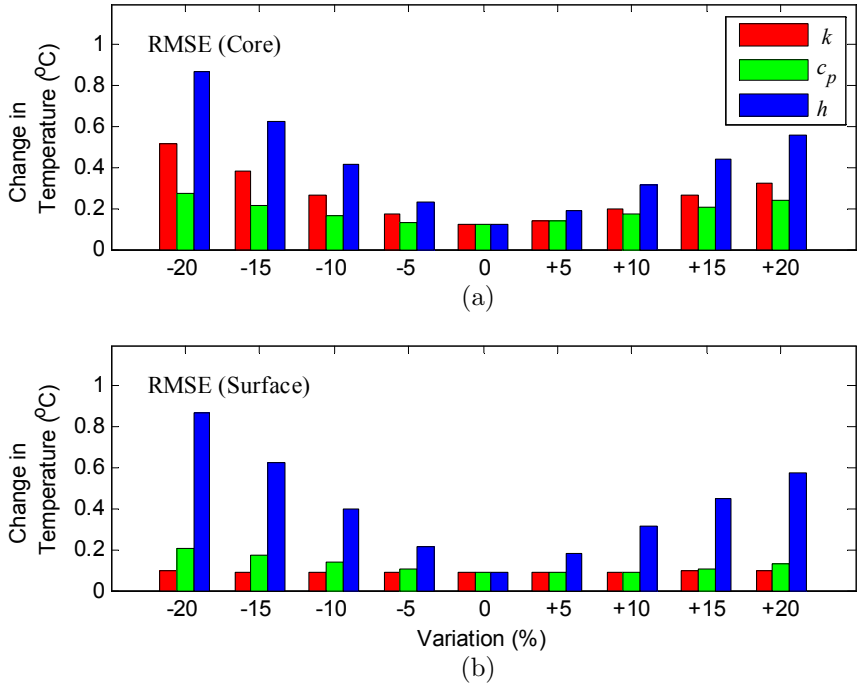

Figure 3.1: The effects of parameter variation to temperature prediction at: (a) core, (b) surface; the convection coefficient has the most significant influence on temperature prediction.

have more influence on the prediction of core temperature than surface temperature. This result corresponds to the fact that the generated heat inside the battery cell is transferred through conduction. On the other hand, the convection coefficient has the most significant influence on the overall prediction of the core and surface temperature. In particular, the prediction of surface temperature is most sensitive to the variation of convection coefficient, which can be explained given the fact that the convection coefficient is directly related to the following convective boundary condition,

$$\frac{\partial T(r,t)}{\partial r}\Big|_{r=R} = -\frac{h}{k_t}(T(R,t) - T_\infty(t)), \tag{3.4}$$

where T_∞ is ambient temperature.

Despite simplicity to check for the impact of parameter variations to model prediction, the OFAT is not able to assess parameter interactions or correlations. To account for these effects, the FIM-based method is additionally used to determine which parameters are estimable using the surface temperature.

Let a parameter vector be

$$p = [k_t \, c_p \, h]^T. \tag{3.5}$$

Sensitivity matrix Ψ for specific time periods $(t_1, t_2, \ldots, t_f)$ is calculated by stacking the partial derivative of output with respect to parameter $\partial y_i / \partial p_j$ ($i = 1, 2$ and $j = 1, 2, 3$) as below

$$\Psi = \begin{bmatrix} \left(\frac{\hat{p}_1}{y(t_1)}\right) \frac{\partial y}{\partial p_1}\Big|_{t_1} & \left(\frac{\hat{p}_2}{y(t_1)}\right) \frac{\partial y}{\partial p_2}\Big|_{t_1} & \left(\frac{\hat{p}_3}{y(t_1)}\right) \frac{\partial y}{\partial p_3}\Big|_{t_1} \\ \left(\frac{\hat{p}_1}{y(t_2)}\right) \frac{\partial y}{\partial p_1}\Big|_{t_2} & \left(\frac{\hat{p}_2}{y(t_2)}\right) \frac{\partial y}{\partial p_2}\Big|_{t_2} & \left(\frac{\hat{p}_3}{y(t_2)}\right) \frac{\partial y}{\partial p_3}\Big|_{t_2} \\ \left(\frac{\hat{p}_1}{y(t_3)}\right) \frac{\partial y}{\partial p_1}\Big|_{t_3} & \left(\frac{\hat{p}_2}{y(t_3)}\right) \frac{\partial y}{\partial p_2}\Big|_{t_3} & \left(\frac{\hat{p}_3}{y(t_3)}\right) \frac{\partial y}{\partial p_3}\Big|_{t_3} \\ & \vdots & \\ \left(\frac{\hat{p}_1}{y(t_f)}\right) \frac{\partial y}{\partial p_1}\Big|_{t_f} & \left(\frac{\hat{p}_2}{y(t_f)}\right) \frac{\partial y}{\partial p_2}\Big|_{t_f} & \left(\frac{\hat{p}_3}{y(t_f)}\right) \frac{\partial y}{\partial p_3}\Big|_{t_f} \end{bmatrix}, \tag{3.6}$$

while solving the following equations along with Eq. (3.1):

$$\frac{d}{dt}\left(\frac{\partial x}{\partial p}\right) = \frac{\partial A}{\partial p} x + \frac{\partial B}{\partial p} u + A \frac{\partial x}{\partial p}, \tag{3.7a}$$

$$\frac{\partial y}{\partial p} = \frac{\partial C}{\partial p} x + \frac{\partial D}{\partial p} u + C \frac{\partial x}{\partial p}. \tag{3.7b}$$

As suggested in [72], $\partial y_i / \partial p_j$ at time t_i is normalized using the nominal values of parameters $\hat{p}$ and output values y at t_i. Then, the FIM is computed by

$$\text{FIM} = \Psi^T \Psi \tag{3.8}$$

The FIM and correlation of Ψ provide very useful information about the estimation problem. The rank of the FIM presents the number of estimable parameters. A highly ill-conditioned FIM indicates that estimation of all parameter is almost infeasible. In particular, the largest element of an eigenvector corresponding to the smallest eigenvalue indicates the least estimable parameter. Moreover, the inverse of FIM means the covariance of parameter estimates.

Using the same input data, eigenvalues Λ and eigenvectors Γ of the FIM and the inverse of the FIM for two cases (case1: T_s only, case2: T_s and T_c) are computed

respectively as follows:

$$\Lambda_{\text{case1}} = \begin{bmatrix} 0.26 & 0 & 0 \\ 0 & 11.02 & 0 \\ 0 & 0 & 848.52 \end{bmatrix}, \tag{3.9a}$$

$$\Lambda_{\text{case2}} = \begin{bmatrix} 59.23 & 0 & 0 \\ 0 & 78.00 & 0 \\ 0 & 0 & 1550.28 \end{bmatrix}, \tag{3.9b}$$

$$\Gamma_{\text{case1}} = \begin{bmatrix} 0.9559 & -0.2934 & -0.0136 \\ 0.2852 & 0.9381 & -0.1963 \\ 0.0704 & 0.1838 & 0.9804 \end{bmatrix}, \tag{3.9c}$$

$$\Gamma_{\text{case2}} = \begin{bmatrix} -0.9005 & 0.4059 & 0.1560 \\ 0.3849 & 0.9109 & -0.1487 \\ 0.2025 & 0.0739 & 0.9765 \end{bmatrix}. \tag{3.9d}$$

$$\text{FIM}^{-1}_{\text{case1}} = \begin{bmatrix} 3.465 & 1.006 & 0.25 \\ 1.006 & 0.388 & 0.091 \\ 0.25 & 0.091 & 0.023 \end{bmatrix}, \tag{3.9e}$$

$$\text{FIM}^{-1}_{\text{case2}} = \begin{bmatrix} 0.016 & -0.001 & -0.003 \\ -0.001 & 0.013 & 0.002 \\ -0.003 & 0.002 & 0.001 \end{bmatrix}. \tag{3.9f}$$

It is apparent that k_t is the most difficult parameter to be estimated, followed by c_p and h, respectively. The parameter covariance indicates that the estimation of k_t from the surface temperature measurement only is almost infeasible whereas h is estimable under the same condition. Since the core and surface temperatures are important information to characterize heat conduction inside the battery, the estimability of k_t and c_p is dramatically improved with two measurement data as indicated by parameter covariance. From the FIM-based sensitivity results, it can be concluded that convection coefficient is estimable from the surface temperature measurement under realistic operating conditions.

According to Maleki *et al.*, Forgez *et al.*, and Onda *et al.*, the specific heat capacity and thermal conductivity are weakly dependent on temperature [65,82,83]; therefore, the assumption of constant parameters can be justified. On the other hand, the convection coefficient is highly dependent on fan speed or fluid velocity as expressed by empirical correlations provided by Zukauskas [84]. Consequently, the accurate identification of convection coefficient is important for better prediction of temperature

inside the battery. This importance as well as the sensitivity analysis justify the on-line identification of the convection coefficient for better estimation of temperature as detailed in Section 3.4.

3.4 Estimation of Temperature and Convection Coefficient

As discussed in Section 3.3, the estimation of temperature inside the battery cell requires accurate knowledge of the convection coefficient which depends on cooling condition. To identify the convection coefficient on-line, two estimation methods are applied for better estimation of temperature distribution inside the battery cell: (1) a Dual Kalman filter (DKF) [85] and (2) a Joint Extended Kalman Filter (JEKF). The other thermal parameters such as thermal conductivity and specific heat capacity are constant since these parameters have less influence on temperature and do not change significantly over time. In the following sections, the implementation of these algorithms and their estimation performance are presented.

3.4.1 A Dual Kalman Filter : a combination of Kalman and Extended Kalman Filters

Assuming the input $u(t)$ is constant over each sampling interval Δt, a parameter varying (PV) discrete-time model at time step k can be obtained by using the Euler Method as

$$x_{k+1} = \bar{A}(\theta_k)x_k + \bar{B}(\theta_k)u_k + w_k, \tag{3.10a}$$

$$y_k = C(\theta_k)x_k + D(\theta_k)u_k + v_k, \tag{3.10b}$$

$$\theta_{k+1} = \theta_k + r_k, \tag{3.10c}$$

where $x_k = [\bar{T}_k \ \bar{\gamma}_k]^T$, $y = T_{\mathrm{s},k}$, $\theta_k = h_k$, and $u_k = [\dot{q}_k \ T_{\infty,k}]^T$. System matrices $\bar{A} \approx I + A\Delta t$ and $\bar{B} = B\Delta t$ are obtained from matrices (3.3) where I is the identity matrix. Noise signals w_k, v_k and r_k, are independent, zero-mean, Gaussian processes of covariance matrices Σ_w, Σ_v, and Σ_r, respectively.

The schematic of a DKF is illustrated in Fig. 3.2. At time step k, the KF estimates the state using the current model estimate $\hat{\theta}^+_{k-1}$, whereas the EKF estimates the parameter using the current state estimate $\hat{x}^+_{k-1}$. The design of the DKF estimator is given as the following update processes.

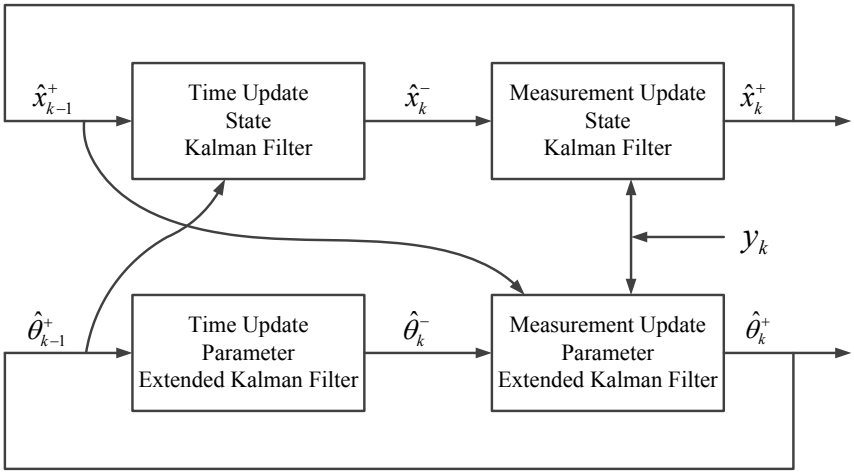

Figure 3.2: Schematic of a Dual Kalman Filter

Time update for the parameter filter:

$$\hat{\theta}_k^- = \hat{\theta}_{k-1}^+, \tag{3.11a}$$

$$P_{\theta,k}^- = P_{\theta,k-1}^+ + \Sigma_r. \tag{3.11b}$$

Time update for the state filter:

$$\hat{x}_k^- = \bar{A}_{k-1}\hat{x}_{k-1}^+ + \bar{B}_{k-1}u_{k-1} \tag{3.12a}$$

$$P_{x,k}^- = \bar{A}_{k-1}P_{x,k-1}^+\bar{A}_{k-1}^T + \Sigma_w. \tag{3.12b}$$

Measurement update for the state filter:

$$K_k = P_{x,k}^- C_k^{xT}\left[C_k^x P_{x,k}^- C_k^{xT} + \Sigma_v\right]^{-1}, \tag{3.13a}$$

$$\hat{x}_k^+ = \hat{x}_k^- + K_k\left[y_k - C(\hat{\theta}_k^-)\hat{x}_k^- - D(\hat{\theta}_k^-)u_k\right] \tag{3.13b}$$

$$P_{x,k}^+ = \left[I - K_k C_k^x\right] P_{x,k}^-. \tag{3.13c}$$

Measurement update for the parameter filter:

$$L_k = P_{\theta,k}^- C_k^{\theta T}\left[C_k^\theta P_{\theta,k}^- C_k^{\theta T} + \Sigma_v\right]^{-1}, \tag{3.14a}$$

$$\hat{\theta}_k^+ = \hat{\theta}_k^- + L_k\left[y_k - C(\hat{\theta}_k^-)\hat{x}_k^- - D(\hat{\theta}_k^-)u_k\right] \tag{3.14b}$$

$$P_{\theta,k}^+ = \left[I - L_k C_k^\theta\right] P_{\theta,k}^-, \tag{3.14c}$$

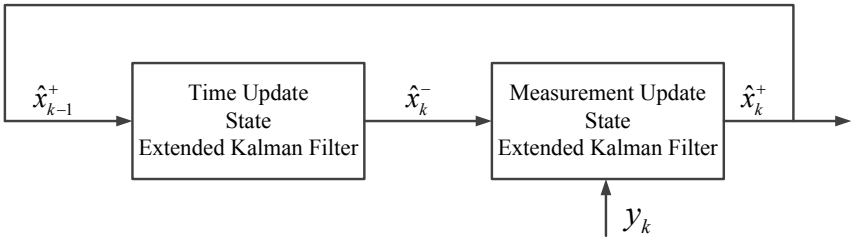

Figure 3.3: Schematic of a Joint Extended Kalman Filter

where superscripts $-$ and $+$ denote the *a priori* and *a posteriori* values respectively. The matrices $\bar{A}_{k-1}$, C_k^x and C_k^θ are calculated according to

$$\bar{A}_{k-1} = \bar{A}(\theta_k)|_{\theta_k=\hat{\theta}_k^-}, \tag{3.15a}$$

$$C_k^x = \frac{\partial y_k}{\partial x_k}\Big|_{x_k=\hat{x}_k^-,\theta_k=\hat{\theta}_k^-}, \tag{3.15b}$$

$$C_k^\theta = \frac{dy_k}{d\theta_k}\Big|_{x_k=\hat{x}_k^-,\theta_k=\hat{\theta}_k^-}. \tag{3.15c}$$

The identified states $\hat{x}$ and parameter $\hat{\theta}$, computed from the above DKF algorithm, are used to estimate the core temperature in the battery from Eqs. (3.10). It is noted that since the thermal system is linear, the DKF becomes a Kalman filter (KF) when the parameter of convection coefficient is known or given.

3.4.2 A Joint Extended Kalman Filter

An alternative approach to estimate states and parameter is applying a Joint Extended Kalman Filter. States x_k and parameter θ_k are concatenated into an augmented state vector $x_{a,k} = [x_k \ \ \theta_k]^T$. As illustrated in Fig. 3.3, the augmented states can be simultaneously estimated through an Extended Kalman Filter, the result of the application of a Kalman Filter to a linearized nonlinear system.

The augmented system can be expressed as follows:

$$x_{a,k+1} = \bar{A}_a x_{a,k} + \bar{B}_a u_k + w_k, \tag{3.16a}$$

$$y_k = C_a x_{a,k} + D_a u_k + v_k, \tag{3.16b}$$

where the augmented system matrices are defined by

$$\bar{A}_a = \begin{bmatrix} \bar{A}(\theta_k) & 0 \\ 0 & 1 \end{bmatrix}, \tag{3.17a}$$

$$\bar{B}_a = \begin{bmatrix} \bar{B}(\theta_k) \\ 0 \end{bmatrix}, \tag{3.17b}$$

$$C_a = \begin{bmatrix} C(\theta_k) & 0 \end{bmatrix}, \tag{3.17c}$$

$$D_a = D(\theta_k). \tag{3.17d}$$

The augmented system is nonlinear even though Eqs. (3.16) are expressed in a form of linear state-space representation, which needs ones to apply an Extended Kalman Filter in the estimator design.

The design of the Joint EKF estimator is given as the following update processes. Time update for the state filter:

$$\hat{x}^-_{a,k} = \bar{A}_{a,k-1}\hat{x}^+_{a,k-1} + \bar{B}_{a,k-1}u_{k-1} \tag{3.18a}$$

$$P^-_k = \bar{A}_{a,k-1}P^+_{k-1}\bar{A}^T_{a,k-1} + \Sigma_w. \tag{3.18b}$$

Measurement update for the state filter:

$$K_k = P^-_k {C^x_{a,k}}^T \left[C^x_{a,k}P^-_k {C^x_{a,k}}^T + \Sigma_v\right]^{-1}, \tag{3.19a}$$

$$\hat{x}^+_{a,k} = \hat{x}^-_{a,k} + K_k\left[y_k - C_a\hat{x}^-_{a,k} - D_a u_k\right] \tag{3.19b}$$

$$P^+_k = \left[I - K_k C^x_{a,k}\right]P^-_k. \tag{3.19c}$$

The matrices $\bar{A}_{a,k-1}$ and $C^x_{a,k}$ are calculated according to

$$\bar{A}_{a,k-1} = \begin{bmatrix} \bar{A}(\hat{\theta}^+_{k-1}) & \dfrac{\partial \bar{A}(\hat{\theta}^+_{k-1})}{\partial \theta_k}\hat{x}^+_{k-1} + \dfrac{\partial \bar{B}(\hat{\theta}^+_{k-1})}{\partial \theta_k}u_{k-1} \\ 0 & 1 \end{bmatrix}, \tag{3.20a}$$

$$C^x_{a,k} = \begin{bmatrix} C(\hat{\theta}^+_{k-1}) & \dfrac{\partial C(\hat{\theta}^+_{k-1})}{\partial \theta_k}\hat{x}^+_{k-1} + \dfrac{\partial D(\hat{\theta}^+_{k-1})}{\partial \theta_k}u_{k-1} \end{bmatrix}. \tag{3.20b}$$

Finally, the identified augmented states $\hat{x}_a$, obtained from the above JEKF algorithm, are used to estimate the core temperature in the battery from Eqs. (3.16). In this framework, the statistics of noise signals are defined as before. However, the noise signal w_k and its covariance matrix Σ_w need to be redefined to account for disturbances affecting the parameter dynamics.

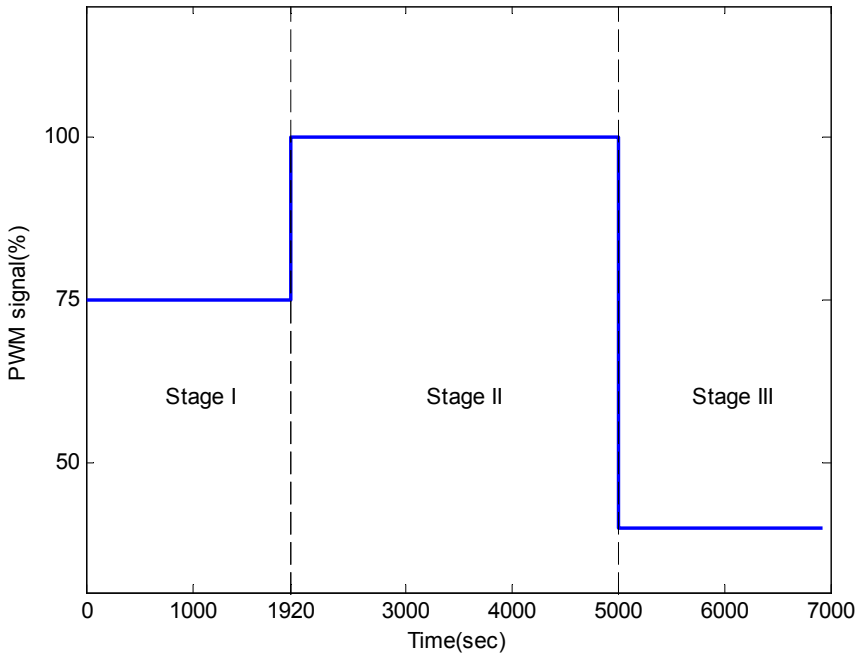

Figure 3.4: Fan schedule for forced-air convective cooling

3.5 Experimental Results

In this section, the performances of the proposed temperature estimators using the DKF and the JEKF are compared with that of the baseline KF estimator without parameter identification. Following an experimental set-up shown in Chapter II, we draw a current and measure voltage and temperature at the core and surface of the battery while controlling ambient temperature in the thermal chamber. The surface temperature is used for the estimators and the core temperature is measured to verify the estimation accuracy. The experiment is performed using the Escort-Convoy Cycle (ECC) to verify the state and parameter estimation. Three different forced convective cooling conditions (stage I, stage II, and stage III) are demonstrated by using different PWM signals driving the fan as shown in Fig. 3.4. To investigate the influence of change in the initial parameter on the temperature estimation, the parameter is provided to each estimator as following:

- In stage I, the off-line predetermined convection coefficient is provided to the KF and is used for the DKF and JEKF as initial values: $\tilde{\theta} = \theta^*$ and $\hat{\theta}(0) = \breve{\theta}(0) = \theta^*$
- In stage II, the off-line predetermined convection coefficient is provided to the

Table 3.2: Tuning parameters for the DKF and JEKF

Parameter	DKF	JEKF
Σ_w	diag($\beta_1{}^2, \beta_1{}^2$)	diag($\beta_1{}^2, \beta_1{}^2, \beta_2{}^2$)
Σ_v	σ^2	σ^2
Σ_r	$\beta_2{}^2$	$\times$
$P(0)$	diag(1,1)	diag(1,1,0.05)
$S(0)$	0.05	$\times$
β_1	0.0005	0.0005
β_2	0.007	0.006

KF only: $\tilde{\theta} = \theta^*$

- In stage III, two times larger convection coefficient compared to the known value is provided to the KF: $\tilde{\theta} = 2\theta^*$

where the parameter $\tilde{\theta}$ denotes a fixed value for the KF. The parameters $\hat{\theta}$ and $\breve{\theta}$ represent identified values for the DKF and JEKF, respectively whereas θ^* presents the predetermined parameter value. Other thermal properties such as the thermal conductivity and the specific heat capacity are assumed constant with values provided in Table 3.1.

It is assumed that the initial temperature distribution inside the battery is uniform at 30°C and convection coefficient is 56.2W/m^2/K, i.e. $\hat{x}(0) = [30\ 0]^T$ and $\hat{\theta}(0) = 56.2$, respectively. The covariance matrix for the state $\Sigma_w = \beta_1{}^2 I$ describes the process noise where $\beta_1 > 0$ is a parameter for tuning based on the model inaccuracy. The noise covariance $\Sigma_v = \sigma^2$ is determined from the standard deviation of temperature signal $\sigma = 0.05$°C. The covariance matrix for the parameter $\Sigma_r = \beta_2{}^2$ influences the performance of noise filtering and the rate of parameter convergence. Ultimately, the initial condition of the error covariance matrix and the tuning parameter for the DKF and JEKF are chosen through repeated simulations as provided in Table 3.2. It is noted that the initial conditions and tuning parameters for the DKF and JEKF are the same as those of the KF.

The results for the parameter and state estimation are shown in Fig. 3.5 and Fig. 3.6–3.8, respectively. The performances of temperature estimation in terms of the root-mean-square-error (RMSE) are summarized in Table 3.3. Figure 3.6 shows that all closed loop estimators can accurately predict temperature inside the battery as evidenced by small RMSEs for core temperature estimation, i.e., 0.18°C. As seen from

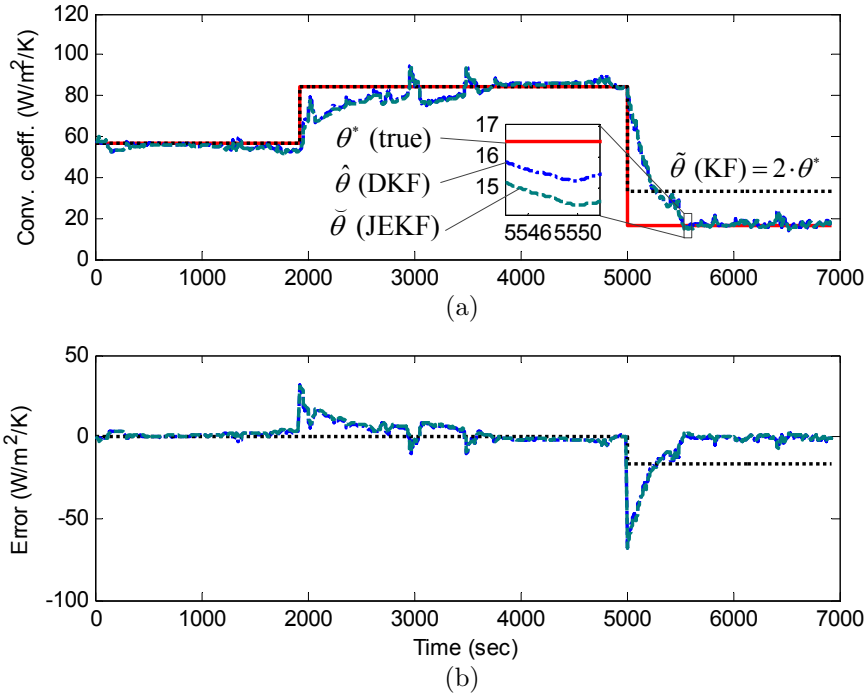

Figure 3.5: Comparison of parameter estimation performance among KF, DKF and JEKF estimators: (a) convection coefficient, (b) errors

Fig. 3.5, on-line (real-time) identified parameters are close to the off-line determined value without large deviations. The deviation is small due to two factors: (1) a correct initial guess for parameter and (2) a relatively small initial parameter covariance. Consequently, performances of the DKF and JEKF estimators are comparable to that of KF estimator. As discussed in Section 3.3, thermal properties can vary with respect to operating temperature. Therefore, it is expected that better performance could be achieved by using temperature-dependent parameters for thermal conductivity and specific heat capacity.

Table 3.3: Comparison of temperature estimation among KF, DKF and JEKF: RMSEs of the core and surface temperatures

Method	KF		DKF		JEKF	
Location	Core	Surface	Core	Surface	Core	Surf.
Stage I	0.18	0.07	0.18	0.07	0.18	0.07
Stage II	0.24	0.08	0.25	0.08	0.25	0.08
Stage III	1.58	0.15	0.45	0.11	0.40	0.11

Figure 3.7 illustrates the performance of temperature estimation by the closed-loop estimators in stage II when there are sudden changes in the cooling condition. The KF can accurately estimate the core temperature with information about the change in parameter values. Since the DKF and JEKF are capable of compensating for inaccuracy in the parameter of the system, the DKF and JEKF provide reasonably accurate estimates for the core temperature in comparison to the core temperature predicted by the KF estimator. The RMSEs for core temperature estimation by the DKF and JEKF are 0.25°C which is very close to the RMSE by the KF, indicating that the errors during initial time periods before parameters converge to the true value are insignificant (Fig. 3.5).

As seen from Fig. 3.8, the KF estimator overestimates the core temperature when the incorrect parameter value is used for the convection coefficient. In other words, the reliable estimation of core temperature with the KF is only possible when accurate parameter values are available. Thus, it can be concluded that the DKF and JEKF estimators outperform the KF estimator due to the capability of parameter identification. The RMSEs for core temperature estimation in stage III can be substantially reduced from 1.58°C to 0.45°C and 0.40°C by the DKF and JEKF respectively.

It is worth noting that the DKF and JEKF can be augmented with other existing battery management strategies to improve the system robustness without cost increase. For instance, to detect partial blockage in a cooling system, typically, a mass flow or pressure sensor is required. The DKF and JEKF could augment the existing techniques to provide redundancy during sensor fault. The proposed algorithm enables the identification of the convection coefficient by using sensors which are already instrumented at the battery. The identified parameter can be also used for monitoring the malfunction or degradation of the cooling system. Under the assumption that the relationship between the convection coefficient and fan speed or PWM signal is known, the malfunction of the cooling system can be detected by comparing the identified parameter with the known value. When the difference between the identified and predetermined values $|\hat{\theta} - \theta^*|$ is bounded and small, it can be considered that there is no fault in the cooling system. On the other hand, $|\hat{\theta} - \theta^*| \gg \epsilon$ where ϵ is a pretuned threshold, could be a sign of cooling fault. In particular, $|(\hat{\theta} - \theta^*)/\theta^*|$ could be interpreted as the severity of degradation of the cooling system.

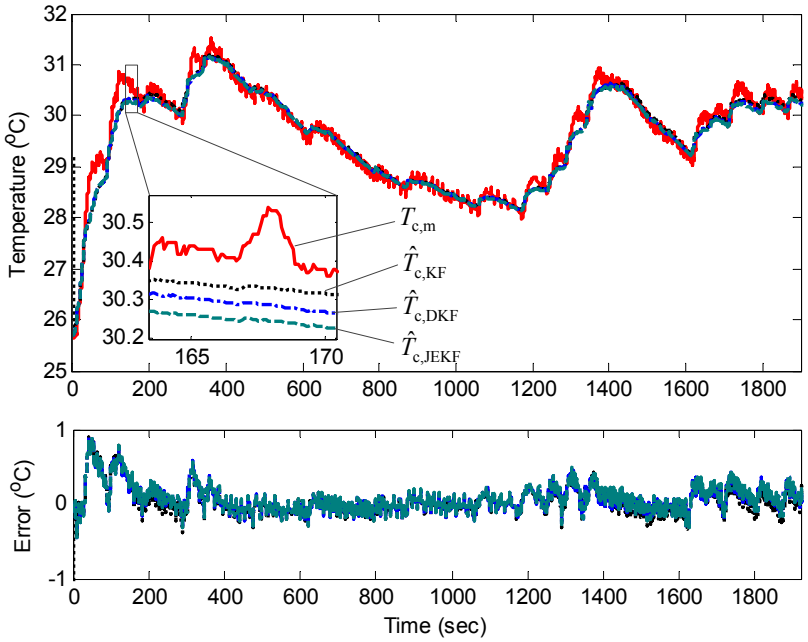

(a)

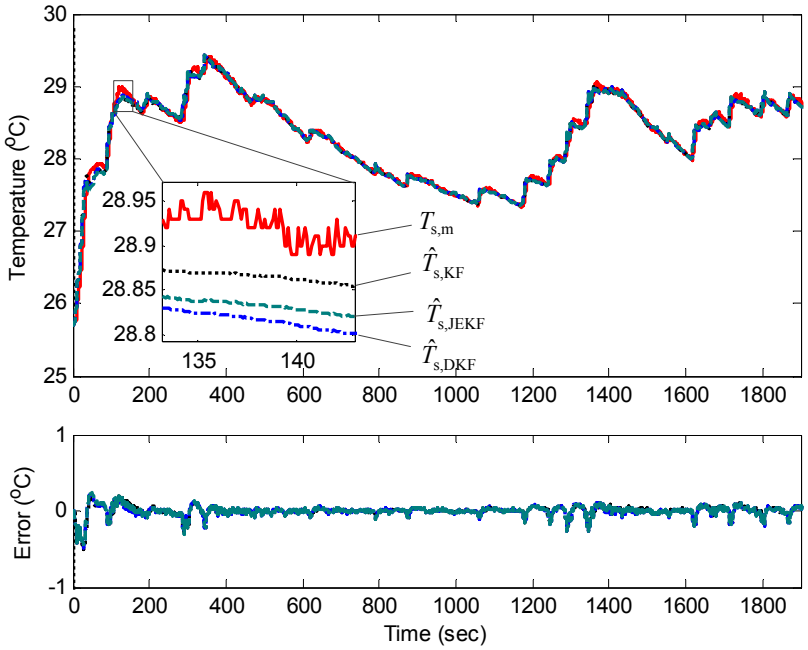

(b)

Figure 3.6: Comparison of state estimation performance among KF, DKF and JEKF estimators during stage I: (a) core temperature, (b) surface temperature

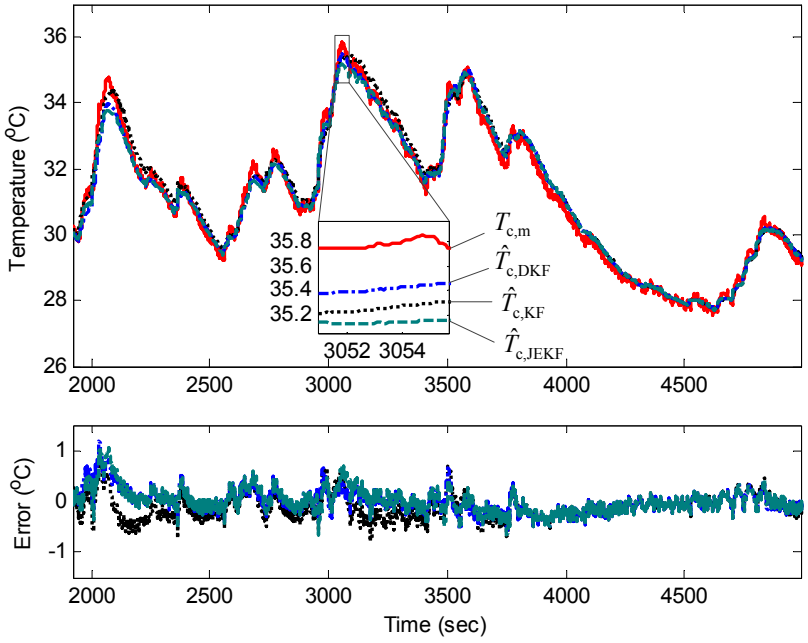

(a)

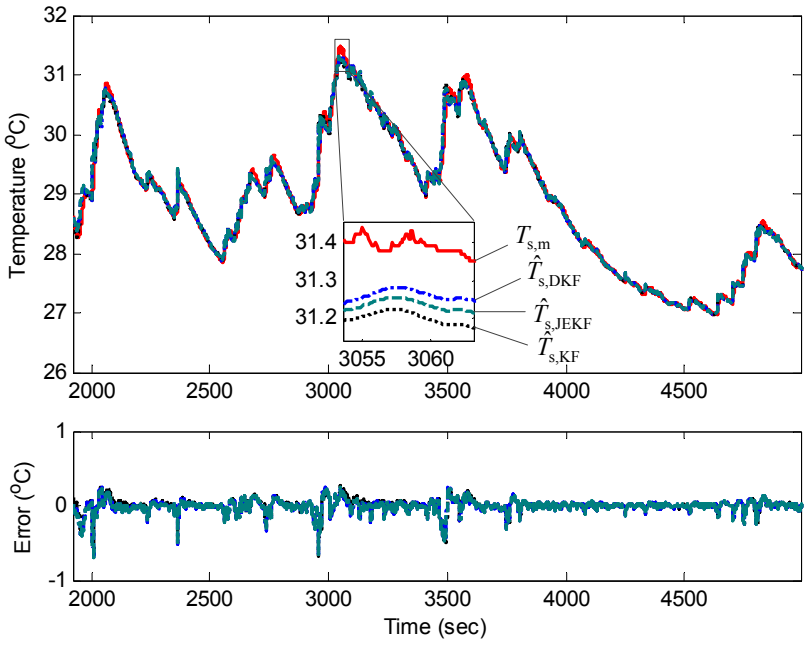

(b)

Figure 3.7: Comparison of state estimation performance among KF, DKF and JEKF estimators during stage II: (a) core temperature, (b) surface temperature

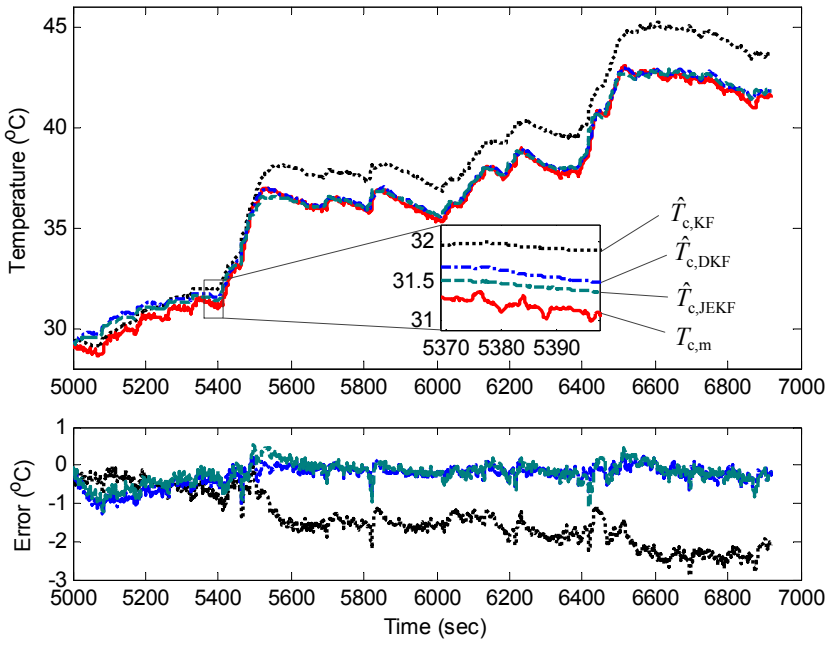

(a)

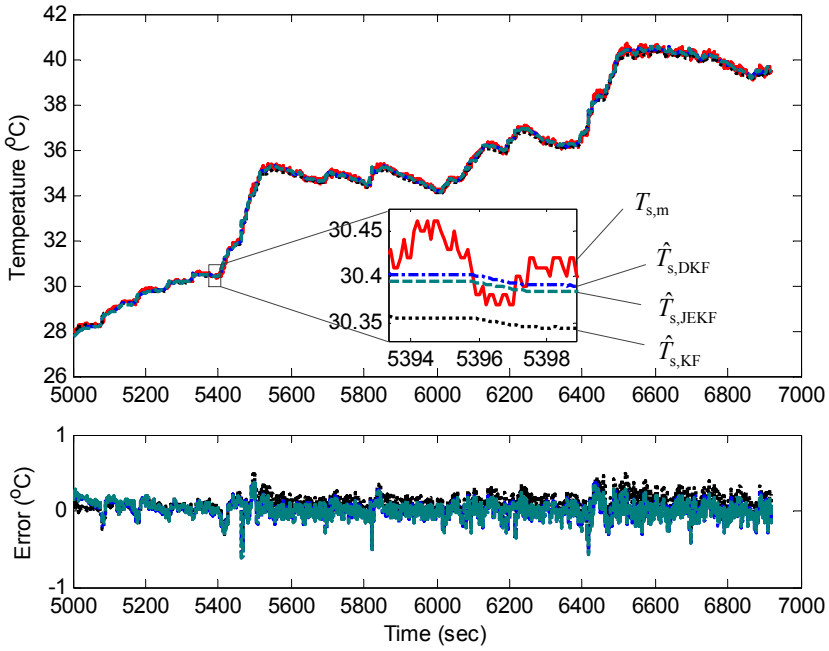

(b)

Figure 3.8: Comparison of state estimation performance among KF, DKF and JEKF estimators during stage III: (a) core temperature, (b) surface temperature

3.6 Conclusion

In this chapter, a method to estimate the temperature distribution in cylindrical batteries under unknown cooling condition is proposed. First, a reduced-order thermal model using a polynomial approximation presented in Chapter II is used to estimate a radial temperature profile. The numerical analysis on parameter sensitivity supports the use of constant parameters for thermal conductivity and heat capacity and the importance of identifying the convection coefficient on-line. Then, a Dual Kalman Filter and a Joint Extended Kalman Filter are applied to estimate the temperature inside the battery and convection coefficient by the cooling fan. The proposed method requires no knowledge of the convective cooling conditions. The results show that the proposed DKF and JEKF estimators can provide reasonably accurate estimates of core temperature and convection coefficient by using current, voltage, battery surface and ambient temperatures. In addition, faulty operation of the cooling system could be detected by monitoring the difference between the identified and off-line predetermined values.

CHAPTER IV

Power Capability Estimation of Lithium-ion Batteries Based on Time Scale Separation

4.1 Introduction

Enforcement of constraints on the maximum deliverable power is essential to protect Li-ion batteries from over-charge/discharge and overheating. This chapter develops an algorithm to address the often overlooked temperature constraint in determining power capability of battery systems. Knowledge of power capability provides dynamic constraints on currents and affords an additional control authority on the temperature of batteries. Power capability is estimated by using a lumped electro-thermal model for a cylindrical cell that has been validated over a wide range of operating conditions. Based on the time scale separation, a real-time implementable method is proposed to determine power capability of a Li-ion battery accounting for thermal and electrical constraints. Current limits and hence power capability are determined by a model-inversion technique, termed Algebraic Propagation (AP). Simulations are performed using realistic depleting currents to demonstrate the effectiveness of the proposed method.

This chapter is organized as follows. Section 4.2 presents a thermal model[1] incorporating information on entropy change in addition to Joule heating and convection phenomena. Then, a simple equivalent-circuit electrical model is presented in Section 4.3 for the electrical dynamics of the battery. In Section 4.4, a model-based maximum power estimation method is proposed to determine the maximum current/power capability over a fixed horizon considering both thermal and electrical constraints inde-

[1]In this chapter, a singe-state thermal model is considered based on the investigation of thermal properties. However, Chapter V addresses power capability estimation for a two-state thermal model.

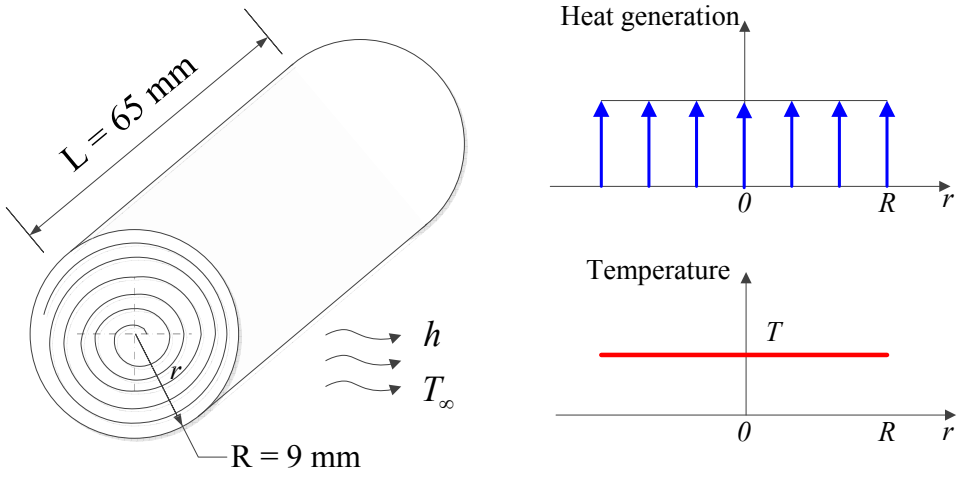

(a) (b)

Figure 4.1: (a) Schematic for an e-Moli ICR18650J cylindrical battery, (b) parabolic temperature profile under uniform heat generation

pendently. Simulation results are discussed in Section 4.5 and conclusions are drawn in Section 4.6.

4.2 Battery Thermal Model

A cylindrical Li-ion battery, e-Moli ICR18650J 2.3 Ah, is considered in this study. This battery is fabricated by rolling a stack of layered thin sheets comprised of a Lithium Cobalt Oxide ($LiCoO_2$) cathode, a separator, and a graphitic anode in a manner similar to the schematic in Fig. 4.1(a). Uniform heat generation along the radial direction as illustrated in 4.1(b) is assumed, which is a standard assumption [68, 86]. Lumped parameters are used so that material properties such as thermal conductivity, density and specific heat capacity are assumed to be constant in a homogeneous and isotropic body. Since the thermal conductivity is one or two orders of magnitude higher in the axial direction than in the radial direction, the temperature distribution in the axial direction will be more uniform [69, 87]. The Biot number[2] (Bi) of the battery with natural convection is calculated to be small ($Bi \ll 0.1$), suggesting that the heat transfer at the surface is much smaller than the internal heat transfer by conduction. Hence, no significant temperature gradient inside the

[2]The Biot number is a ratio of heat convected via surroundings to heat conducted in a material: $Bi = hl/k_t$ where l and k_t are thickness and thermal conductivity respectively.

battery is expected.

Under the above assumptions, the energy balance equation in the battery can be described by one bulk temperature T [83]:

$$Mc_p\frac{dT}{dt} = \dot{q}_{\text{gen}} + \dot{q}_{\text{rev}} + \dot{q}_{\text{rej}}, \tag{4.1a}$$

$$\dot{q}_{\text{gen}} = I_{\text{b}}^2 R_{\text{e}}, \tag{4.1b}$$

$$\dot{q}_{\text{rev}} = -I_{\text{b}} T\frac{\Delta S}{nF}, \tag{4.1c}$$

$$\dot{q}_{\text{rej}} = A_{\text{b}} h(T_\infty - T), \tag{4.1d}$$

where M and A_{b} are the mass and area of the Li-ion battery respectively; $\dot{q}_{\text{gen}}$, $\dot{q}_{\text{ref}}$, and $\dot{q}_{\text{rej}}$ represent joule heating, entropic heat generation, and heat transfer through convection, respectively. The variable n is the charge number pertaining to the reaction (n=1 for a Li-ion battery) and F is the Faraday constant, 96485.3365 C/mol. The internal resistance R_{e} lumps ohmic, activation, diffusion polarization resistances. Heat of mixing is not considered since its contribution to the total heat generation is small [54]. In the chosen sign convention, a positive current discharges the battery.

The energy balance equation is described in the state space representation:

$$\dot{x}_T = \alpha x_T + \beta x_T u + \gamma u^2 + \eta \tag{4.2}$$

where the state and input of the system are $x_T = T$ and $u = I_{\text{b}}$, respectively. The parameters are defined by .

$$\alpha = -\frac{A_{\text{b}} h}{Mc_p}, \tag{4.3a}$$

$$\beta = \frac{-1}{Mc_p}\frac{\Delta S}{nF}, \tag{4.3b}$$

$$\gamma = \frac{R_{\text{e}}}{Mc_p}, \tag{4.3c}$$

$$\eta = \frac{A_{\text{b}} h T_\infty}{Mc_p}. \tag{4.3d}$$

This nonlinear thermal dynamic model is used to predict the temporal evolution of temperature and to formulate a current limiting strategy in Section 4.4.

Table 4.1: List of publications where the entropy change of Li-ion batteries are provided

Author (year)	Temperature Profile [°C]	Test Duration [hours]
Hong *et al.* (1998) [89]	27-30-35-39-50	25
Takano *et al.* (2002) [88]	50-10-50	24
Onda *et al.* (2006) [83]	40-10-20-30-40	33
Viswanathan *et al.* (2010) [90]	35-25-15-35	Not specified*
Forgez *et al.* (2010) [65]	26-16-21-36-26	20
Jalkanen *et al.* (2013) [91]	20-0-10-20-30-40-20	12

* voltage was measured after temperature equalization.

4.2.1 Entropy Change Measurement

The contribution of the entropy change ΔS to the total heat generation in a $LiCoO_2/LiC_6$ battery is significant at low current rates [54, 88]. Therefore, it is important to determine the entropy change of the battery for predicting the temperature of a battery accurately. The entropy change can be identified by using the change in the open circuit voltage, V_{oc}, as a function of temperature according to Eq. (4.4)

$$\Delta S = nF\frac{\partial V_{oc}}{\partial T}. \tag{4.4}$$

Two methods can be considered to measure the entropy change of Li-ion batteries:

1. measuring terminal voltages with very low charge and discharge current rates such as C/20, C/40 and C/100 at different temperatures

2. measuring terminal voltage without current while changing temperature at different battery SOCs

Battery charge and discharge operations at very high or low temperature may affect operations at other temperatures. Thus, the second method has been widely used for the entropy change measurement with considerations of repeatability and/or reproducibility. Table 4.1 illustrates temperature profiles and test duration[3] for the second method in literature [65, 83, 88–91].

[3]Initial time periods to fully charge or discharge a battery is not accounted for.

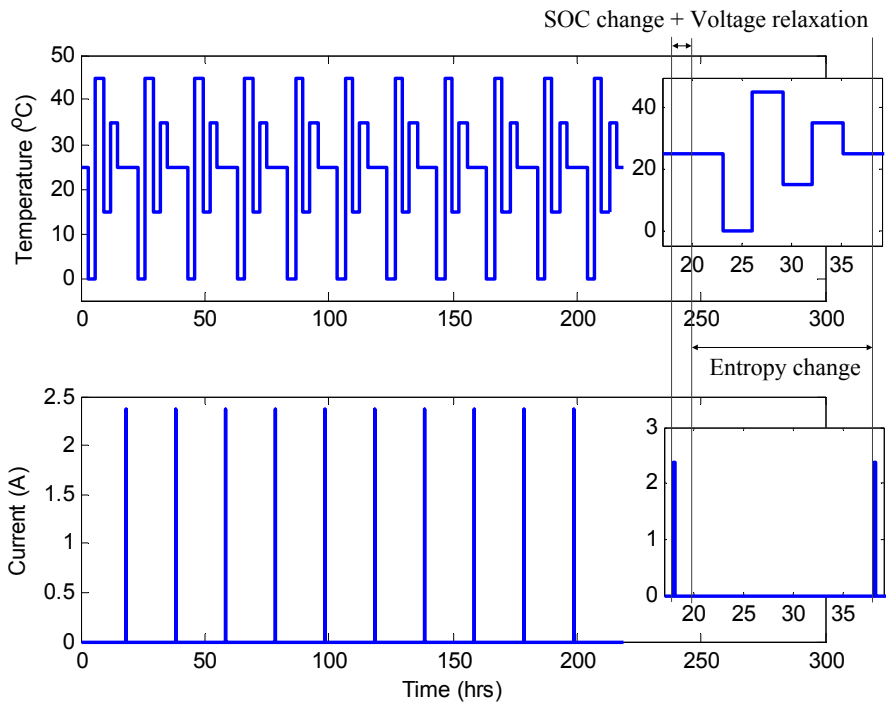

(a)

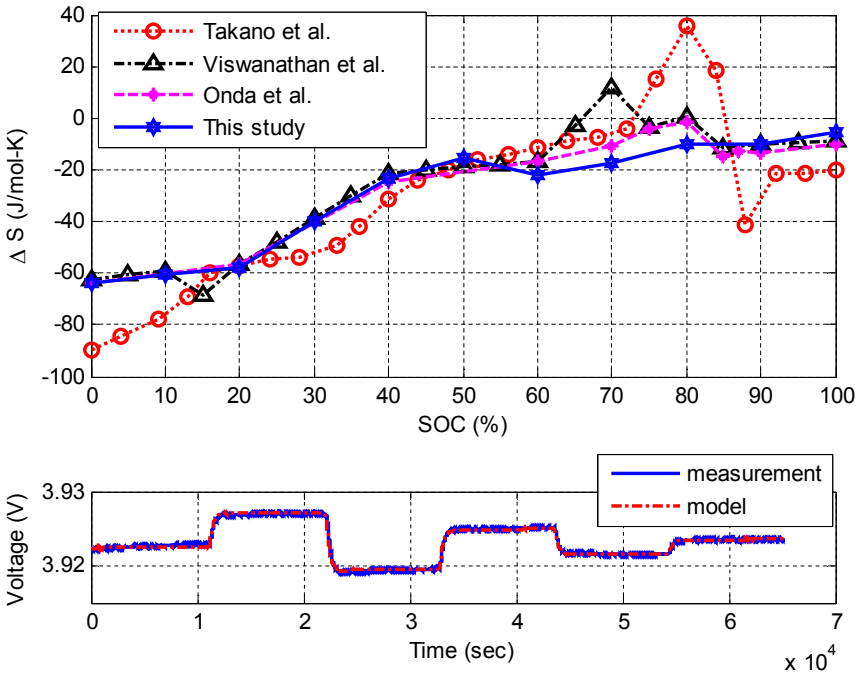

(b)

Figure 4.2: Experimental design and measured entropy change of the battery: (a) ambient temperature profile (top) and current profile (bottom), (b) comparison with literature values [83, 88, 90](top) and measured and simulated open circuit voltage at 70% SOC (bottom)

Figure 4.2(a) illustrates the experimental set-up in this study for characterizing entropy change. The battery is fully charged at a rate of C/20 at 25°C using a Constant Current Constant Voltage (CCCV) protocol with a cutoff current rate of C/100. The temperature in the thermal chamber is controlled as shown in Fig. 4.2(a). The zig-zag manner of changing temperature is designed to minimize negative influences by long thermal excursion at higher or lower temperatures than room temperature of 25°C. The battery is allowed to rest for three hours at each temperature to equilibrate. To change the SOC of the battery by 10%, a current at a rate of 1C is applied to the battery for six minutes at 25°C that is followed by two hours of rest for charge equilibrium.

Figure 4.2(b) shows the entropy change of the $LiCoO_2/LiC_6$ battery in this study and compares the values from the literature [83, 88, 90]. The entropy change of the battery in this study within the SOC range of 60% to 80% is estimated differently compared to values in other studies. Clearly some batteries in these studies show an endothermic behavior while the others display an exothermic process during battery discharge. In particular, the battery in this study does not have endothermic process, leading to a higher total heat generation during battery discharge than batteries in [83, 88, 90]. Figure 4.2(b) also compares measured and predicted open circuit voltages of the battery at 70% SOC, providing that the measured entropy change of the battery is reasonably accurate.

4.2.2 Identifying Thermal Properties

To predict the temperature of the battery, thermal parameters, namely heat capacity c_p and convection coefficient h are to be identified. Parameter identification is performed as follows – a current profile such as the one presented in Fig. 4.3(a) is applied to the battery placed in a temperature controlled chamber, and its surface temperature, terminal voltage and current are measured as shown in Fig. 4.3(a)–(c). The time constant of the thermal system α is approximated from the relaxation data following the initial constant current phase. Imposing the relation between h and c_p in Eq. (4.3) as an equality constraint, the parameterization is formulated in the form of optimization problem by using data collected during discharge operation as follows

$$\min_{c_p} \quad J = ||\hat{T}(c_p) - T|| \tag{4.5a}$$

$$\text{subject to} \quad hA_\text{b} + \alpha M c_p = 0, \tag{4.5b}$$

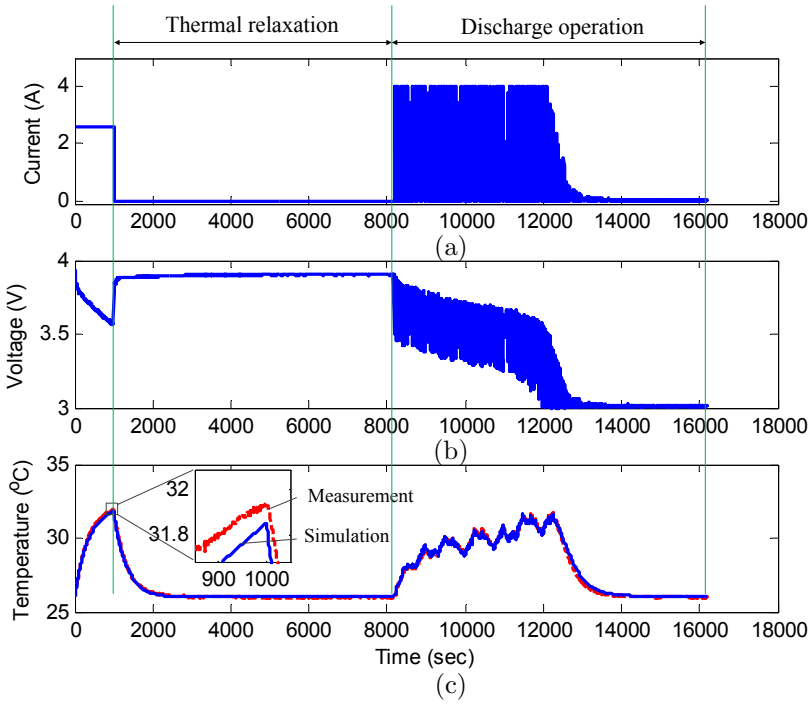

Figure 4.3: Measurement data used for thermal parametrization: (a) current, (b) voltage, (c) temperature

where T and $\hat{T}$ are measured and predicted temperatures, respectively. It is noted that heat generation is calculated from measurement data such as current and voltage using Bernardi's simplified form in [53], as discussed in Chapter II.

The optimization problem is implemented and solved in MATLAB using the built-in function *fmincon* [92]. The heat capacity of SONY 18650 batteries, which have similar chemistries to the e-Moli ICR 18650 batteries under consideration, can be found in open literature [69]. Even though the chemistry and dimension of these batteries are the same, the values for heat capacity c_p lie between 836 and 1280 J/kg/K. In this study, c_p=1000 J/kg/K is chosen as an initial value to the optimization problem. The identified parameters c_p and h are 1248 J/kg/K and 42.9 W/m^2/K respectively. As demonstrated in Fig. 4.3(c), the parameterized thermal model can provide accurate prediction of the temperature during battery operation.

4.2.3 Model Validation

To validate the performance of the parameterized model, the battery was tested under a different cycle (Fig. 4.4(a)). This cycle consists of repeated current profiles obtained from a mobile robot during a certain segment of movement provided in [93]. The corresponding battery SOC is illustrated in Fig. 4.4(b). The battery

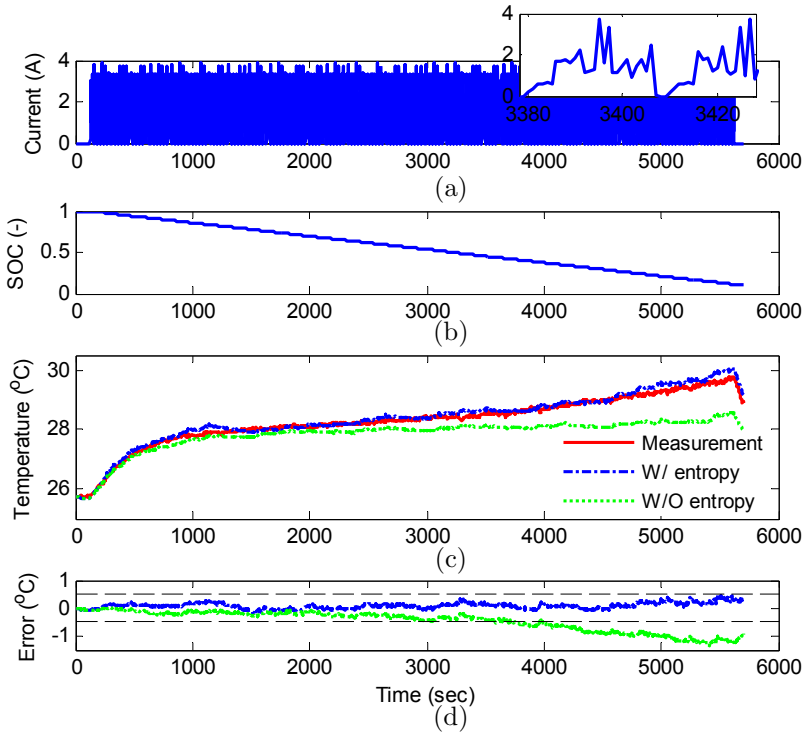

Figure 4.4: Validation of the thermal model using repeated robot operations: (a) current, (b) SOC, (c) temperature, (d) temperature error

was discharged from 100% to 10%. Figure 4.4(c) shows comparison among measured temperature and predicted temperatures with and without considerations of entropic heat generation. When entropic heat is considered in the calculation of the total heat generation, the error is bounded within $\pm$ 0.5°C. As shown early in Fig. 4.2(b), the change in entropy of the reaction is smaller at high SOC than at low SOC. Therefore, as the battery is discharged, the contribution of entropy change becomes very evident. In particular, the RMSE of the predicted temperatures with and without considerations of entropic heat generation are 0.1°C and 0.6°C, respectively (Fig. 4.2(b)(d)). The error between the measurements and predicted temperature with considerations of entropy change is considerably less than the sensor accuracy of 0.5°C. Thermocouples used for temperature measurements are T-type whose accuracy is the maximum of 0.5°C or 0.4% according to technical information from the manufacturer, OMEGA. Consequently, it can be concluded that the parameterized model is sufficiently accurate for the development of battery power management strategies.

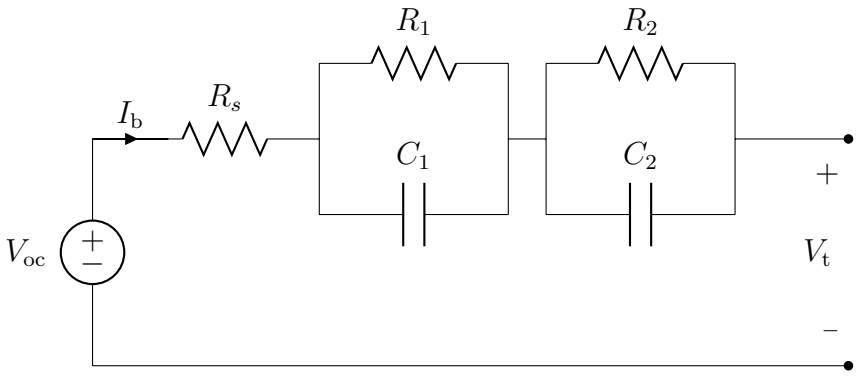

Figure 4.5: An equivalent-circuit model: OCV-R-RC-RC

4.3 Electrical Model

In control applications, an equivalent-circuit model, as illustrated in Fig. 4.5, is favored owing to its simplicity and has been shown to be reasonably capable of emulating the dynamics of a battery [49, 51, 94]. In this study, the equivalent-circuit model is used and the electrical system is described by

$$\dot{\mathrm{SOC}} = -\frac{I_\mathrm{b}}{3600 C_\mathrm{b}}, \tag{4.6a}$$

$$\dot{V}_i = -\frac{1}{R_i C_i} V_i + \frac{1}{C_i} I_\mathrm{b}, \;\; i \in \{1, 2\}, \tag{4.6b}$$

$$V_\mathrm{t} = V_\mathrm{oc}(\mathrm{SOC}) - R_s I_\mathrm{b} - \sum_{i=1}^{2} V_i, \tag{4.6c}$$

where C_b represents the estimated capacity of the battery.

Parameters R_s, R_1, R_2, C_1 and C_2 are identified using pulse tests described in [49,94]. As these parameters are functions of temperature and SOC, a two dimensional look-up table is used to schedule the model parameters [49]. Figures 4.6(b) and (c) present a comparison between measured and simulated battery terminal voltages using the current profile employed in Fig. 4.3. The electrical submodel is validated independently using measured temperatures as shown in Fig. 4.6(a). It is observed that the error in the simulated voltage is less than 5% of the total variation in terminal voltage.

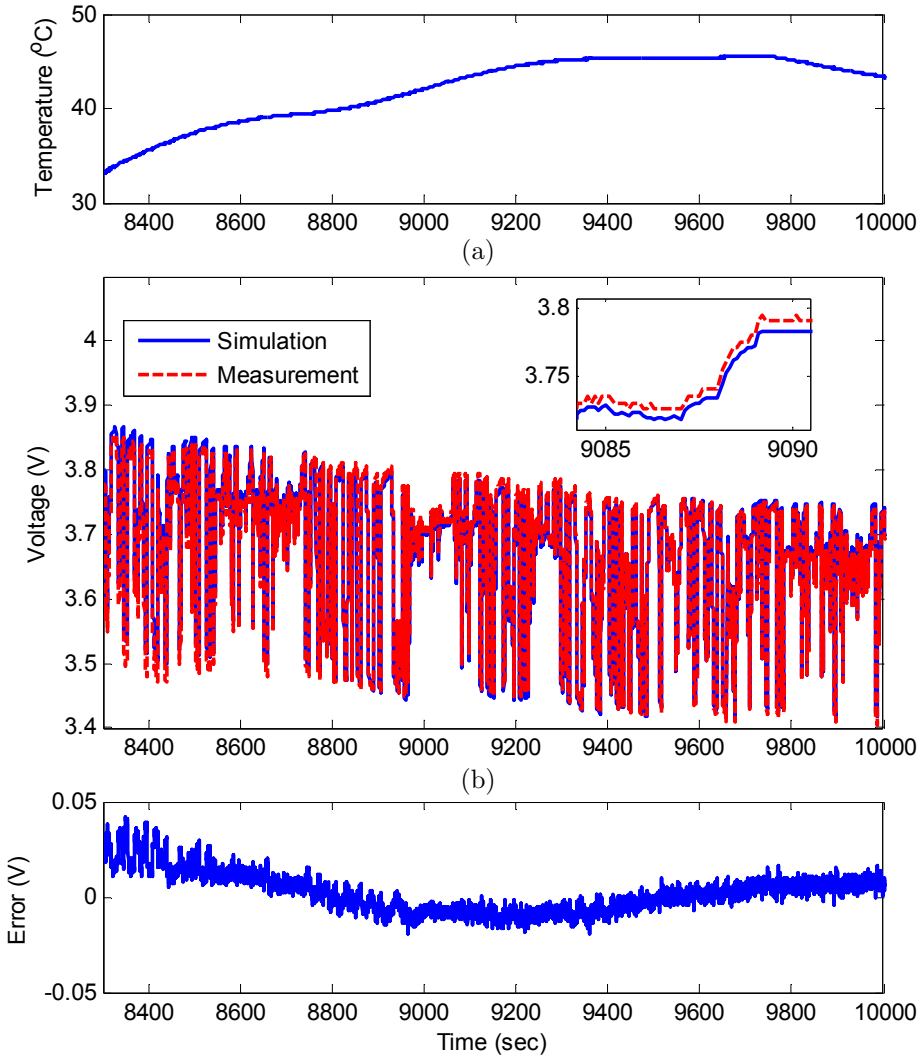

Figure 4.6: Validation of the electrical model and its performance under varying temperatures: (a) temperature, (b) voltage, (c) voltage error

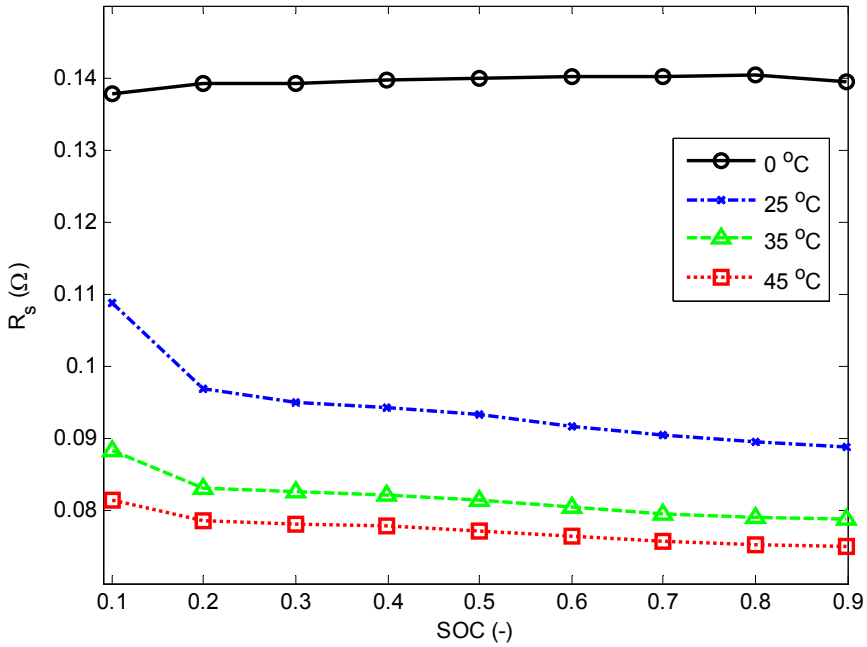

Figure 4.7: Temperature dependence of the internal resistance at various SOCs

4.4 Power Capability Estimation Method

In this section, a computationally simple but effective method to estimate power capability is described. In estimating power capability, the following factors are considered

- The thermal and electrical dynamics of a Li-ion battery are intrinsically coupled.
- The internal resistance and the rate of change in the internal resistance decrease with increasing temperatures (Fig. 4.7).
- For a galvanostatic operation (or a constant current operation), any arbitrary increase in battery temperatures will cause reduced internal losses, and subsequently generate less heat.
- Over a reasonably short horizon, the temperature increase can be assumed to be bounded and similar arguments can be made for the change in the electrical quantity, SOC.

The above statements are valid insofar as the temperature of the battery does not exceed the threshold temperature at which thermal runaway is initiated [49, 95]. Since thermal dynamics are much slower than electrical dynamics, it follows that

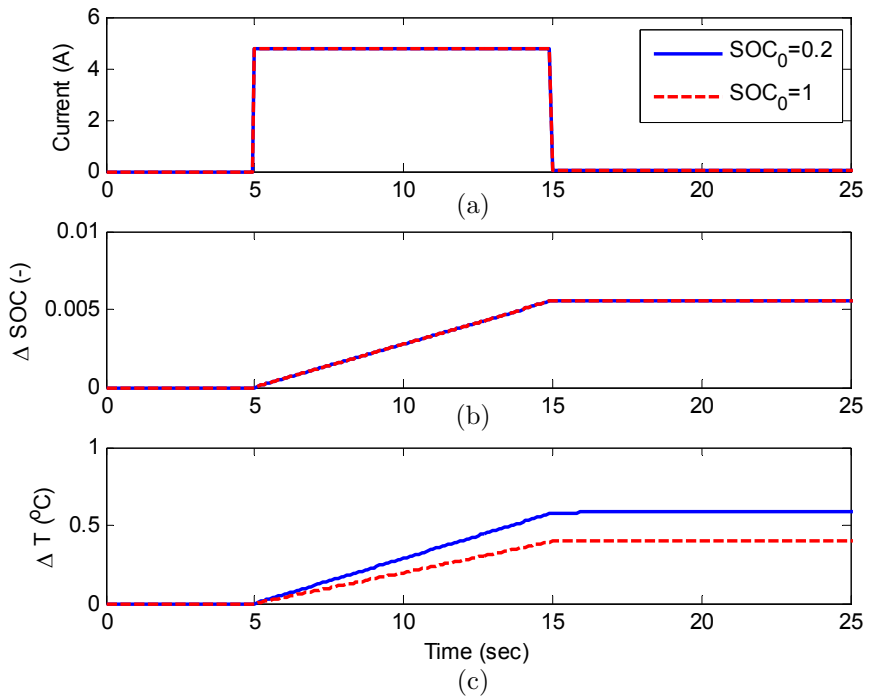

Figure 4.8: Simulated SOC and temperature changes under 2C discharge rate for ten seconds: (a) current, (b) $\Delta\text{SOC} = \text{SOC} - \text{SOC}_\text{o}$, (c) $\Delta T = T - T_\text{o}$

over a short horizon, in estimating power capability, considering electrical and thermal constraints independently yield conservative estimates. As a consequence, the thermal and electrical constraint problems are addressed separately.

To test the validity of last statement, a simulation study is conducted. The electro-thermal model is discharged at 2C rate, which is the manufacturer specified limit, for 10 seconds as illustrated in Fig. 4.8(a). Ambient temperature and convection coefficient are set to 25°C and 6W/m^2/K respectively. Note that two different initial SOC values are considered since the entropy change of the battery is six times larger at SOC of 0.2 than at SOC of 1. Figure 4.8(b) and (c) show that the maximum values of changes in SOC and temperature are 0.0056 and 0.6°C, respectively. In particular, 0.6°C change in temperature corresponds to 0.2% change in a unit of K. Therefore, it can be concluded that the assumptions of constant temperature and SOC are reasonable. This valid argument will benefit us to handle the nonlinearity in the expression of heat generation rate.

To solve each constraint problem, the Algebraic Propagation (AP) method is utilized. The AP method, based on iteration and inversion of a dynamic model, allows ones to estimate the maximal value of input ensuring that no constraints are violated.

Consider a linear discrete-time model whose dynamics are described by the following set of difference equations

$$x_{k+1} = Ax_k + Bu_k + G, \tag{4.7a}$$

$$y_k = Cx_k + Du_k + H \tag{4.7b}$$

where system matrices, which are denoted by A, B, C, D, G and H, are obtained through linearization and discretization processes around the operating point $(x_\mathrm{o}, u_\mathrm{o})$ at each sampling time. Following this notation, the linearized system matrices of the electrical and thermal models are denoted with superscripts or subscripts of E and T, respectively. For example, the discrete state transition matrix of the thermal model is denoted by A_T.

For a constant input $\overline{u}$, the state x and output y after N future steps are written as

$$x_{k+N} = A^N x_k + \sum_{i=0}^{N-1} A^i B\overline{u} + \sum_{i=0}^{N-1} A^i G, \tag{4.8a}$$

$$y_{k+N} = Cx_{k+N} + D\overline{u} + H. \tag{4.8b}$$

Therefore, at any instant k, the maximum permissible input that does not violate a constraint $\bar{y}$ on the output y in N future steps is determined by

$$\overline{u} = \left(\sum_{i=0}^{N-1} CA^i B + D \right)^{-1} \left(\bar{y} - CA^N x_k - \sum_{i=0}^{N-1} CA^i G - H \right) \tag{4.9}$$

Since the power capability is determined by using information on current limits and terminal voltage as addressed in [25–30], Eq. (4.9) will be used to determine the maximum current accounting for thermal and electrical constraints in the following sections.

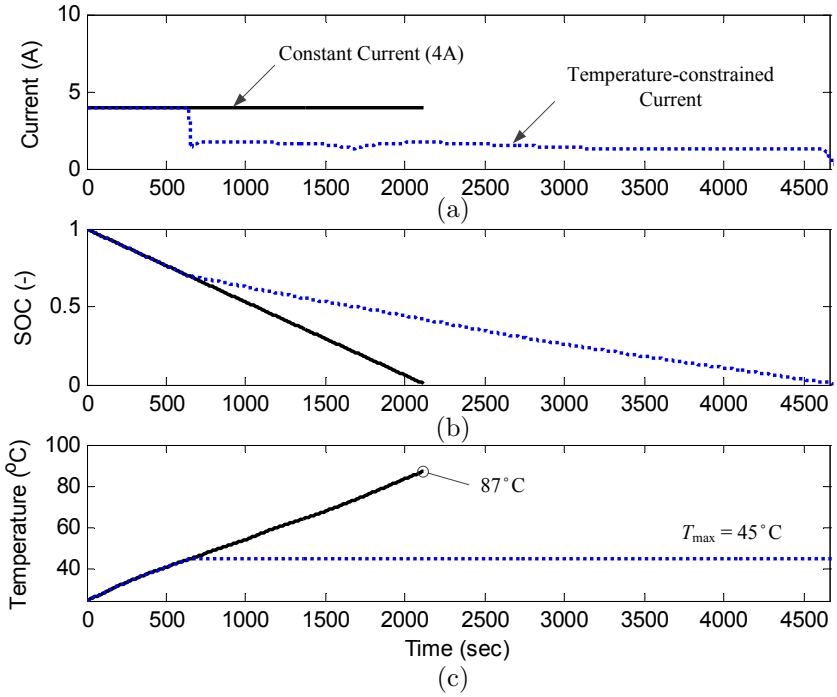

Figure 4.9: Performance of current limiting for temperature control during constant current operation at 25°C ambient temperature and natural convection ($6\text{W/m}^2\text{/K}$): (a) current, (b) SOC, (c) temperature

4.4.1 Active Thermal Constraints

The thermal dynamics in discrete-time domain with a sampling period Δt can be captured by the following equation:

$$x_{T,k+1} = A_T x_{T,k} + v_k, \tag{4.10a}$$

$$y_{T,k} = x_{T,k}, \tag{4.10b}$$

where $A_T = 1 + \alpha\Delta t$. The virtual input, v, is defined as

$$v_k = \Delta t(\beta_k x_{T,k} u_k + \gamma_k u_k^2 + \eta_k). \tag{4.11}$$

Then, the maximum of the virtual input, $\overline{v}_k$, described by considering the maximum operating temperature, $\overline{T}$, is obtained from the following equation.

$$\overline{v}_k = \left(\sum_{i=0}^{N-1} C_T A_T^i\right)^{-1} \left(\overline{T} - C_T A_T^N x_{T,k}\right). \tag{4.12}$$

When the maximal value of current is less than 2C and the prediction period is less than 10 seconds, the SOC and temperature of the battery do not change significantly over the prediction horizon as shown in Section 4.4. Thus, it is reasonable to assume that the entropy change and internal resistance are constant over the prediction horizon, that is, $\beta_{j|k}x_{T,j|k} \approx \beta_k x_{T,k}$ and $\gamma_{j|k} \approx \gamma_k$ for $j = k, k+1, \ldots, k+N$. Moreover, ambient temperature is assumed not to change rapidly and hence to be constant, i.e. $\eta_{j|k} \approx \eta_k$ for $j = k, k+1, \ldots, k+N$. These assumptions make it easy to handle the nonlinearity in the expression of heat generation rate using a quadratic term $\gamma_k u_k^2$ and a bilinear term $u_k x_{T,k}$.

By substituting Eq. (4.12) into Eq. (4.11), the maximum permissible currents during battery discharge and charge are determined respectively by following equations

$$I_{\mathrm{b,max},k}^{T,\mathrm{dch}} = \frac{-\overline{\beta}_k + \sqrt{\overline{\beta}_k^2 - 4\gamma_k(\eta_k - \overline{v}_k/\Delta t)}}{2\gamma_k}, \tag{4.13a}$$

$$I_{\mathrm{b,min},k}^{T,\mathrm{chg}} = \frac{-\overline{\beta}_k - \sqrt{\overline{\beta}_k^2 - 4\gamma_k(\eta_k - \overline{v}_k/\Delta t)}}{2\gamma_k}, \tag{4.13b}$$

where $\overline{\beta}_k = \beta_k x_{T,k}$. Superscripts *dch* and *chg* present battery discharge and charge, respectively.

To investigate the efficacy of Eqs. (4.13a) and (4.13b) in controlling temperature, a simulation study is conducted. In the simulation, the sampling frequency is set at 10 Hz with a 100 sample prediction horizon. Figures 4.9(a)–(c) show the current drawn from the battery, the corresponding SOC and battery temperature profiles. It is noted that the battery temperature increases up to 87°C without limiting current rate. On the other hand, the battery temperature remains well around the designated maximal operating temperature of 45°C when current is limited. Due to temperature-constrained current, as shown in Fig. 4.9(c), the completion time increases from 2133 seconds to 4687 seconds.

4.4.2 Active Electrical Constraints

The electrical dynamics in discrete-time domain can be expressed as

$$x_{E,k+1} = A_E x_{E,k} + B_E u_k, \tag{4.14a}$$

$$y_{E,k} = C_E x_{E,k} + D_E u_k + H_E, \tag{4.14b}$$

where the state and output are defined as $x_E = [\text{SOC}\ \ V_1\ \ V_2]^T$ and $y_E = [\text{SOC}\ \ V]^T$, respectively.

System matrices A_E, B_E, C_E, D_E and H_E are calculated by

$$A_E = \begin{bmatrix} 1 & 0 & 0 \\ 0 & e^{\frac{-\Delta t}{R_1 C_1}} & 0 \\ 0 & 0 & e^{\frac{-\Delta t}{R_2 C_2}} \end{bmatrix}, \tag{4.15a}$$

$$B_E = \begin{bmatrix} -\frac{\Delta t}{3600 C_\text{b}} \\ R_1 \left(1 - e^{\frac{-\Delta t}{R_1 C_1}}\right) \\ R_2 \left(1 - e^{\frac{-\Delta t}{R_2 C_2}}\right) \end{bmatrix}, \tag{4.15b}$$

$$C_E = \begin{bmatrix} 1 & 0 & 0 \\ \left.\dfrac{\partial V_\text{oc}}{\partial \text{SOC}}\right|_{\text{SOC}_\text{o}} & -1 & -1 \end{bmatrix}, \tag{4.15c}$$

$$D_E = \begin{bmatrix} 0 \\ -R_s \end{bmatrix}, \tag{4.15d}$$

$$H_E = \begin{bmatrix} 0 \\ V_\text{oc}(\text{SOC}_\text{o}) - \left.\dfrac{\partial V_\text{oc}}{\partial \text{SOC}}\right|_{\text{SOC}_\text{o}} \text{SOC}_\text{o} \end{bmatrix}, \tag{4.15e}$$

where SOC_o is the battery SOC at previous sampling time $(k-1)$ about which the system is linearized.

By applying Eq. (4.9), the maximum permissible current accounting for electrical constraints such as SOC and voltage limits, $\overline{\text{SOC}}$ and $\overline{V}$, is determined respectively by using Eqs. (4.16a) and (4.16b),

$$I^{E,\overline{\text{SOC}}}_{\text{b,max},k} = \left(\sum_{i=0}^{N-1} C_{E1} A_E^i B_E + D_{E1}\right)^{-1} \left(\overline{\text{SOC}} - C_{E1} A_E^N x_{E,k} - H_{E1}\right), \tag{4.16a}$$

$$I^{E,\overline{V}}_{\text{b,max},k} = \left(\sum_{i=0}^{N-1} C_{E2} A_E^i B_E + D_{E2}\right)^{-1} \left(\overline{V} - C_{E2} A_E^N x_{E,k} - H_{E2}\right), \tag{4.16b}$$

where subscripts 1 and 2 denote the row indices of system matrices corresponding to SOC and terminal voltage respectively. The overall maximum permissible current is determined by comparing Eqs. (4.13) and (4.16).

4.4.3 Power Capability Estimation

The power capability accounting for all constraints is estimated by the product of the maximum allowable current and terminal voltage. Maximum discharge and charge currents accounting for all constraints are calculated with

$$I^{\text{dch}}_{\text{b,max},k} = \min\{I^{E,\text{SOC}_{\min}}_{\text{b,max},k}, I^{E,V_{\min}}_{\text{b,max},k}, I^{T,\text{dch}}_{\text{b,max},k}\}, \tag{4.17a}$$

$$I^{\text{chg}}_{\text{b,min},k} = \max\{I^{E,\text{SOC}_{\max}}_{\text{b,min},k}, I^{E,V_{\max}}_{\text{b,min},k}, I^{T,\text{chg}}_{\text{b,min},k}\}. \tag{4.17b}$$

It is noteworthy that Eqs. (4.17a) and (4.17b) can be considered as general solutions that can be made specific to the load governor/regulator problem by choosing an appropriate prediction horizon and sampling frequency.

Therefore, the maximum power capability of the battery $\{P_{\text{b,max},k}, P_{\text{b,min},k}\}$ is obtained as follows

$$P_{\text{b,max},k} = I^{\text{dch}}_{\text{b,max},k} \cdot V^{\text{dch}}_{k+N|k}, \tag{4.18a}$$

$$P_{\text{b,min},k} = I^{\text{chg}}_{\text{b,min},k} \cdot V^{\text{chg}}_{k+N|k}, \tag{4.18b}$$

where the terminal voltage after N future sample steps $V^{q}_{k+N|k}$ is calculated with

$$\begin{aligned} V^{\text{dch}}_{k+N|k} = V_{\text{oc}} &\left(\text{SOC}_k - \frac{I^{\text{dch}}_{\text{b,max},k} N\Delta t}{3600 C_{\text{b}}}\right) - I^{\text{dch}}_{\text{b,max},k} R_s \\ &- \sum_{i=1}^{2} \left(e^{\frac{-N\Delta t}{R_i C_i}} V_{i,k} + I^{\text{dch}}_{\text{b,max},k} R_i \left(1 - e^{\frac{-N\Delta t}{R_i C_i}}\right)\right), \end{aligned} \tag{4.19a}$$

$$\begin{aligned} V^{\text{chg}}_{k+N|k} = V_{\text{oc}} &\left(\text{SOC}_k - \frac{I^{\text{chg}}_{\text{b,min},k} N\Delta t}{3600 C_{\text{b}}}\right) - I^{\text{chg}}_{\text{b,min},k} R_s \\ &- \sum_{i=1}^{2} \left(e^{\frac{-N\Delta t}{R_i C_i}} V_{i,k} + I^{\text{chg}}_{\text{b,min},k} R_i \left(1 - e^{\frac{-N\Delta t}{R_i C_i}}\right)\right). \end{aligned} \tag{4.19b}$$

4.5 Simulation Results

In this section, we investigate the performance of the proposed model-based method to estimate power capability through a battery simulation with a predic-

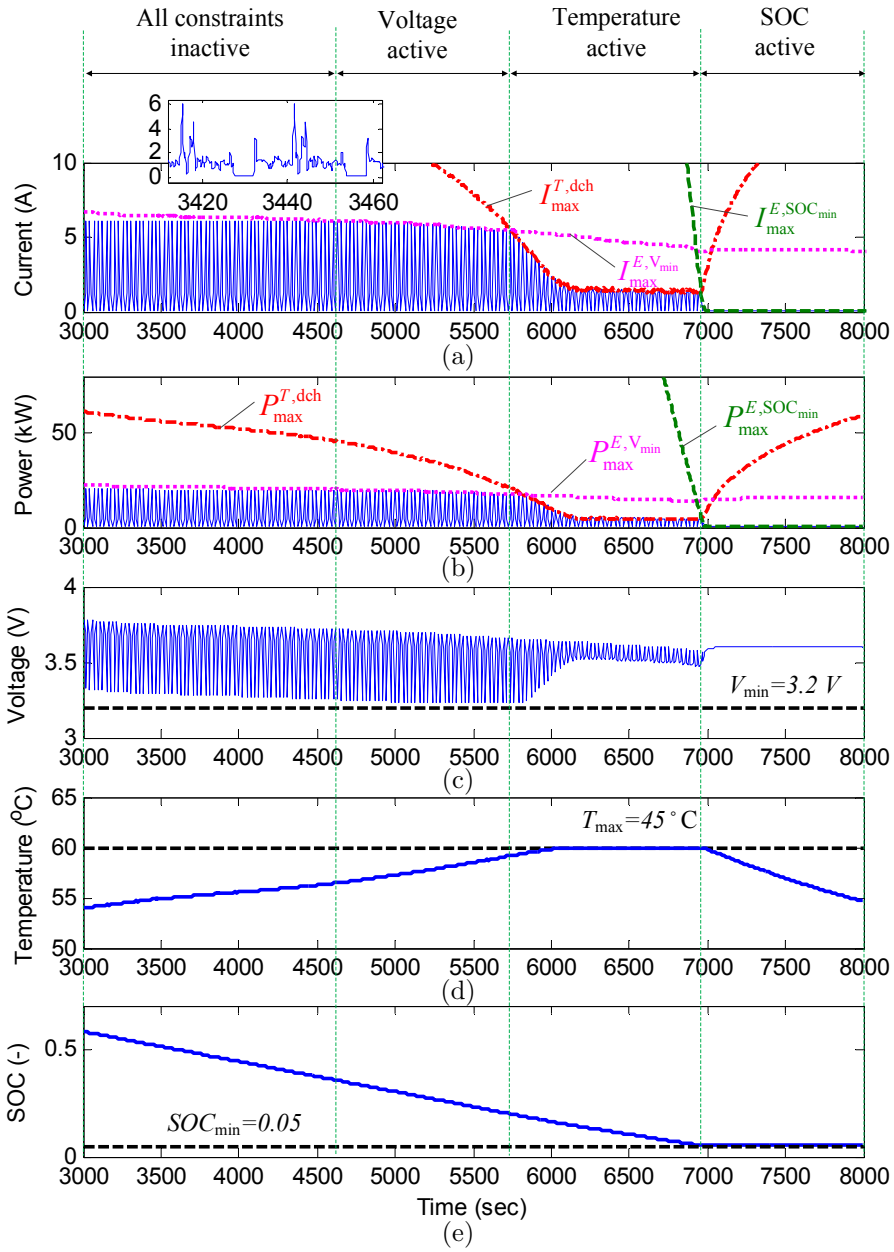

Figure 4.10: Performance of power capability estimation method during repeated operations at 30°C ambient temperature and natural convection (6 W/m^2/K): (a) current, (b) power, (c) voltage, (d) temperature, (e) SOC

tion horizon of 10 seconds and a 10 Hz sampling frequency. Figure 4.10(a) illustrates repeated discharge duty cycles provided in [93]. Figures 4.10(b)–(e) show the estimated power capabilities and actual power drawn from the battery, corresponding terminal voltage, battery temperature and SOC profiles, respectively. The ambient temperature is assumed to be 30°C and natural convection is considered (6 W/m^2/K). The electrical and thermal constraints are shown in Fig. 4.10(c)–(e).

It is noted that all constraints are inactive initially, that is, the battery voltage, temperature and SOC do not exceed $V_{\min}$, $T_{\max}$, and $\mathrm{SOC}_{\min}$ respectively. Hence, the battery can provide the power requested up to 4705 second until the voltage constraint is violated. As the power is drawn from the battery, the battery SOC is reduced as seen from Fig. 4.10(e). Due to the corresponding decrease in open circuit voltage and voltage drop caused by internal resistances, the power is limited by the voltage-constrained power capability so that the terminal voltage is higher than the minimum limit of 3.2 V as shown in Fig. 4.10(c) from 4705 to 5740 second.

As the battery temperature approaches to the maximum temperature limit, the power capability is determined by the maximum temperature limit. Hence, as illustrated in 4.10(d), the battery temperature remains below 45°C until SOC constraint becomes active. This performance highlights that the proposed method is capable of estimating power capability accounting for thermal and electrical constraints and thus safe and reliable operation of the battery is achievable.

4.6 Conclusion

In this chapter a method to estimate battery power limits accounting for both electrical and thermal constraints is presented. The method relies on an electro-thermal model for the electrical and thermal dynamic behaviors. Further, a method to parameterize the lumped thermal model that includes entopic heat generation as well as joule heating is presented and discussed. Under the assumptions of short prediction horizons, the power capability estimation problem is broken into a current limiting problem under two weakly coupled constraints – thermal and electrical. A computationally efficient algorithm is proposed that is able to exploit the time scale separation of the electrical and thermal dynamics.

CHAPTER V

Case Study : a Series Hybrid Electric Vehicle

5.1 Introduction

The primary task of a supervisory controller or power management system (PMS) is to determine the power flow among hybrid powertrain components to minimize fuel consumption and emissions. Li-ion batteries have become one of the most critical components in hybrid electric vehicles due to their high specific power and energy density. The performance and longevity of these batteries rely on constraining their operation such that voltage and temperature are regulated within prescribed intervals. In particular, power capability of Li-ion batteries is considerably reduced at low state-of-charge and temperature, whereas battery degradation is accelerated at high temperature [19, 96, 97]. Therefore, the PMS must be aware of constraints of the system not only to ensure reliable and safe operation, but also to maximize resource utilization.

This chapter considers a battery power management strategy for hybrid electric vehicles by including the radial temperature distribution inside a cylindrical battery and a convective cooling condition along with electrical dynamics. To provide accurate information about the battery to the PMS, state-parameter estimators are developed by applying Filtering algorithms, namely a Dual Extended Kalman Filter and Dual Kalman Filter for electrical and thermal dynamics respectively. Model-in-the-loop simulations are conducted using a series hybrid electric vehicle (SHEV) simulator to demonstrate the effectiveness of the proposed method.

This chapter is organized as follows: Section 5.2 addresses the formulation of a Model Predictive Control based power management strategy in the SHEV. Section 5.3 presents an estimation algorithm to determine power capability accounting for electrical and thermal constraints of the battery. Development of state-parameter

estimators for electrical and thermal dynamics is also described. Section 5.4 presents and discusses simulation results, and conclusions are drawn in Section 5.5.

5.2 Power Management System

5.2.1 Background

Diesel engines are the preferred engine technology in heavy-duty commercial and military applications due to their high performance in terms of fuel economy, torque at low speed, and power density [98]. However, their soot emissions lead to environmental concerns in commercial applications, as well as survivability concerns in military applications due to visual signature. Aggressive transients worsen soot emissions [99] due to a turbocharger lag which corresponds to the slow air-path dynamics of a diesel engine with a time constant of a few seconds [100].

One approach to reduce soot emissions is to leverage the hybrid powertrain technology. Hybrid technology has been successfully deployed on some passenger vehicles, improving fuel economy and reducing tailpipe emissions [101], [102], and vehicles with diesel engines can benefit from hybridization, as well [103].

Among the various topologies for vehicle hybridization, such as series [104, 105], parallel [106], [107], and power-split [108], [109], this study focuses on a series hybrid electric architecture with a military context in mind. The series hybrid electric technology is considered in military vehicles due to stringent requirements for silent watch, increased mobility, enhanced functionality for on-board power, improved export power capabilities, and the potential for minimal visual signature. The series configuration offers greater flexibility in vehicle design such as the V-shaped hull to maximize crew survivability during blast events [110].

Within the context of series hybrid electric vehicles (SHEV), different power management strategies have been developed to successfully alleviate the tradeoff between fuel economy and soot emissions. For example, Filipi and Kim [104] proposed a modulated battery state-of-charge (SOC) control using a Proportional-Integral (PI) feedback control. Konev *et al.* [111] and Kim *et al.* [112] used low-pass filtering for splitting the power demand. Even though these methods result in smooth engine operations, the engine power rate is not strictly considered as a constraint for engine operations. A power constraint was explicitly handled in [9] where a smooth engine operation was achieved by applying a Model Predictive Control (MPC) while accounting for an input constraint of the maximum engine-generator power rate. The results in [9] also show the comparison between the MPC-based power management

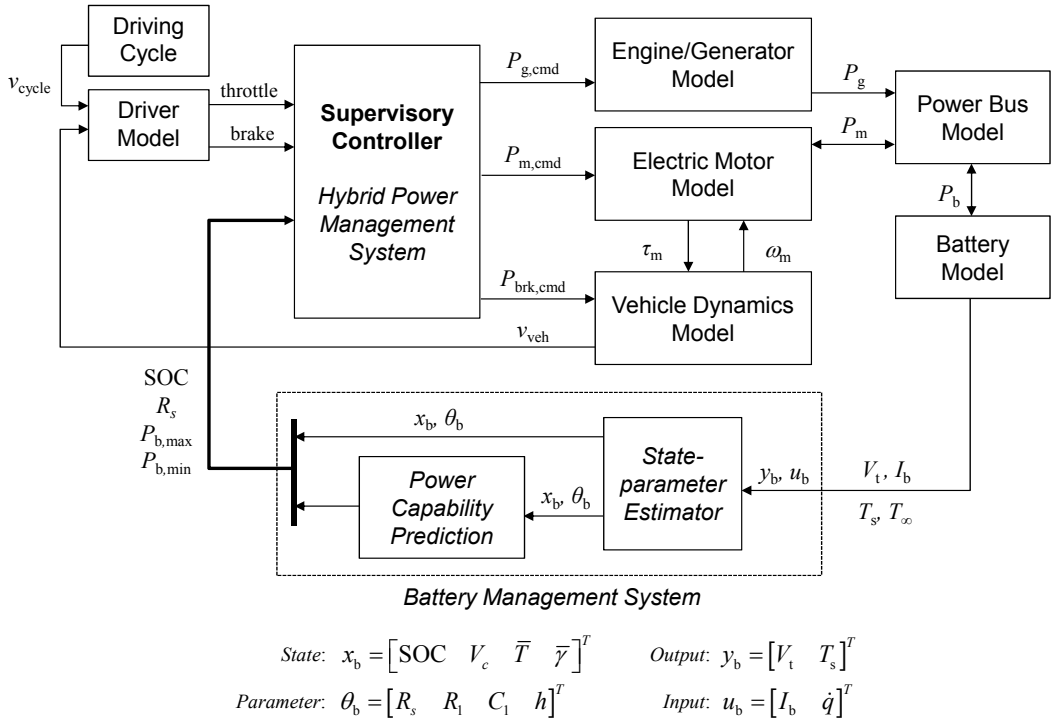

Figure 5.1: Schematic of power and battery management systems in a SHEV simulation framework

strategy and Dynamic Programming in terms of fuel economy. However, the influence of smooth engine operations on emissions reduction has not been investigated.

Thus, in this study, to achieve a reduction in soot, the maximum engine-generator power rate is allowed to vary based on the engine-generator power. Empirical knowledge of the operation of a turbocharged diesel engine suggests that the allowable power rate decreases as the engine power increases. The design of the power rate map is discussed in Appendix A.

The SHEV configuration under consideration consists of an engine, a generator, in-hub motors, a battery, a power bus, and the vehicle as illustrated in Fig. 5.1. The SHEV is simulated in a forward looking scheme, where the driver determines control commands to follow a desired speed profile. The engine drives the generator, converting mechanical power into electrical power which is then used to power electric motors and/or to charge the battery. Electrical power flow among the generator, battery, and electric motors is managed by a power management system (PMS) through the power bus. A hybridized Mine Resistant Ambush Protected All-Terrain Vehicle (M-ATV) is the target vehicle for control design and its specifications are summarized

Table 5.1: Mine Resistant Ambush Protected All-Terrain Vehicle (M-ATV) Specifications

Parameter	Symbol	Value	Unit
Weight	M_{veh}	15554	kg
Frontal Area	A_{veh}	5.72	m^2
Diesel Engine Power	P_{e}	261	kW
Generator Power	P_{g}	236	kW
Battery Capacity	C_{b}	9.27	kWh
Motor Power	P_{m}	380	kW

in Table 5.1. Detailed models for the SHEV are given in Appendix B.

5.2.2 MPC-based Power Management

For power management in the SHEV, Model Predictive Control (MPC) is used to split the power demand between the engine-generator unit and the battery. MPC is an attractive control method with advantages such as generating a suboptimal solution in a causal manner and taking into account input and state constraints over a finite horizon. In MPC, an optimal control sequence is computed at each time step by solving an on-line optimization problem over a finite future time horizon by utilizing a receding horizon approach. Then, the first element of the optimal sequence is applied to the system as a control input, and this procedure is repeated at each time step.

The supervisory control design focuses on distributing the power demand between the battery and the engine-generator and hence a simplified modeling approach is considered for the powertrain. To model the battery, a simple equivalent-circuit model with a single state is considered. As discussed in [30] and [9], the single-state equivalent-circuit model is capable of capturing the SOC dynamics of the battery, the most relevant dynamics, for the supervisory control design. Thus, the SOC dynamic behavior of the battery is simplified by the following equation:

$$\frac{d\underline{x}(t)}{dt} = -\frac{I_{\text{b}}}{3600C_{\text{b}}} \tag{5.1a}$$

$$I_{\text{b}} = -\frac{V_{\text{oc}} - \sqrt{V_{\text{oc}}^2 - 4R_{\text{s}}\underline{u}(t)}}{2R_{\text{s}}}, \tag{5.1b}$$

where $\underline{(\cdot)}$ stands for power management system level. The variable $\underline{x}$ = SOC is the

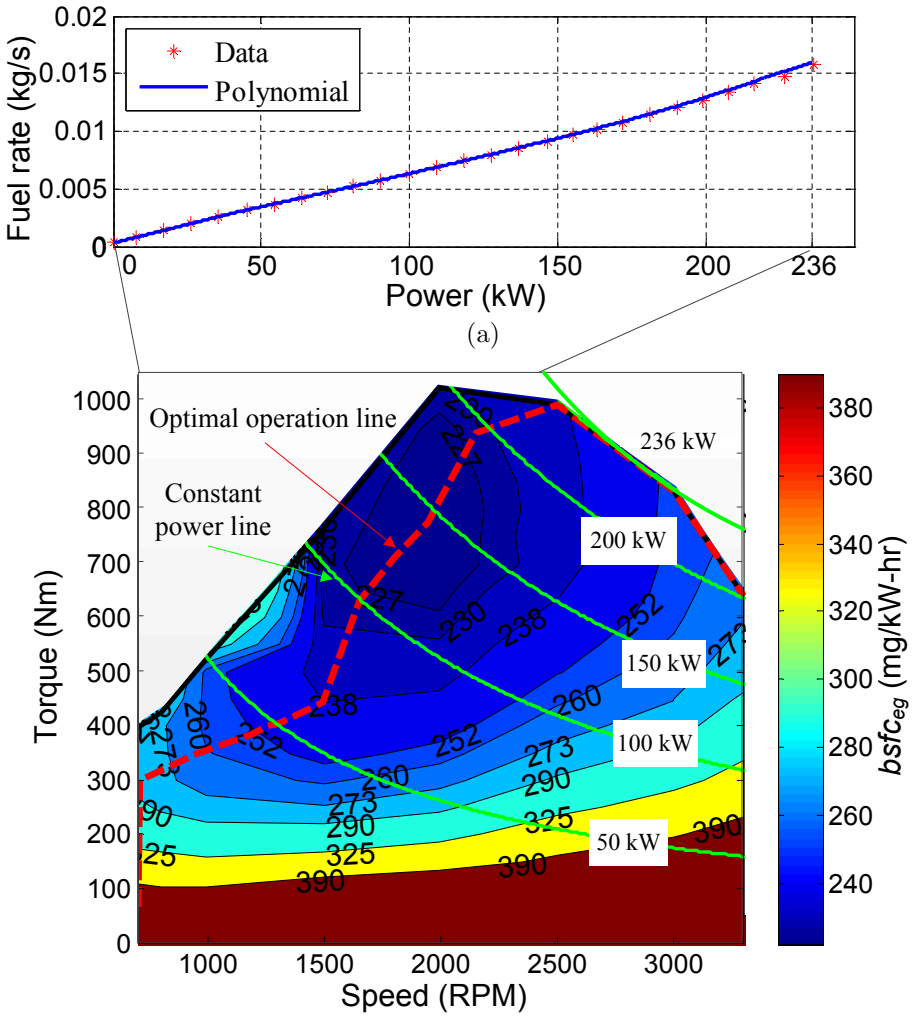

Figure 5.2: Quasi-static engine maps: (a) a steady state fuel rate as a function of engine-generator power, and (b) brake specific fuel consumption *bsfc* of the engine-generator unit superimposed by optimal operation line

state of the battery system, $\underline{u} = P_{\mathrm{b}}$ is the battery power, I_{b} is the battery current and C_{b} is the battery capacity in a unit of Ah. Variables V_{oc} and R_{s} are open circuit voltage (OCV) and internal resistance, respectively. Note that the battery SOC and internal resistance are provided by the battery management system (BMS).

To model the engine-generator, a quasi-static nonlinear map representing the relationship between power P_{g} and fuel rate $\dot{m}_f$ is used as shown in Fig. 5.2. The engine-generator power $\underline{v} = P_{\mathrm{g}}$ is calculated by

$$\underline{v}(t) = P_{\mathrm{d}}(t) - \underline{u}(t), \tag{5.2}$$

explaining how the power demand generated by the driver $P_{\mathrm{d}}(t)$ is satisfied by the sum of the battery power $\underline{u}$(t) and engine-generator power $\underline{v}(t)$. The outputs of the model are

$$\underline{y} = [\underline{x} \;\; \dot{m}_f^{0.5}]^T, \tag{5.3}$$

where the square root of fuel rate of the engine generator $\dot{m}_f^{0.5}$ is used since the MPC problem is formulated as a Quadratic Programming (QP) problem similarly to [9] (Appendix C). The fuel rate is a function of the engine-generator power (Fig. 5.2).

In summary, the nonlinear powertrain model is described in the state-space representation as following:

$$\dot{\underline{x}}(t) = \varphi(\underline{x}(t), \underline{u}(t)), \tag{5.4a}$$
$$\underline{y}(t) = \psi(\underline{x}(t), \underline{v}(t)), \tag{5.4b}$$

where $\underline{x} \in \mathbb{R}^1$, $\underline{u} \in \mathbb{R}^1$, $\underline{v} \in \mathbb{R}^1$, $\underline{y} \in \mathbb{R}^2$.

A linear discrete-time MPC control strategy is used for power management in this thesis. Since the system is nonlinear, linearization and discretization processes are required to formulate a linear MPC problem. By computing the Jacobian matrices from the nonlinear system (5.4), an approximate linear continuous-time model can be obtained as

$$\dot{\underline{x}}(t) = A\underline{x}(t) + B\underline{u}(t) + G_1, \tag{5.5a}$$
$$\underline{y}(t) = C\underline{x}(t) + H\underline{v}(t) + G_2, \tag{5.5b}$$

System matrices are calculated by

$$A = \left.\frac{\partial \varphi}{\partial \underline{x}}\right|_{(\underline{x}_{\mathrm{o}}, \underline{u}_{\mathrm{o}}, \underline{v}_{\mathrm{o}})}, \tag{5.6a}$$
$$B = \left.\frac{\partial \varphi}{\partial \underline{u}}\right|_{(\underline{x}_{\mathrm{o}}, \underline{u}_{\mathrm{o}}, \underline{v}_{\mathrm{o}})}, \tag{5.6b}$$
$$C = \left.\frac{\partial \psi}{\partial \underline{x}}\right|_{(\underline{x}_{\mathrm{o}}, \underline{u}_{\mathrm{o}}, \underline{v}_{\mathrm{o}})}, \tag{5.6c}$$
$$H = \left.\frac{\partial \psi}{\partial v}\right|_{(\underline{x}_{\mathrm{o}}, \underline{u}_{\mathrm{o}}, \underline{v}_{\mathrm{o}})}, \tag{5.6d}$$
$$G_1 = \varphi(\underline{x}_{\mathrm{o}}, \underline{u}_{\mathrm{o}}, \underline{v}_{\mathrm{o}}) - (A\underline{x}_{\mathrm{o}} + B\underline{u}_{\mathrm{o}}), \tag{5.6e}$$
$$G_2 = \psi(\underline{x}_{\mathrm{o}}, \underline{u}_{\mathrm{o}}, \underline{v}_{\mathrm{o}}) - (C\underline{x}_{\mathrm{o}} + H\underline{v}_{\mathrm{o}}). \tag{5.6f}$$

where $\underline{x}_{\mathrm{o}}$, $\underline{u}_{\mathrm{o}}$, and $\underline{v}_{\mathrm{o}}$ are the values at previous sampling time $t-1$.

Assuming the input $\underline{u}(t)$ is constant over each sampling interval, a linear discrete-time model can be obtained as

$$\underline{x}_{k+1} = A_d \underline{x}_k + B_d \underline{u}_k + G_{1d}, \tag{5.7a}$$

$$\underline{y}_k = C\underline{x}_k + H\underline{v}_k + G_2, \tag{5.7b}$$

where $A_d \approx 1 + A\Delta\underline{t}$, $B_d = B\Delta\underline{t}$, $G_{1d} = G_1\Delta\underline{t}$, and $\Delta\underline{t}$ is the sampling period in power management system.

For the purposes of MPC, the cost function J to be minimized and constraints are defined as

$$\begin{aligned} J_k = & \sum_{i=k}^{k+N_{\mathrm{p}}} (\underline{y}_{i|k} - \underline{y}^{\mathrm{ref}})^T \begin{bmatrix} \eta_1 & 0 \\ 0 & \eta_2 \end{bmatrix} (\underline{y}_{i|k} - \underline{y}^{\mathrm{ref}}) \\ & + \Delta\underline{v}_{i|k}^T \eta_3 \Delta\underline{v}_{i|k} + \underline{u}_{i|k}^T \eta_4 \underline{u}_{i|k} \end{aligned} \tag{5.8a}$$

$$\text{s.t.} \quad P_{\mathrm{b,min}} \le \underline{u}_{i|k} \le P_{\mathrm{b,max}},\ i = 1, 2, \ldots, N_{\mathrm{c}} \tag{5.8b}$$

$$P_{\mathrm{g,min}} \le \underline{v}_{i|k} \le P_{\mathrm{g,max}}, \quad , i = 1, 2, \ldots, N_{\mathrm{c}} \tag{5.8c}$$

$$\Delta P_{\mathrm{g,min}} \le \Delta\underline{v}_{i|k} \le \Delta P_{\mathrm{g,max}},\ i = 1, 2, \ldots, N_{\mathrm{c}} \tag{5.8d}$$

$$\mathrm{SOC}_{\mathrm{min}} \le \underline{y}_{i|k}^1 \le \mathrm{SOC}_{\mathrm{max}},\ i = 1, 2, \ldots, N_{\mathrm{p}} \tag{5.8e}$$

where N_{p} and N_{c} are lengths of the prediction and control horizons, respectively. The parameter η_j $(j = 1, \ldots, 4)$ represents a weighting factor for the balance between battery SOC regulation and fuel economy improvement. These weighting factors are tuned through repeated simulations until the fuel economy improvements are diminished. The variables $P_{\mathrm{g,min}}$ and $P_{\mathrm{g,max}}$ are minimum and maximum engine-generator power, respectively. The minimum and maximum power rates of the engine-generator $\Delta P_{\mathrm{g,min}}$ and $\Delta P_{\mathrm{g,max}}$ are obtained through a design optimization process presented in Appendix A. The maximum discharging and charging power limits of the battery $P_{\mathrm{b,max}}$ and $P_{\mathrm{b,min}}$ are provided by the battery management system and will be presented in Section 5.3. Parameters and constraints are provided in Table 5.2 and Fig. 5.3.

Equation (5.8) is rewritten as a QP problem:

$$\min_{\Delta\underline{U}} \quad J = \frac{1}{2}\Delta\underline{U}^T \mathbf{\Psi_1} \Delta\underline{U} + \mathbf{\Psi_2}^T \Delta\underline{U} \tag{5.9a}$$

$$\text{s.t.} \quad \mathbf{\Gamma_1}\Delta\underline{U} \le \mathbf{\Gamma_2}, \tag{5.9b}$$

Table 5.2: Parameter and Constraint Values for MPC

Parameter	Symbol	Value
Weighting Factor	η_1	4.17
	η_2	1
	η_3	2.5e-5
	η_4	1.25e-6
Horizon Length	N_c	15
	N_p	40
State Reference	$\underline{y}_1^{\mathrm{ref}}$	0.5
	$\underline{y}_2^{\mathrm{ref}}$	0
Engine Constraint	$P_{\mathrm{g,min}}$	0 kW
	$P_{\mathrm{g,max}}$	236 kW
	$\Delta P_{\mathrm{g,min}}$	-60 kW/s
	$\Delta P_{\mathrm{g,max}}$	a function of P_g shown in Fig. 5.3

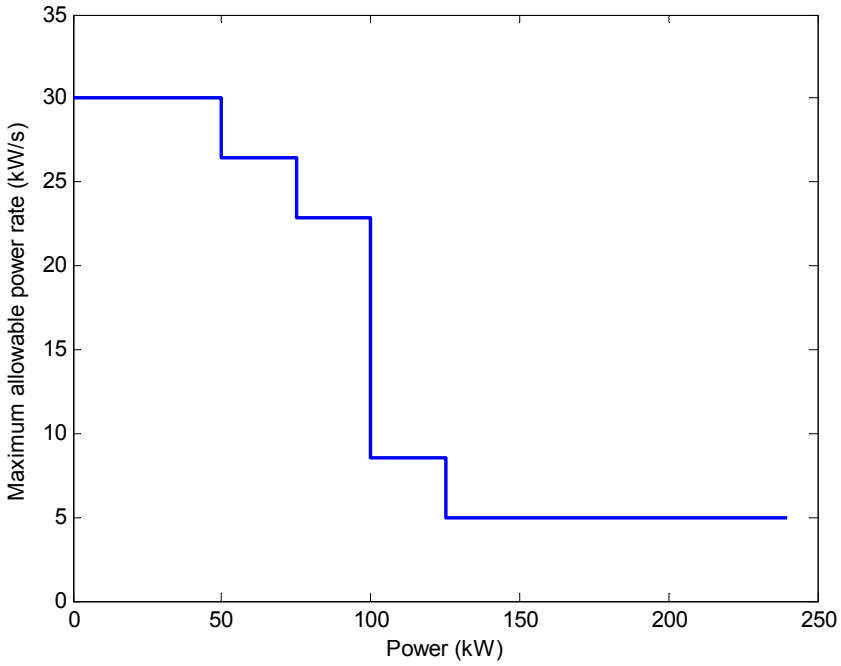

Figure 5.3: Power rate constraint map of the engine-generator; the maximum allowable power rate varies depending on the engine-generator power.

where $\Delta\underline{U} = \left[\Delta\underline{u}_{k|k}, \ldots, \Delta\underline{u}_{k+N_\mathrm{c}-1|k}\right]^T$ is the change in the input vector. The lengths of horizon for control N_c and prediction N_p are tuned based on the computation time so that the time of solving the optimization problem is less than the time step of

0.2 seconds to allow real-time simulations with the hardware in the loop. Matrices $\mathbf{\Psi_1}$, $\mathbf{\Psi_2}$, $\mathbf{\Gamma_1}$, and $\mathbf{\Gamma_2}$ are obtained by substituting Eqs. (5.2) and (5.7) into Eq. (5.8)(Appendix C).

Power demand $P_{\mathrm{d},k}$ over the prediction horizon is assumed constant,

$$P_{\mathrm{d},k+i|k} = P_{\mathrm{d},k|k}, \quad i = 1, \ldots, N_{\mathrm{p}}. \tag{5.10}$$

Even though this assumption may not be accurate, unsteady power demands can be properly handled due to the fact that only the first element of the control action sequence over the prediction horizon is used. Approaches to predict future power demand such as an exponential decay, stochastic and perfect predictions and their influence on the fuel economy are not considered in this thesis, but can be found in [113] and [114].

After solving Eq. (5.9), the first element of optimal sequence $\Delta \underline{u}^{\mathrm{opt}}_{k|k}$ is used for splitting power demand; that is, the optimal engine-generator power $\underline{v}^{\mathrm{opt}}_{k}$ is calculated by

$$\underline{v}^{\mathrm{opt}}_{k} = P_{\mathrm{d},k} - \underline{u}_{k-1} - \Delta \underline{u}^{\mathrm{opt}}_{k|k}. \tag{5.11}$$

In the following section, information about the battery, namely SOC, internal resistance and the maximum available battery power, is estimated for the PMS to solve the power distribution problem (5.8).

5.3 Battery Power Management Strategy

Battery state[1] needs to be accurately estimated to ensure efficient and robust operation of the battery. Thus, in this section, adaptive estimators are developed to sequentially identify SOC, internal resistance and core temperature of the battery along with the convection coefficient. Then, these states and parameters are used to determine power capability of the battery. The battery SOC, internal resistance and power capability are provided to the power management system. As a first step, all batteries in the battery pack are assumed to be identical.

[1]Battery states in the context of this chapter are different from *states* of a dynamic system but refer to information describing 1) how much energy is stored in a battery; 2) how high power can be drawn from or provided to a battery.

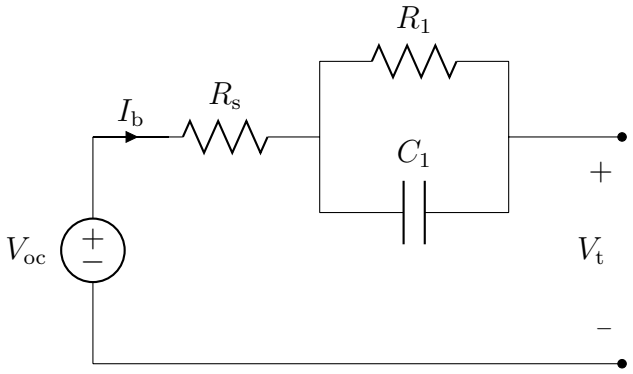

Figure 5.4: An equivalent-circuit model: OCV-R-RC

5.3.1 Control-Oriented Battery Model

Electrical dynamics of the battery is captured by an equivalent-circuit model similar to the one used in the PMS. However, a two-state model (OCV-R-RC) as shown in Fig. 5.4 is considered to accurately predict terminal voltage. As suggested in [51], this two-state model is reasonably accurate for voltage prediction in application to electrified vehicles. The electrical dynamics in discrete-time domain is given by

$$\begin{bmatrix} \mathrm{SOC}_{k+1} \\ V_{1,k+1} \end{bmatrix} = A_E \begin{bmatrix} \mathrm{SOC}_k \\ V_{1,k} \end{bmatrix} + B_E I_{b,k} \tag{5.12a}$$

$$V_{t,k} = V_{oc}(\mathrm{SOC}_k) - V_{1,k} - R_s I_{b,k} \tag{5.12b}$$

where V_t is the terminal voltage of the battery and Δt is the sampling period in battery management system. The subscript E denotes the electrical system. System matrices A_E and B_E are expressed by

$$A_E = \begin{bmatrix} 1 & 0 \\ 0 & e^{\frac{-\Delta t}{R_1 C_1}} \end{bmatrix} \tag{5.13a}$$

$$B_E = \begin{bmatrix} -\dfrac{1}{3600 C_b} \\ R_1 \left(1 - e^{\frac{-\Delta t}{R_1 C_1}}\right) \end{bmatrix} \tag{5.13b}$$

where polarization resistance and polarization capacitance are denoted by R_1 and C_1, respectively.

To predict core and surface temperatures of the battery, T_c and T_s respectively, the reduced-order model developed in Chapter II is adopted and reproduced below

for convenience:

$$\begin{bmatrix} \bar{T}_{k+1} \\ \bar{\gamma}_{k+1} \end{bmatrix} = A_T \begin{bmatrix} \bar{T}_k \\ \bar{\gamma}_k \end{bmatrix} + B_T \begin{bmatrix} \dot{q}_k \\ T_{\infty,k} \end{bmatrix} \tag{5.14a}$$

$$\begin{bmatrix} T_{\mathrm{c},k} \\ T_{\mathrm{s},k} \end{bmatrix} = C_T \begin{bmatrix} \bar{T}_k \\ \bar{\gamma}_k \end{bmatrix} + D_T T_{\infty,k} \tag{5.14b}$$

where $\bar{T}$ and $\bar{\gamma}$ represent the averaged temperature and temperature-gradient. The subscript T denotes the thermal system. Ambient temperature and the rate of heat generation are denoted by T_∞ and $\dot{q}$ respectively. Matrices of the thermal system are given by

$$A_T = \begin{bmatrix} \dfrac{hr^2 + 24k_t r - 48\alpha h \Delta t}{r(24k_t + rh)} & \dfrac{-15\alpha h \Delta t}{24k_t + rh} \\ \dfrac{-320\alpha h \Delta t}{r^2(24k_t + rh)} & \dfrac{hr^3 + 24k_t r^2 - 120\alpha \Delta t(rh + 4k_t)}{r^2(24k_t + rh)} \end{bmatrix} \tag{5.15a}$$

$$B_T \triangleq \begin{bmatrix} B_{E1} & B_{E2} \end{bmatrix} = \begin{bmatrix} \dfrac{\alpha \Delta t}{k_t V_\mathrm{b}} & \dfrac{48\alpha h \Delta t}{r(24k_t + rh)} \\ 0 & \dfrac{320\alpha h \Delta t}{r^2(24k_t + rh)} \end{bmatrix} \tag{5.15b}$$

$$C_T \triangleq \begin{bmatrix} C_{T1} \\ C_{T2} \end{bmatrix} = \begin{bmatrix} \dfrac{24k_t - 3rh}{24k_t + rh} & -\dfrac{120rk_t + 15r^2 h}{8(24k_t + rh)} \\ \dfrac{24k_t}{24k_t + rh} & \dfrac{15rk_t}{48k_t + 2rh} \end{bmatrix} \tag{5.15c}$$

$$D_T \triangleq \begin{bmatrix} D_{T1} \\ D_{T2} \end{bmatrix} = \begin{bmatrix} \dfrac{4rh}{24k_t + rh} \\ \dfrac{rh}{24k_t + rh} \end{bmatrix} \tag{5.15d}$$

where r, k_t and α are the radius, thermal conductivity and thermal diffusivity of the battery respectively.

The heat generation rate $\dot{q}_k$ is defined as

$$\dot{q}_k = I_{\mathrm{b},k}^2 R_\mathrm{s} + \frac{V_{1,k}^2}{R_1} - I_{\mathrm{b},k} \bar{T}_k \frac{\Delta S_k}{F}, \tag{5.16}$$

where F is the Faraday constant, 96485.3365 C/mol. By following the test procedure described in Chapter IV, the entropy change of the battery ΔS is measured as shown in Fig. 5.5.

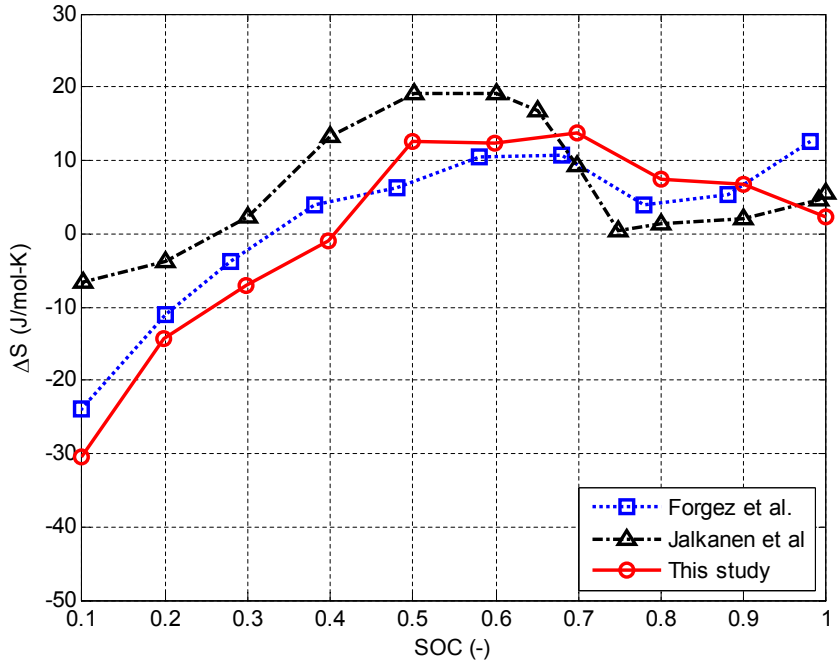

Figure 5.5: Measured entropy change of the battery and its comparison with literature values [65, 91]

5.3.2 Sequential State-Parameter Estimation

The schematic of battery state-parameter estimation is illustrated in Fig. 5.6. Since the heat generation rate is critical to estimate state and parameter of the battery thermal system, state and parameter of the electrical system are estimated prior to those of the thermal system. As seen from Eq. (5.16), the averaged temperature of the battery is required to calculate the entropic heat generation; however, the averaged temperature is not measurable but estimable. Thus, an estimated value at previous time step $\bar{T}_{k-1}$ is used instead. Due to slow dynamics of the thermal system, it is reasonable to assume that the difference between two consecutive averaged temperatures is negligible, i.e. $\bar{T}_k \approx \bar{T}_{k-1}$.

For state-parameter estimation of the electrical and thermal system, a variant of Kalman Filter is applied. States, parameters, inputs and outputs of the electrical and thermal systems are summarized in Table 5.3. The Dual Kalman Filter (DKF) based estimator developed in Chapter III is adopted for the thermal system whereas a Dual Extended Kalman Filter (DEKF) is applied to the electrical system.

Even though the efficacy of the DEKF-based estimator to determine states (SOC and polarization voltage) and parameters (resistances and capacitances) of the electrical dynamics has been shown in literature [25, 115], sensitivity of the states and

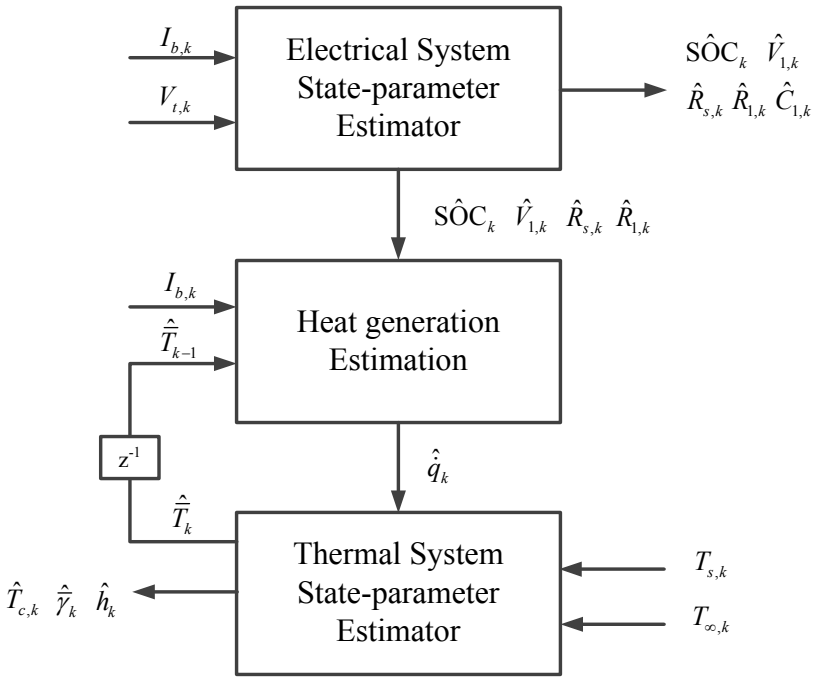

Figure 5.6: Schematic of state-parameter estimation for electrical and thermal systems

parameters to voltage prediction has not been fully considered for the estimation problem. Therefore, a grouping approach for state-parameter estimation is investigated based on sensitivity analysis.

Similarly to Chapter III, sensitivity of the states and parameters is analyzed by investigating the partial derivative of output with respect to the individual state and parameter through a simulation using a HEV current profile over a military driving mission, Urban Assault Cycle (UAC) [116]. The sensitivity of terminal voltage to each of the electrical state and parameter can be expressed using Eq. 5.12 as follows:

$$\frac{\partial V_{\mathrm{t},k}}{\partial \mathrm{SOC}} = \frac{\partial V_{\mathrm{oc}}(\mathrm{SOC}_k)}{\partial \mathrm{SOC}}, \tag{5.17a}$$

$$\frac{\partial V_{\mathrm{t},k}}{\partial V_1} = -1, \tag{5.17b}$$

$$\frac{\partial V_{\mathrm{t},k}}{\partial R_{\mathrm{s}}} = -I_{\mathrm{b},k}, \tag{5.17c}$$

$$\frac{\partial V_{\mathrm{t},k}}{\partial R_1} = -e^{\frac{\Delta t}{R_1 C_1}} \frac{\Delta t}{R_1^2 C_1} V_{1,k-1} - \left(1 - e^{\frac{\Delta t}{R_1 C_1}} - R_1 e^{\frac{\Delta t}{R_1 C_1}} \frac{\Delta t}{R_1^2 C_1}\right) I_{\mathrm{b},k-1}, \tag{5.17d}$$

$$\frac{\partial V_{\mathrm{t},k}}{\partial C_1} = -e^{\frac{\Delta t}{R_1 C_1}} \frac{\Delta t}{R_1 C_1^2} V_{1,k-1} + R_1 e^{\frac{\Delta t}{R_1 C_1}} \frac{\Delta t}{R_1 C_1^2} I_{\mathrm{b},k-1}. \tag{5.17e}$$

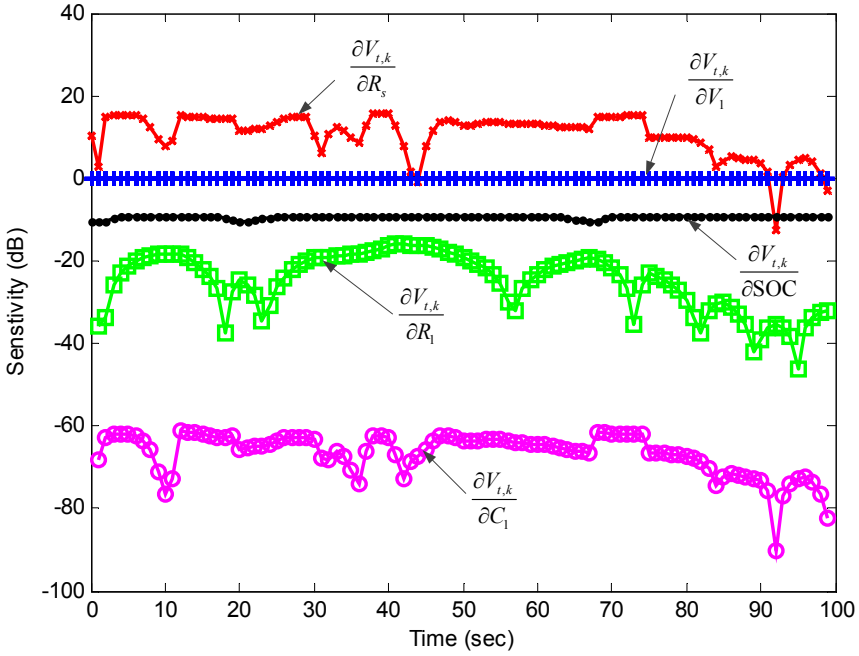

Figure 5.7: Sensitivity of output responses with respect to parameter variations; the variable R_s is the most sensitive parameter, followed by V_1, SOC, R_1 and C_1.

It is assumed that the states and parameters of the electrical system are known perfectly: (1) the initial battery SOC is known, (2) the battery SOC based on the integration of the current is accurate, and (3) parameters obtained from off-line identification process are accurate. As seen from Fig. 5.7, the internal resistance R_s is the most estimable followed by the polarization voltage V_1 and SOC. This result corresponds to Eq. (5.12b) where the thermal voltage V_t is computed from SOC (or $V_\mathrm{oc}(\mathrm{SOC})$), V_1 and $R_\mathrm{s}I_\mathrm{b}$. For the battery of interest to us, $\mathrm{LiFePO_4}$/graphite, V_oc–SOC curve is flat in the middle SOC range from 0.2 to 0.9 (Fig. 2.3); thus, SOC is relatively difficult to be identified.

Based on these results, the states and parameters are divided into two groups as follows:

$$\Omega_1 =: \{\mathrm{SOC}, V_1, R_\mathrm{s}\}, \tag{5.18a}$$

$$\Omega_2 =: \{R_1, C_1\} \tag{5.18b}$$

The internal resistance $R_{\mathrm{s},k}$ is augmented with SOC_k and $V_{1,k}$ as the parameters in Ω_1; on the other hand, the polarization resistance $R_{1,k}$ and capacitance $C_{1,k}$ are considered as the parameters in Ω_2. This grouping approach benefits from decoupling parameter interactions between two groups, allowing the ease of tuning the DEKF

[117]. It is noted that the parameters in Ω_1 can be considered as the states of the augmented system similarly to a Joint Extended Kalman Filter presented in Chapter III. Therefore, system matrices for the electrical dynamics need to be redefined as

$$\bar{A}_E = \begin{bmatrix} A_E & 0 \\ 0 & 1 \end{bmatrix}, \tag{5.19a}$$

$$\bar{B}_E = \begin{bmatrix} B_E \\ 0 \end{bmatrix}. \tag{5.19b}$$

In general, a nonlinear dynamics can be expressed as follows:

$$x_{k+1} = f(x_k, u_k, \theta_k) + w_k, \tag{5.20a}$$

$$y_k = g(x_k, u_k, \theta_k) + v_k, \tag{5.20b}$$

$$\theta_{k+1} = \theta_k + r_k, \tag{5.20c}$$

where x_k, u_k, θ_k and y_k are state (or parameter in Ω_1), input, parameter (or parameter in Ω_2) and output, respectively; w_k, v_k and r_k are independent, zero-mean, Gaussian noise processes of covariance matrices Σ_w, Σ_v and Σ_r, respectively. Then, the DEKF estimator is given as the following update processes.
Time update for the parameter (or parameter in Ω_2) filter:

$$\hat{\theta}_k^- = \hat{\theta}_{k-1}^+, \tag{5.21a}$$

$$P_{\theta,k}^- = P_{\theta,k-1}^+ + \Sigma_r. \tag{5.21b}$$

Time update for the state (or parameter in Ω_1) filter:

$$\hat{x}_k^- = f(\hat{x}_{k-1}^+, u_{k-1}, \hat{\theta}_k^-), \tag{5.22a}$$

$$P_{x,k}^- = \bar{A}_{k-1} P_{x,k-1}^+ \bar{A}_{k-1}^T + \Sigma_w. \tag{5.22b}$$

Measurement update for the state filter:

$$K_k = P_{x,k}^- C_k^{xT} \left[C_k^x P_{x,k}^- C_k^{xT} + \Sigma_v \right]^{-1}, \tag{5.23a}$$

$$\hat{x}_k^+ = \hat{x}_k^- + K_k \left[y_k - g(\hat{x}_k^-, u_k, \hat{\theta}_k^-) \right] \tag{5.23b}$$

$$P_{x,k}^+ = \left[I - K_k C_k^x \right] P_{x,k}^-. \tag{5.23c}$$

Table 5.3: State, parameter, input and output of electrical and thermal systems for state-parameter estimation

	Electrical	Thermal
Parameter in Ω_1/State	$\theta_{\Omega_1,k} = [\mathrm{SOC}_k\, V_{1,k}\, R_{s,k}\,]^T$	$x_{T,k} = [\bar{T}_k\, \bar{\gamma}_k]^T$
Parameter in Ω_2/Parameter	$\theta_{\Omega_2,k} = [R_{1,k}\, C_{1,k}]^T$	$\theta_{T,k} = h_k$
Input	$u_{E,k} = I_{\mathrm{b},k}$	$u_{T,k} = [\dot{q}_k\, T_{\infty,k}]^T$
Output	$y_{E,k} = V_{\mathrm{t},k}$	$y_{T,k} = [T_{\mathrm{s},k}]^T$

Measurement update for the parameter filter:

$$L_k = P^-_{\theta,k} C^{\theta^T}_k \left[C^\theta_k P^-_{\theta,k} C^{\theta^T}_k + \Sigma_v \right]^{-1}, \tag{5.24a}$$

$$\hat{\theta}^+_k = \hat{\theta}^-_k + L_k \left[y_k - g(\hat{x}^-_k, u_k, \hat{\theta}^-_k) \right] \tag{5.24b}$$

$$P^+_{\theta,k} = \left[I - L_k C^\theta_k \right] P^-_{\theta,k}, \tag{5.24c}$$

where superscripts $-$ and $+$ denote the *a priori* and *a posteriori* values respectively. The matrices $\bar{A}_{k-1}$, C^x_k and C^θ_k are calculated according to

$$\bar{A}_{k-1} = \frac{\partial f(x_{k-1}, u_{k-1}, \hat{\theta}^-_k)}{\partial x_{k-1}}\Big|_{x_{k-1}=\hat{x}^+_{k-1}}, \tag{5.25a}$$

$$C^x_k = \frac{\partial g(x_k, u_k, \hat{\theta}^-_k)}{\partial x_k}\Big|_{x_k=\hat{x}^-_k}, \tag{5.25b}$$

$$C^\theta_k = \frac{dg(\hat{x}^-_k, u_{k-1}, \theta_k)}{d\theta_k}\Big|_{\theta_k=\hat{\theta}^-_k}. \tag{5.25c}$$

Table 5.3 summarizes parameters in Ω_1 and Ω_2 (or states and parameters) alongside inputs and outputs of the electrical and thermal systems for the state-parameter estimation.

5.3.3 Power Capability Estimation

To calculate power capability of the battery, the Algebraic Propagation (AP) method developed in Chapter IV is applied with estimated states and parameters from the sate-parameter estimators as illustrated in Fig. 5.8. The AP method computes a constant input which leads to that none of constraints are violated in N future steps. Similar to state-parameter estimation, power capability is also sequentially computed.

To apply the AP method to the electrical system, the output of the system (5.12b)

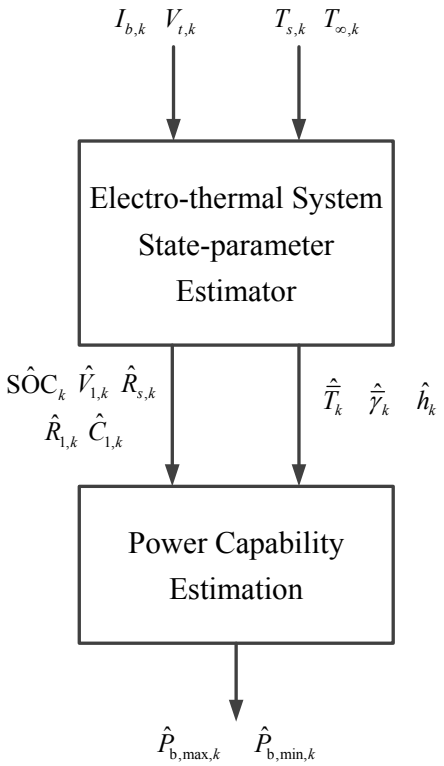

Figure 5.8: Schematic of power capability estimation

needs to be linearized as described in Chapter IV and is expressed by:

$$\begin{bmatrix} \hat{\mathrm{SOC}}_{k+1} \\ \hat{V}_{1,k+1} \end{bmatrix} = A_E(\hat{R}_{1,k}, \hat{C}_{1,k}) \begin{bmatrix} \hat{\mathrm{SOC}}_k \\ \hat{V}_{1,k} \end{bmatrix} - B_E(\hat{R}_{1,k}, \hat{C}_{1,k}) I_{\mathrm{b},k} \tag{5.26a}$$

$$\begin{bmatrix} \hat{\mathrm{SOC}}_k \\ \hat{V}_{\mathrm{t},k} \end{bmatrix} = C_E \begin{bmatrix} \hat{\mathrm{SOC}}_k \\ \hat{V}_{1,k} \end{bmatrix} - D_E I_{\mathrm{b},k} + F_E \tag{5.26b}$$

where matrices C_E, D_E and F_E are obtained by

$$C_E \triangleq \begin{bmatrix} C_{E1} \\ C_{E2} \end{bmatrix} = \begin{bmatrix} 1 & 0 \\ \dfrac{\partial V_{\mathrm{oc}}(\mathrm{SOC})}{\partial \mathrm{SOC}}\Big|_{\mathrm{SOC}=\hat{\mathrm{SOC}}_k} & -1 \end{bmatrix} \tag{5.27a}$$

$$D_E \triangleq \begin{bmatrix} D_{E1} \\ D_{E2} \end{bmatrix} = \begin{bmatrix} 0 \\ \hat{R}_{s,k} \end{bmatrix} \tag{5.27b}$$

$$F_E \triangleq \begin{bmatrix} F_{E1} \\ F_{E2} \end{bmatrix} = \begin{bmatrix} 0 \\ V_{\mathrm{t},k} - \dfrac{\partial V_{\mathrm{oc}}(\mathrm{SOC})}{\partial \mathrm{SOC}}\Big|_{\mathrm{SOC}=\hat{\mathrm{SOC}}_k} \hat{\mathrm{SOC}}_k \end{bmatrix} \tag{5.27c}$$

The maximum permissible currents accounting for electrical constraints such as

SOC and voltage limits, $\mathrm{SOC}_{\min}$, $\mathrm{SOC}_{\max}$, $V_{\min}$, and $V_{\max}$, are determined respectively as following:

$$\hat{I}^{E,\mathrm{SOC}_{\min}}_{\mathrm{b,max},k} = \left(\sum_{i=0}^{N-1} C_{E1}A_E^i B_E + D_{E1}\right)^{-1} \left(\mathrm{SOC}_{\min} - C_{E1}A_E^N \begin{bmatrix} \hat{\mathrm{SOC}}_k \\ \hat{V}_{1,k} \end{bmatrix} - F_{E1}\right) \tag{5.28a}$$

$$\hat{I}^{E,\mathrm{SOC}_{\max}}_{\mathrm{b,min},k} = \left(\sum_{i=0}^{N-1} C_{E1}A_E^i B_E + D_{E1}\right)^{-1} \left(\mathrm{SOC}_{\max} - C_{E1}A_E^N \begin{bmatrix} \hat{\mathrm{SOC}}_k \\ \hat{V}_{1,k} \end{bmatrix} - F_{E1}\right) \tag{5.28b}$$

$$\hat{I}^{E,V_{\min}}_{\mathrm{b,max},k} = \left(\sum_{i=0}^{N-1} C_{E2}A_E^i B_E + D_{E2}\right)^{-1} \left(V_{\min} - C_{E2}A_E^N \begin{bmatrix} \hat{\mathrm{SOC}}_k \\ \hat{V}_{1,k} \end{bmatrix} - F_{E2}\right) \tag{5.28c}$$

$$\hat{I}^{E,V_{\max}}_{\mathrm{b,min},k} = \left(\sum_{i=0}^{N-1} C_{E2}A_E^i B_E + D_{E2}\right)^{-1} \left(V_{\max} - C_{E2}A_E^N \begin{bmatrix} \hat{\mathrm{SOC}}_k \\ \hat{V}_{1,k} \end{bmatrix} - F_{E2}\right) \tag{5.28d}$$

For the battery thermal system, the representation in Eq. (5.14) is modified for time scale separation as the following equations:

$$\begin{bmatrix} \hat{\bar{T}}_{k+1} \\ \hat{\gamma}_{k+1} \end{bmatrix} = A_T(\hat{h}_k) \begin{bmatrix} \hat{\bar{T}}_k \\ \hat{\gamma}_k \end{bmatrix} + B_{T1}(\hat{h}_k)\mu_k + \xi_{1,k}, \tag{5.29a}$$

$$\hat{T}_{\mathrm{c},k} = C_{T1}(\hat{h}_k) \begin{bmatrix} \hat{\bar{T}}_k \\ \hat{\gamma}_k \end{bmatrix} + \xi_{2,k}, \tag{5.29b}$$

where

$$\mu_k = I^2_{\mathrm{b},k}\hat{R}_{s,k} - I_{\mathrm{b},k}\hat{\bar{T}}_k \frac{\Delta\hat{S}_k}{F}, \tag{5.30a}$$

$$\xi_{1,k} = B_{T1}(\hat{h}_k) \begin{bmatrix} \dfrac{\hat{V}^2_{1,k}}{\hat{R}_{1,k}} \\ T_{\infty,k} \end{bmatrix} \tag{5.30b}$$

$$\xi_{2,k} = D_{T1}(h_k)T_{\infty,k}. \tag{5.30c}$$

When the prediction period is short, the SOC and temperature of the battery do not change significantly over the prediction horizon; time scale separation can be utilized as presented in Chapter IV. Thus, it is reasonable to assume that the entropy change and internal resistance are constant over the prediction horizon, that is, $R_{s,j|k} \approx R_{s,k}$ and $\Delta S_{j|k} \approx \Delta S_k$ for $j = k, k+1, \ldots, k+N$. This approximation

is conservative since internal resistance decreases with respect to increasing temperatures. In addition, ambient temperature and convection coefficient are assumed not to change rapidly and hence to be constant, i.e. $T_{\infty,j|k} \approx T_{\infty,k}$ and $h_{j|k} \approx h_k$ for $j = k, k+1, \ldots, k+N$. Lastly, a conservative value of heat generation by polarization voltage over the prediction horizon is obtained through model iteration using the maximum permissible current at previous sampling time $k - N\Delta t$.

$$\bar{\xi}_{1,k} = \max\{\xi_{1,k}, \xi_{1,k+N}\}. \tag{5.31}$$

These approximations make it easy to handle the nonlinearity in the expression of heat generation rate using a quadratic term $I_{\mathrm{b},k}^2$ and a bilinear term $I_{\mathrm{b},k}\bar{T}_k$.

Then, the maximum of the input $\mu_{\max,k}^q$, $q \in \{\mathrm{dch}, \mathrm{chg}\}$, which is described by considering the maximum core temperature $T_{c,\max}$, is determined as

$$\mu_{\max,k}^{\mathrm{dch}} = \left(\sum_{i=0}^{N-1} C_T A_T^i B_T\right)^{-1}\left(T_{\mathrm{c,max}} - C_T A_T^N \begin{bmatrix}\hat{\bar{T}}_k \\ \hat{\gamma}_k\end{bmatrix} - \sum_{i=0}^{N-1} C_T A_T^i \bar{\xi}_{1,k}^{\mathrm{dch}} - \xi_{2,k}\right), \tag{5.32a}$$

$$\mu_{\max,k}^{\mathrm{chg}} = \left(\sum_{i=0}^{N-1} C_T A_T^i B_T\right)^{-1}\left(T_{\mathrm{c,max}} - C_T A_T^N \begin{bmatrix}\hat{\bar{T}}_k \\ \hat{\gamma}_k\end{bmatrix} - \sum_{i=0}^{N-1} C_T A_T^i \bar{\xi}_{1,k}^{\mathrm{chg}} - \xi_{2,k}\right), \tag{5.32b}$$

where superscripts *dch* and *chg* represent battery discharge and charge, respectively. By substituting Eqs. (5.32) into Eq. (5.30a), the maximum permissible currents during battery discharge and charge are determined respectively by the following equations

$$\hat{I}_{\mathrm{b,max},k}^{T,\mathrm{dch}} = \frac{\frac{\hat{\bar{T}}_k \Delta\hat{S}_k}{F} + \sqrt{\left(\frac{\hat{\bar{T}}_k \Delta\hat{S}_k}{F}\right)^2 + 4\hat{R}_{s,k}\mu_{\max,k}^{\mathrm{dch}}}}{2\hat{R}_{s,k}}, \tag{5.33a}$$

$$\hat{I}_{\mathrm{b,min},k}^{T,\mathrm{chg}} = \frac{\frac{\hat{\bar{T}}_k \Delta\hat{S}_k}{F} - \sqrt{\left(\frac{\hat{\bar{T}}_k \Delta\hat{S}_k}{F}\right)^2 + 4\hat{R}_{s,k}\mu_{\max,k}^{\mathrm{chg}}}}{2\hat{R}_{s,k}}. \tag{5.33b}$$

Maximum discharge and charge currents accounting for all constraints are calculated with

$$\hat{I}_{\mathrm{b,max},k}^{\mathrm{dch}} = \min\{\hat{I}_{\mathrm{b,max},k}^{E,\mathrm{SOC_{min}}}, \hat{I}_{\mathrm{b,max},k}^{E,V_{\min}}, \hat{I}_{\mathrm{b,max},k}^{T,\mathrm{dch}}\} \tag{5.34a}$$

$$\hat{I}_{\mathrm{b,min},k}^{\mathrm{chg}} = \max\{\hat{I}_{\mathrm{b,min},k}^{E,\mathrm{SOC_{max}}}, \hat{I}_{\mathrm{b,min},k}^{E,V_{\max}}, \hat{I}_{\mathrm{b,min},k}^{T,\mathrm{chg}}\} \tag{5.34b}$$

Finally, the power capability $\{\hat{P}_{\mathrm{b,max},k}, \hat{P}_{\mathrm{b,min},k}\}$ is estimated by the product of the maximum allowable current and terminal voltage after N future sample steps expressed as

$$\hat{P}_{\mathrm{b,max},k} = \hat{I}^{\mathrm{dch}}_{\mathrm{b,max},k} \cdot \hat{V}^{\mathrm{dch}}_{k+N|k}, \tag{5.35a}$$

$$\hat{P}_{\mathrm{b,min},k} = \hat{I}^{\mathrm{chg}}_{\mathrm{b,min},k} \cdot \hat{V}^{\mathrm{chg}}_{k+N|k}, \tag{5.35b}$$

where the predicted terminal voltage $V^{q}_{k+N|k}$, $q \in \{\mathrm{dch}, \mathrm{chg}\}$ is calculated with

$$\begin{aligned}\hat{V}^{\mathrm{dch}}_{k+N|k} = V_{\mathrm{oc}}\left(\hat{\mathrm{SOC}}_k - \frac{\hat{I}^{\mathrm{dch}}_{\mathrm{b,max},k} N\Delta t}{3600 C_{\mathrm{b}}}\right) - \hat{I}^{\mathrm{dch}}_{\mathrm{b,max},k}\hat{R}_{s,k} \\ - e^{\frac{-N\Delta t}{\hat{R}_{1,k}\hat{C}_{1,k}}}\hat{V}_{1,k} - \hat{I}^{\mathrm{dch}}_{\mathrm{b,max},k}\hat{R}_{1,k}\left(1 - e^{\frac{-N\Delta t}{\hat{R}_{1,k}\hat{C}_{1,k}}}\right),\end{aligned} \tag{5.36a}$$

$$\begin{aligned}\hat{V}^{\mathrm{chg}}_{k+N|k} = V_{\mathrm{oc}}\left(\hat{\mathrm{SOC}}_k - \frac{\hat{I}^{\mathrm{chg}}_{\mathrm{b,min},k} N\Delta t}{3600 C_{\mathrm{b}}}\right) - \hat{I}^{\mathrm{chg}}_{\mathrm{b,min},k}\hat{R}_{s,k} \\ - e^{\frac{-N\Delta t}{\hat{R}_{1,k}\hat{C}_{1,k}}}\hat{V}_{1,k} - \hat{I}^{\mathrm{chg}}_{\mathrm{b,min},k}\hat{R}_{1,k}\left(1 - e^{\frac{-N\Delta t}{\hat{R}_{1,k}\hat{C}_{1,k}}}\right).\end{aligned} \tag{5.36b}$$

As described in Section 5.2, the maximum power capability is provided to the power management system.

5.4 Model-in-the-loop Simulation Results

The purpose of this section is to investigate the performance of the BMS and its influences on the PMS. The military SHEV is simulated in the co-simulation framework in which the battery electro-thermal model and the on-line adaptive estimators are fully integrated to the vehicle model. The military vehicle mission profile, Urban Assault Cycle (UAC) shown in Fig. 5.9, is used as an input to the SHEV simulator. The UAC cycle has frequent high acceleration and deceleration events, typical of military driving conditions [40].

The battery current and terminal voltage, which are inputs to the DEKF-based estimator for the electrical system, are shown in Fig. 5.10. To simulate realistic noise conditions, measured current and voltage are contaminated with artificial Gaussian noises, i.e. σ_I=0.003 and σ_V=0.001; the tuning parameters of the DEKF are specified as shown in Table 5.4.

The results of state-parameter estimation for the electrical system are shown in Fig. 5.11(a)–(c), showing that the DEKF can simultaneously estimate SOC, polariza-

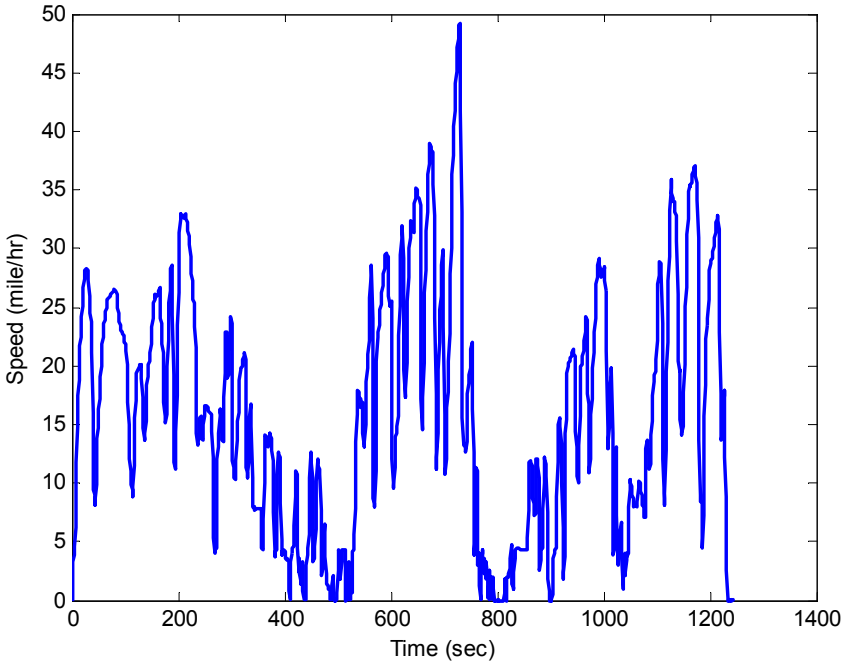

Figure 5.9: A military vehicle mission profile: Urban Assault Cycle

Table 5.4: Tuning parameters of adaptive estimators for electrical and thermal systems

Parameter	Electrical system	Thermal system
Σ_w	diag(6e-3,2e-2,8e-6)	diag(2.5e-7,2.5e-7)
Σ_v	1	2.5e-4
Σ_r	diag(2.5e8,4e-1)	9e-4
$P(0)$	diag(1,1,1)	diag(1,1)
$S(0)$	diag(1e-1,1e-1)	1e-2

tion voltage and internal resistance. The *true*[2] battery SOC, denoted by SOC_{CC}, is measured by using Coulomb Counting (CC). Slow convergence of the battery SOC is the result of estimator tuning based on sensitivity analysis discussed in Section 5.3.2. On the other hand, the polarization voltage and internal resistance are estimated with relatively fast convergence rate. It is noted that the battery plant is modeled by using an OCV-R-RC-RC equivalent-circuit model; therefore, the *true* polarization voltage is the sum of two polarization voltages in the plant model. It is also noted that polarization resistance and capacitance are not shown since the order of the

[2]The term *true* stands for a response from the plant model in the SHEV simulator.

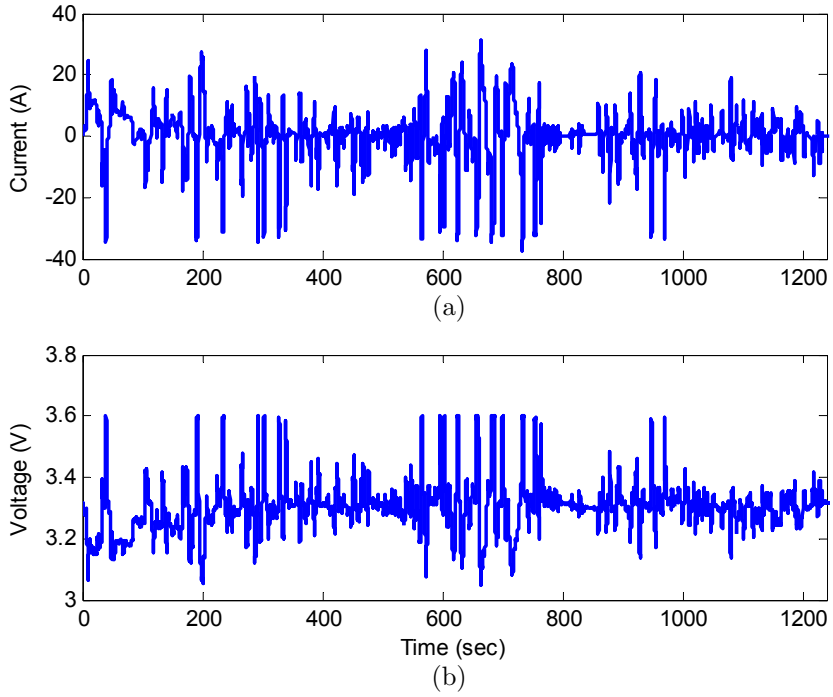

Figure 5.10: Input data to the DEKF over the UAC: (a) current, (b) terminal Voltage

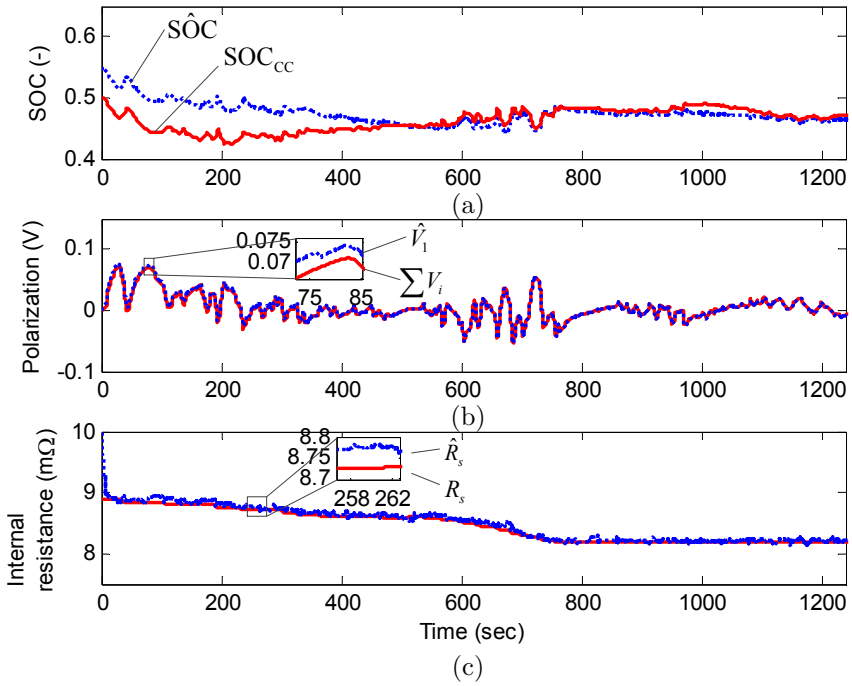

Figure 5.11: Performance of the DEKF-based estimator for the electrical system: (a) SOC, (b) Polarization voltage, (c) internal resistance

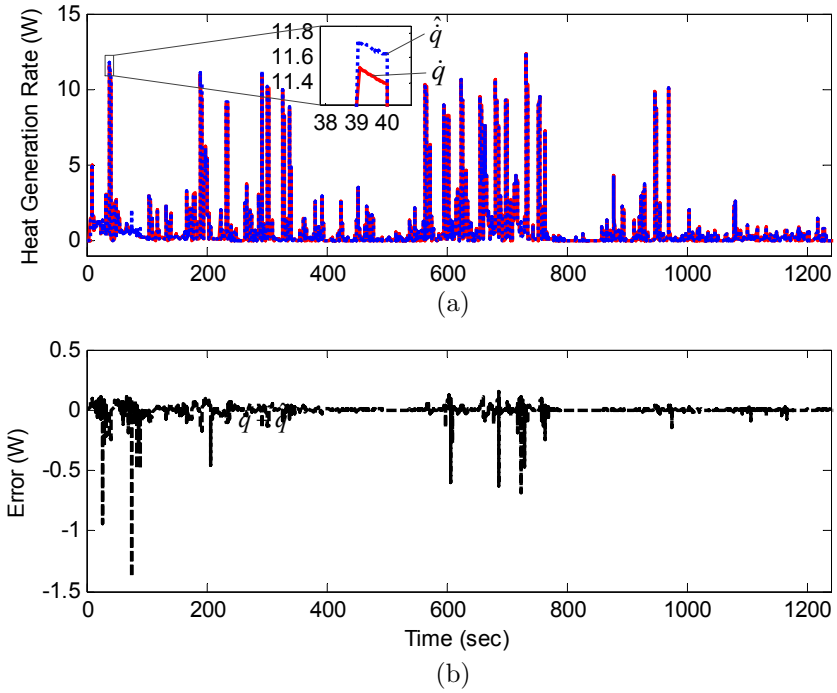

Figure 5.12: Performance of the DEKF-based estimator for the electrical system: (a) heat generation rate, (b) error

battery model in the estimation algorithm is different from that of the plant model. Instead, the effectiveness of the parameter estimation is evaluated by investigating the accuracy of the polarization voltage and heat generation rate. Figure 5.12 shows the comparison between the *true* heat generation rate and the estimated value; the root-mean-square-error (RMSE) of the heat generation rate is 0.001 W which is less than 0.2 percent of the averaged heat generation rate over the UAC. The heat generation rate needs to be accurately estimated since the estimated value is used as an input to the state-parameter estimation in the thermal system.

Figure 5.13 shows the battery surface temperature and ambient temperature which are used as inputs to the DKF-based estimator for the thermal system. Similar to the DEKF, Gaussian noises are artificially added to the measured data, i.e. σ_{T_s}=σ_{T_∞}=0.016. Details of tuning parameters of the DKF are also shown in Table 5.4. To simulate malfunction of the cooling system, the convection coefficient is deliberately changed from 20 to 3 W/m^2/K at t=300 s. This malfunction condition is simulated to assess not only the performance of the DKF but also the effectiveness of the power capability estimation. As seen from Fig. 5.14, the DKF is capable of providing accurate estimates of the states and parameter of the thermal system. It is noted that, as presented in Section 5.3.2, a one step-delayed averaged temperature

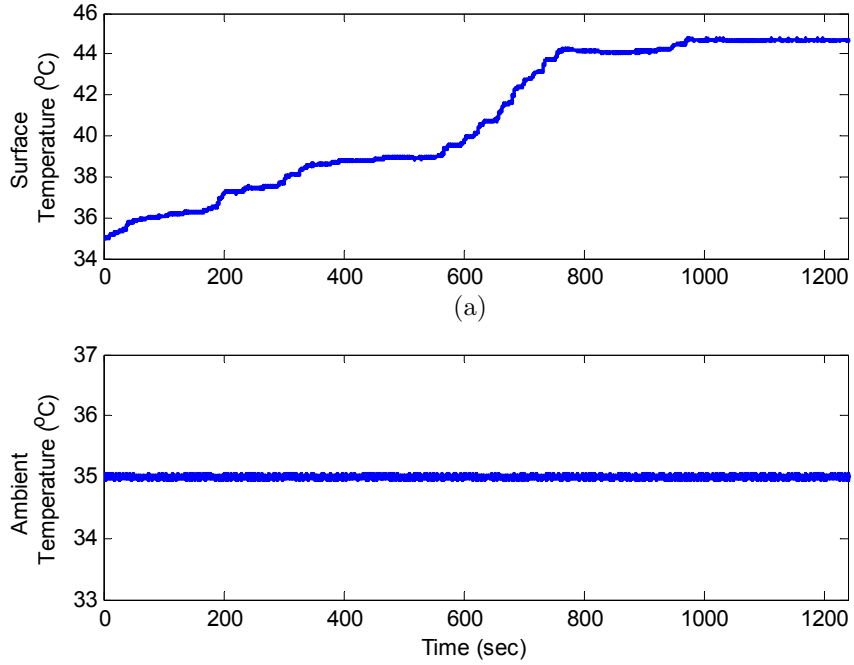

(a)

(b)

Figure 5.13: Input data to the DKF over the UAC: (a) surface temperature; (b) ambient temperature

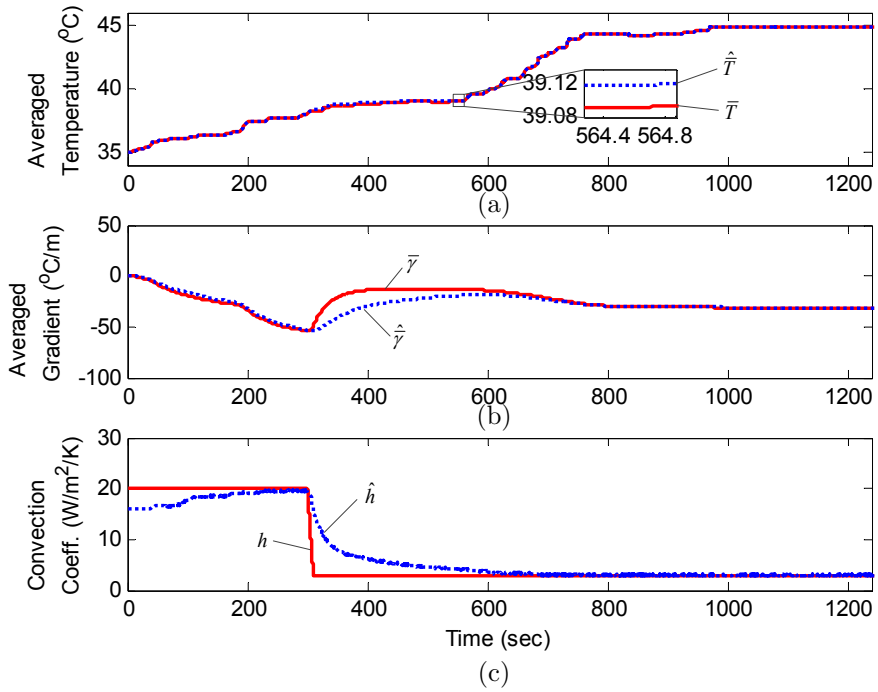

(a)

(b)

(c)

Figure 5.14: Performance of the DKF-based estimator for the thermal system: (a) averaged temperature, (b) averaged thermal gradient, (c) convection coefficient

is used to estimate the heat generation rate.

The results of power capability estimation are shown in Fig. 5.15(a)–(e), which depict battery power, terminal voltage and core temperature. As shown in Fig. 5.15(a), the maximum battery power is limited by electrical-constrained power capability when the battery core temperature is lower than the target value of $T_{\mathrm{c,max}} = 45°\mathrm{C}$. It can be seen that battery SOC and terminal voltage do not violate constraints (Fig. 5.15(c) and (d)). However, as the core temperature increases, thermal-constrained power capability becomes active and hence the battery power are effectively regulated between the maximum and minimum power limits. To highlight this performance, specific time periods from 930 to 110 seconds are shown in Fig. 5.15(b). Consequently, the core temperature does not exceed the maximum temperature as illustrated in Fig. 5.15(e).

Evidenced by the results from the model-in-the-loop simulation, it can be concluded that the developed estimation algorithms including states, parameters, and power capability are capable of providing accurate information about the battery. Thus, the safe and reliable operation of the power management system as well as the battery can be achieved.

5.5 Conclusion

This chapter has demonstrated the application of state-parameter estimation algorithms developed in Chapters III and IV to a series hybrid electric vehicle. First, a model predictive control (MPC) based power management strategy is developed to determine power flows among hybrid powertrain components. Since the power management system requires operational limits of the battery, adaptive estimators capable of identifying the thermal and electrical states and parameters in an on-line manner are developed. For the electrical system, a parameter grouping approach is used based on parameter sensitivity analysis suggesting that battery SOC, polarization voltage, and internal resistance can be considered as one group. Moreover, the order of sequential estimation (electrical–thermal) is proposed and reasoned for better state-parameter estimation. Then, the algorithm to compute power capability of the battery is developed based on the simple method proposed in Chapter IV using the information provided by the adaptive estimators. The results of the model-in-the-loop simulation show that the proposed estimation algorithms can provide accurate information of the battery to the power management system and hence the safe and robust operation of the series hybrid electric vehicle can be achieved.

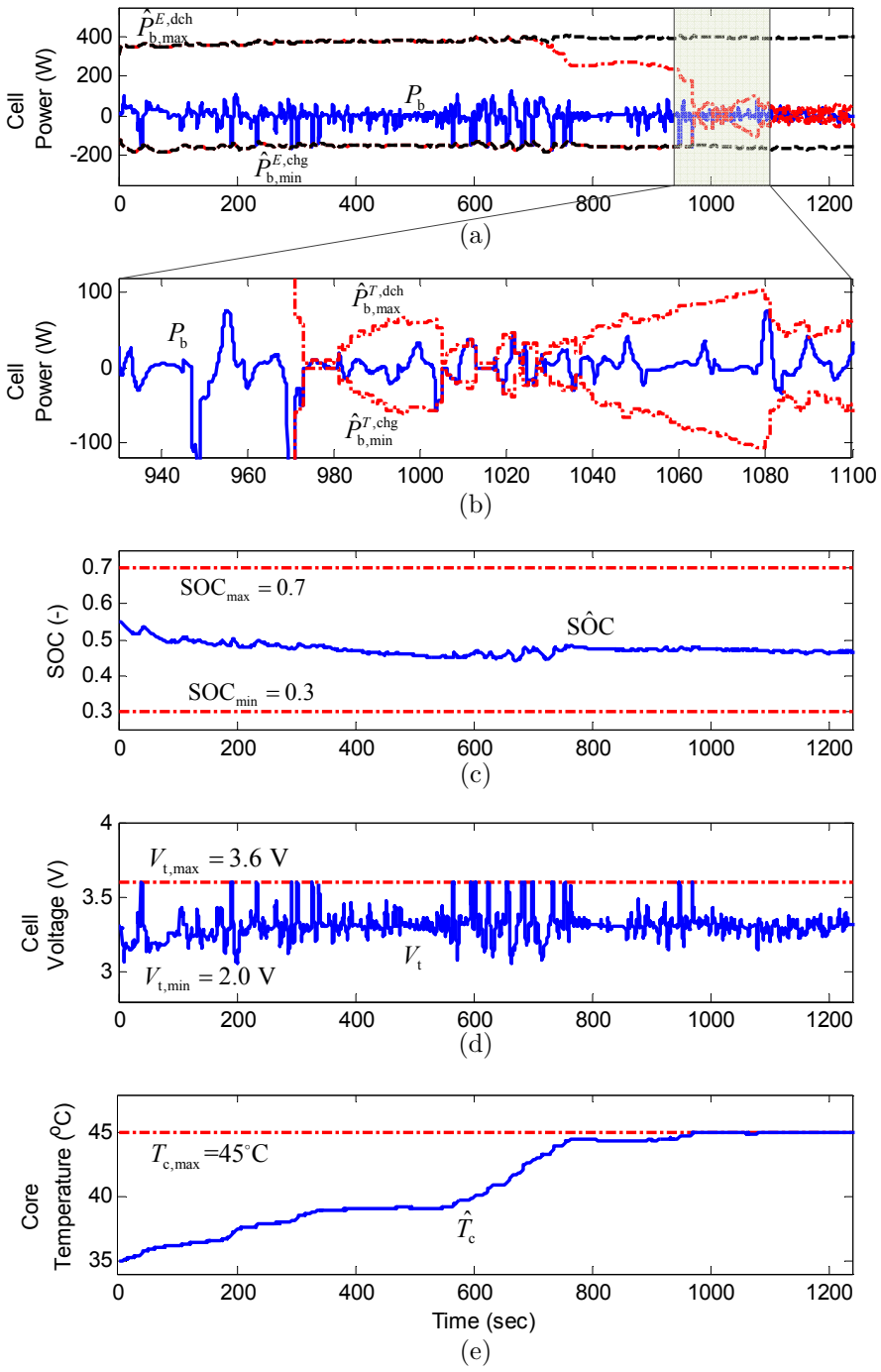

Figure 5.15: Performance of the power capability estimation: (a) power, (b) power (from 930 to 1100 seconds), (c) SOC, (d) terminal voltage, (e) core temperature

CHAPTER VI

Conclusion

6.1 Summary of Contributions

The contributions in this dissertation are summarized as follows.

In Chapter II, a radially distributed 1-D thermal modeling approach for a cylindrical battery is proposed. Polynomial approximation is applied to obtain a reduced-order model. Frequency domain analysis shows that the proposed model provides sufficiently accurate prediction of the core and the surface temperatures. The proposed model is used to identify thermal properties and convective coefficient for a 2.3 Ah 26650 LFP battery. The proposed thermal model is found to accurately predict the core and surface temperatures alongside volume-averaged temperature and volume-averaged temperature gradient of a cylindrical Li-ion battery.

In Chapter III, a method to estimate the temperature distribution in cylindrical batteries under unknown cooling conditions is proposed. First, a reduced-order thermal model developed in Chapter II is used to estimate the radial temperature distribution. Numerical analysis on parameter sensitivity supports the use of constant parameters for thermal conductivity and heat capacity and the importance of identifying the convection coefficient on-line. Filtering methods are applied to estimate the temperature inside the battery and convection coefficient. The proposed method establishes an on-line estimate of convection coefficient for accurate estimating the core temperature.

In Chapter IV, a method to estimate battery power limits accounting for both electrical and thermal constraints is presented. The method relies on an electro-thermal model for the electrical and thermal dynamic behaviors. Further, a method to parameterize the lumped thermal model that includes entopic heat generation as well as joule heating is presented and discussed. Under the assumptions of short

prediction horizons, a computationally efficient algorithm is proposed to estimate power capability of Li-ion batteries by utilizing time scale separation.

In Chapter V, the proposed battery thermal model and estimation algorithms from the previous chapters are integrated into a power management system for a series hybrid electric vehicle. An algorithm for sequential estimation of coupled model parameters and states is developed. For the electrical system, parameter grouping based on sensitivity is utilized to formulate the state-parameter estimation problem. The estimated states and parameters of the battery are used to predict the maximum allowable power of the battery which is required by the power management system. The results of the model-in-the-loop simulation reveal that the power management system can effectively determine power flow among hybrid powertrain components without violating operational constraints with information of the battery such as SOC, internal resistance, and power capability.

6.2 Possible Future Extensions

This dissertation proposes a novel approach to estimate power capability (or battery state-of-power) accounting for thermal and electrical constraints. The proposed approach is found to be effective to provide accurate information about battery core temperature, cooling condition, state-of-charge and internal resistance as well. Nevertheless, to advance the presented work, the following can be considered as opportunities for future research.

6.2.1 Battery warm-up strategy for cold start

Li-ion batteries are well known to suffer from poor performance at low temperatures: the discharge capacity and available power of the Li-ion batteries are substantially deteriorated below -20°C [118–121]. The poor performance at low temperatures is attributed to reduced conductivity and diffusivity of electrode and electrolyte [120, 122] and increased charge-transfer resistance at the solid-electrolyte-interface (SEI) [119]. For a given design of Li-ion batteries, heating with current drawn from the battery can be a viable solution to exploit the thermal dynamics of the battery by generating heat inside a battery cell [123]. Despite its feasibility, an optimal control to the battery warm-up problem has to be detailed to properly account for objectives (e.g. warm-up duration, efficiency, and battery state-of-health) and constraints (temperature, terminal voltage, and current). Pontryagin's Minimum Principle (PMP) and Dynamic Programming(DP) can be applied to solve this optimal

warm-up problem. Moreover, the state-parameter estimators presented in Chapters III and V can be augmented to the controller to provide accurate information about the battery.

6.2.2 Mechanical Stress as a Power Capability Constraint

The health of Li-ion batteries is typically judged by monitoring internal resistance and capacity [66, 124–130]. The performance degradation of a battery may not be the result of a single mechanism but of several complicated mechanisms as studied in literature [124,131,132]. In particular, Lithium de/intercalation into electrodes results in its expanding/contracting and eventually particles cracking or becoming electrically disconnected from the current collector leading to power capability loss [133–135]. Since the mechanical stress at the electrode level is not easy to measure, Cannarella and Arnold in [136] studied a stack level mechanical stress and its influence on capacity fade. This volumetric change or bulk mechanical stress is measurable by using load sensors and hence a monitoring system may be implementable on HEVs to provide additional information about the state-of-health and state-of-power of the battery. Thus, development of such a model to capture the relationship among bulk mechanical stress, battery state-of-charge (SOC) and temperature can be used to improve the estimation of power capability of Li-ion batteries presented in Chapter IV.

6.2.3 Powertrain-in-the-loop Validation

Experimental validation is required to investigate interaction among hybrid powertrain components under power and battery management strategies addressed in Chapter V. A networked hardware-in-the-loop simulation of this vehicle system can be considered to enable a system integration despite the fact that the components reside in different geographic locations [8, 137–140]. For example, the engine and battery are the hardware components located in two different locations, and the remaining components of the vehicle system (i.e., generator, motors, vehicle dynamics, and driver) are mathematically modeled and simulated in a third location. The overview of the networked system architecture is illustrated in Fig. 6.1.

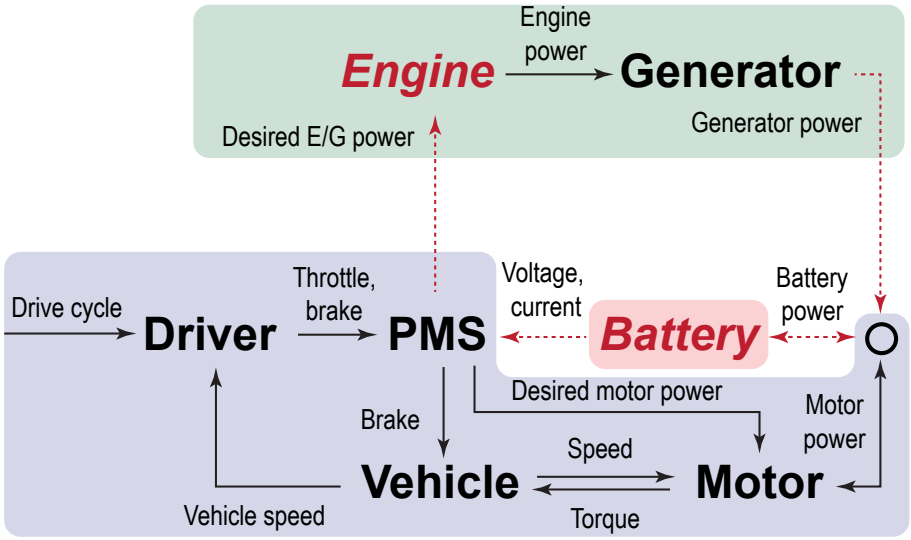

Figure 6.1: The overview of the networked hardware-in-the-loop simulation setup. Each shaded area represents a different geographic location. Italic typeface denotes actual hardware components. Dashed lines represent the signals communicated over the network.

APPENDICES

APPENDIX A

Development of a Power Rate Constraint Map for a Diesel-powered Series Hybrid Electric Vehicle

A.1 Introduction

In this appendix, a methodology to design the maximum allowable power rate map, the *power rate constraint map*, for an engine-generator of an SHEV is proposed for reducing soot emissions. To develop this constraint map, a three-step discrete optimization process is used by sequentially combining Genetic Algorithm (GA) and Exhaustive Search (ES). GA results are used to narrow down the design space. Then, ES finds the optimal solution within the search region reduced by GA. A quasi-static map for soot emissions similar to [11] and [52] is considered as a first step to evaluate the benefits of including the power rate constraint map in an Model Predictive Control (MPC) based power management for soot emissions reduction. This constraint map is then evaluated experimentally using an engine-in-the-loop simulation setup where a Navistar 6.4L V8 diesel engine is supplemented by a 9.27 kWh battery. Moreover, the implementation of the resulting MPC on battery life is assessed using a weighted Ah-processed model [141].

This appendix is organized as follows. Section A investigates the effect of the engine-generator power rate on fuel economy and soot emissions. Then, the three-step discrete optimization process to obtain the power rate constraint map is described in Section A. Experimental setup and results are presented and discussed in Section A, and conclusions are drawn in Section A.

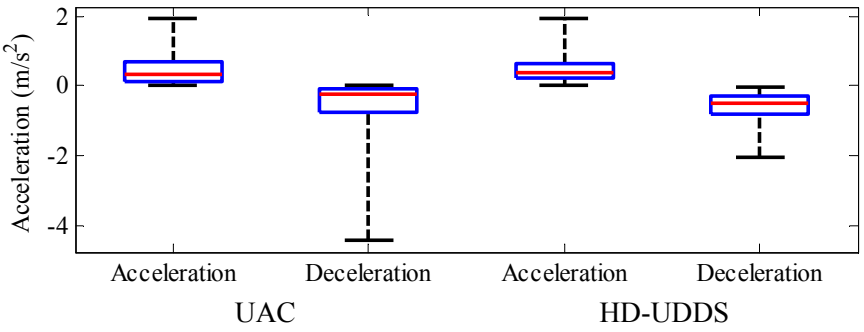

Figure A.1: Comparison of acceleration and deceleration of the urban assault cycle (UAC) and the heavy-duty urban dynamometer driving schedule (HD-UDDS)

A.2 Effect of maximum engine-generator power rate

The purpose of this section is to investigate the effect of the engine-generator power rate on the fuel economy and soot emissions. A military vehicle driving mission, Urban Assault Cycle (UAC), is used; this cycle with a whole distance of 8.80 km (5.46 mile) is aggressive compared to a federal driving cycle such as the Urban Dynamometer Driving Schedule for Heavy-Duty Vehicles (HD-UDDS) as shown in Fig. A.1. The UAC cycle has frequent high acceleration and deceleration events, typical of military driving conditions [40].

For the purpose of accounting for the remaining battery SOC, two consecutive driving cycles are considered, and the fuel economy is calculated by

$$\text{fuel economy} = \frac{1}{N_\text{s}} \sum_{k=1}^{N_\text{s}} \frac{\int_{t_k}^{t_k+t_\text{cycle}} v_\text{veh}\, dt}{\int_{t_k}^{t_k+t_\text{cycle}} \dot{m}_f\, dt}, \tag{A.1}$$

where t_cycle is the total time of the given driving cycle, v_veh is the velocity of the vehicle and N_s is the total number of t_k's that satisfy the SOC sustainability condition: $t_k \in \{\xi : \text{SOC}\,(\xi) = \text{SOC}\,(\xi + t_\text{cycle})\}$ and $\xi \in \mathbb{R}^1$. Parameters for the MPC problem are tuned manually for the best fuel economy and summarized in Table A.1 along with the constraint values.

To predict the trends in soot emissions and subsequently help with the control design, a quasi-static map is considered. Note that more than 50% of all soot emissions could be generated during transients such as tip-in operations [142] and hence a quasi-static map cannot accurately predict the magnitude of the soot emissions during aggressive transients. Nevertheless, for the purposes of designing a supervisory

Table A.1: Parameter and Constraint Values for MPC

MPC Parameter	Value	Constraint	Value
w_1	4.17	$V_{\min}$	2.0 V
w_2	1	$V_{\max}$	3.6 V
w_3	2.5e-5	$P_{\mathrm{g,min}}$	0 kW
w_4	1.25e-6	$P_{\mathrm{g,max}}$	236 kW
N_{c}	15	$\Delta P_{\mathrm{g,min}}$	-60 kW/s
N_{p}	40	$\Delta P_{\mathrm{g,max}}$	30 kW/s
$y_{1,\mathrm{ref}}$	0.5	$\mathrm{SOC}_{\min}$	0.3
$y_{2,\mathrm{ref}}$	0	$\mathrm{SOC}_{\max}$	0.7

controller, quasi-static maps have been shown to be useful due to their ability to capture the basic trends [11,52]. More relevantly, the quasi-static soot emissions map used in this work has been previously found adequate to capture the basic trends in soot emissions even during transients [143]. Therefore, it is used in this study to help with the control design and avoid ad-hoc experimental tuning, with the understanding that the resulting control design may not yield the optimal performance and a dynamic soot emissions model such as [143] would ultimately be needed to achieve the best performance. Fuel economy and total soot emission over the UAC are 3.278 km/l (7.71 mpg) and 0.0316 g/km, respectively, which are used as the baseline values for the simulation-based results.

In order to investigate the effect of the engine-generator power rate on the fuel economy and soot emissions, different maximum power rates $\Delta P_{textg,\mathrm{max}}$ are simulated. The minimum power rate $\Delta P_{\mathrm{g,min}}$ is considered to be a fixed parameter since soot emissions are zero during braking due to fuel cut-off and the slow decrease of power leads to multiple power conversions, resulting in a decrease of the total efficiency of the system as explained in [112].

As it can be seen from Fig. A.2, a decrease in the maximum power rate of the engine-generator helps reduce the soot emissions but it decreases fuel economy as a tradeoff. Specifically, considering a reduction of less than 0.5% in fuel economy as a reasonable compromise, limiting the maximum power rate to 19.3 kW/s could reduce soot emissions by 1.9%.

This example is useful to demonstrate the tradeoff between soot emissions and fuel economy; however, it also raises the question of whether a constant maximum power rate is the best way to address this tradeoff. This question is addressed in the

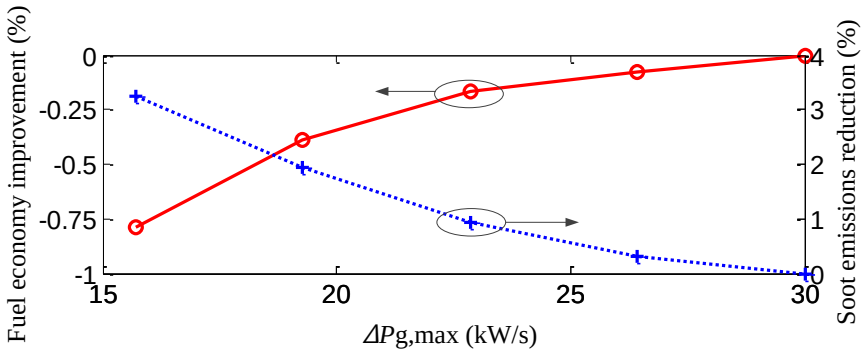

Figure A.2: The effect of a decrease in maximum engine-generator power rate on fuel economy and soot emissions

next section. Specifically, it is shown that better smoke results can be obtained if the maximum power rate is not constant but variable; i.e. the rate depends on the engine-generator power level.

A.3 Maximum Power Rate Optimization

This section describes the offline process of optimizing maximum power rate $\Delta P_{\text{g,max}}$ as a function of the engine-generator power. The goal is to optimize the maximum power rate of the engine-generator as a function of power level, which minimizes the total soot emission over a driving cycle. Thus, the discrete optimization problem is formulated by

$$\begin{aligned} \min_{\Delta P_{\text{g,max}}(d)} \quad & J = \frac{1}{N_{\text{s}}} \sum_{k=1}^{N_{\text{s}}} \int_{t_k}^{t_k+t_{\text{cycle}}} \dot{m}_{\text{soot}}\, dt, \\ \text{s.t.} \quad & \alpha \geq \alpha_* \\ & d = h\left(P_{\text{g}}\right) \in \left\{d_1, d_2, \ldots, d_{l_1}\right\}, d_i \subset \mathbb{R}_{\geq 0}, i = 1, 2, \ldots, l_1 \\ & \Delta P_{\text{g,max}}(d) \in \left\{\beta_1, \beta_2, \ldots, \beta_{l_2}\right\}, \beta_j \in \mathbb{R}_{>0}, j = 1, 2, \ldots, l_2 \end{aligned} \tag{A.2}$$

where $\dot{m}_{\text{soot}}$ is the soot emissions rate and α is the fuel economy defined in Eq. (A.1). The minimum allowed fuel economy α_* is set to 3.265 km/l (7.68 mpg); i.e., fuel economy is allowed to be reduced from 3.278 km/l (7.71 mpg) to 3.265 km/l (7.68 mpg) by 0.4%. The reference fuel economy is obtained from the MPC-based power management without the optimized power rate constraint map. The function h is a discrete mapping from the engine-generator power P_{g} to d_i, partitions of power capability of the engine-generator; e.g., $d_1 = [0\ 25)$ and $d_2 = [25\ 50)$. In each partition

Table A.2: Input Parameters of Genetic Algorithm

Parameter	Value
Number of population	30
Number of generation	50
Probability of crossover	0.8
Probability of mutation	0.01

d_i, the maximum power rate $\Delta P_{\mathrm{g,max}}$ is set to β_j, and lower and upper bounds of β_j are defined by considering vehicle requirements and engine soot generation. Integer variables l_1 and l_2 denote the number of design variables (i.e., the power rates for different d_i's) and the size of design space (i.e., the discrete set of values the power rates can assume), respectively.

With respect to solving this discrete optimization problem, algorithms such as Genetic Algorithm and Simulated Annealing are good for searching the global optimum; thus, those algorithms have been applied to optimize the design and control strategy of HEVs [144–149]. However, a large number of iterations are required to guarantee the global optimality, which is a challenge in this study, since each iteration takes several minutes in vehicle simulation. To overcome this drawback, a three-step discrete optimization process is conducted as follows:

1. Find candidate solutions using Genetic Algorithm.

2. Redefine the lower and upper bound for each variable.

3. Determine the optimal solution using Exhaustive Search in the bounded range.

Figure A.3 and Table A.2 show parameters for the optimization problem (A.2) and parameters for GA, respectively. It is noted that the total number of every possible case in the initial design space (gray shaded area in Fig. A.3) is 8^8, which is impractical to apply ES. However, the search region is significantly reduced by using GA results as shown in blue-shaded area in Fig. A.3. Thus, only 648 cases, 0.004% of every possible case, need to be explored by ES. Then, the optimal power rate constraint map, which is the blue colored line in Fig. A.3, is obtained from ES results and compared to seven power rate constraint maps resulting in the least soot emissions over the UAC cycle. All of the power rate constraint maps enforce the power rate of the engine-generator to be decreased with power above 75 kW. This result means that these solutions behave effectively as a low-pass filter incorporating

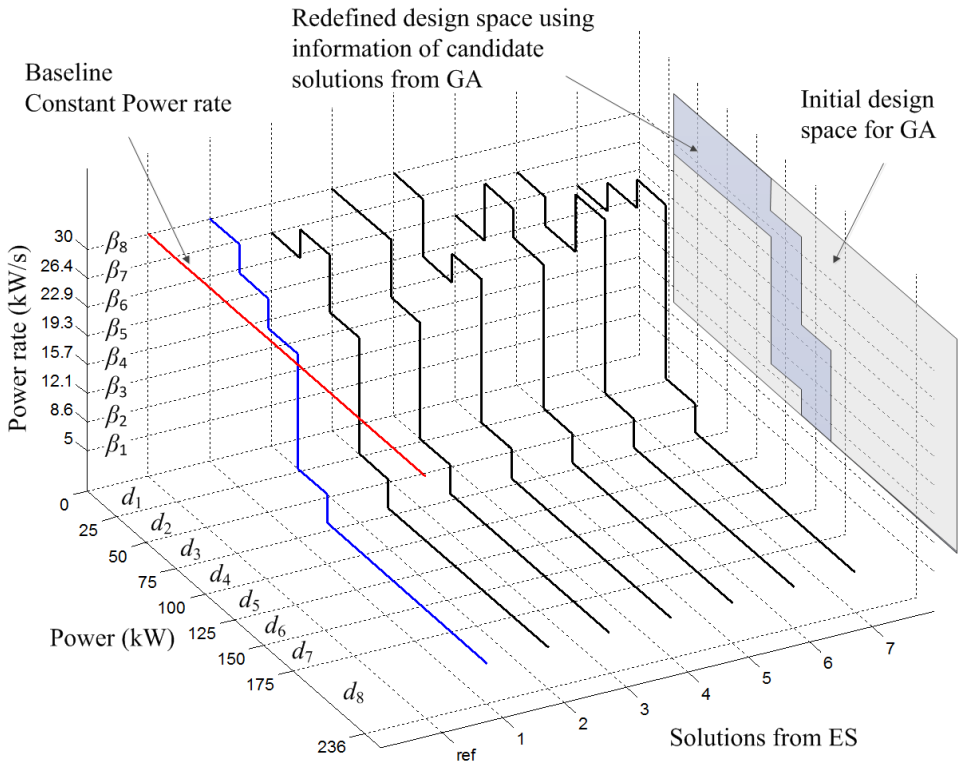

Figure A.3: Optimal solutions from ES to adjust the maximum power rate of the engine-generator depending on power level

load-leveling as used in [112]. Figure A.4 summarizes the reduction in soot emission and the compromise in fuel economy from the model-based simulation. The total soot emission could be successfully reduced by 4.0 % with the optimal power rate constraint map without significantly compromising fuel economy; fuel economy is reduced by 0.4% only. This is two times the reduction in soot emissions that was obtained with a constant maximum engine power rate constraint in Section A.

The results reported thus far are simulation-based and are obtained using a quasi-static map for soot emissions. While the quasi-static map is useful for design purposes, it is reasonable to expect the actual reduction in soot emissions to be higher than what is predicted by the quasi-static map, because it has been reported that more than 50% of soot emissions are generated during transients [142]. Therefore, to better assess the extent that the power rate constraint map can reduce soot emissions, this map is experimentally evaluated in an engine-in-the-loop simulation framework described in the following section.

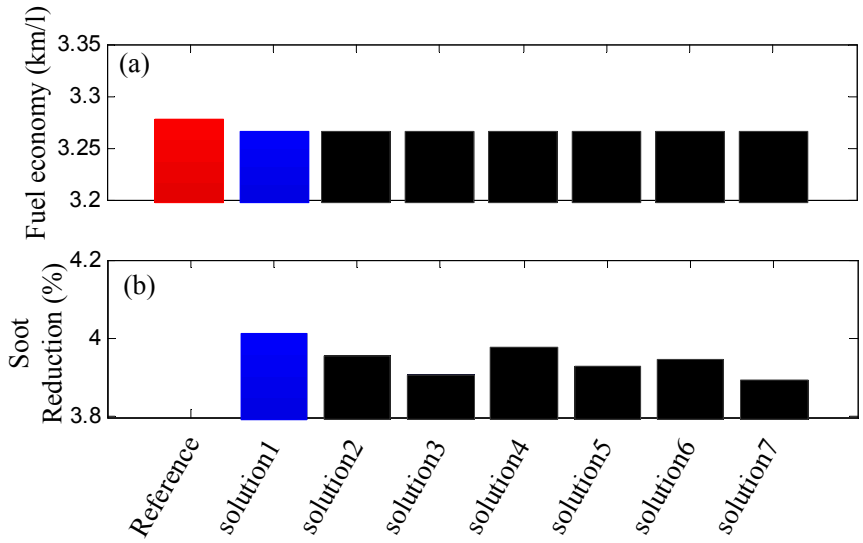

Figure A.4: Simulation-based comparison of solutions from ES with reference: (a) fuel economy and (b) reduction in soot emissions

A.4 Experimental Results

For experimental evaluation, a networked engine-in-the-loop simulation [137–139] of the vehicle system is considered, where the engine is the hardware component and the remaining components of the vehicle system (i.e., generator, battery, motors, vehicle dynamics, and driver) are mathematically modeled as described in Appendix B. The overview of the networked system architecture is illustrated in Fig. A.5.

A.4.1 Engine-in-the-loop setup

The hardware component of interest for this work is a Navistar 6.4L V8 diesel engine with 260 kW rated power at 3000 rpm and a rated torque of 880 Nm at 2000 rpm. It is intended for a variety of medium-duty truck applications covering the range between classes IIB and VII, and features technologies such as high pressure common rail fuel injection, twin sequential turbochargers, and exhaust gas recirculation. A high-fidelity AC electric dynamometer couples the physical engine with the simulation models in real-time and operates in speed control mode. The setup can be connected to Simulink for integration with mathematical models, allowing for a real-time hardware-in-the-loop simulation. This connection is achieved through an EMCON 400 flexible test bed with an ISAC 400 extension.

Transient soot emissions are measured with a Differential Mobility Spectrometer (DMS) 500 manufactured by Cambustion Ltd. in the form of temporally resolved particulate concentrations. The DMS500 offers measurement of different particle

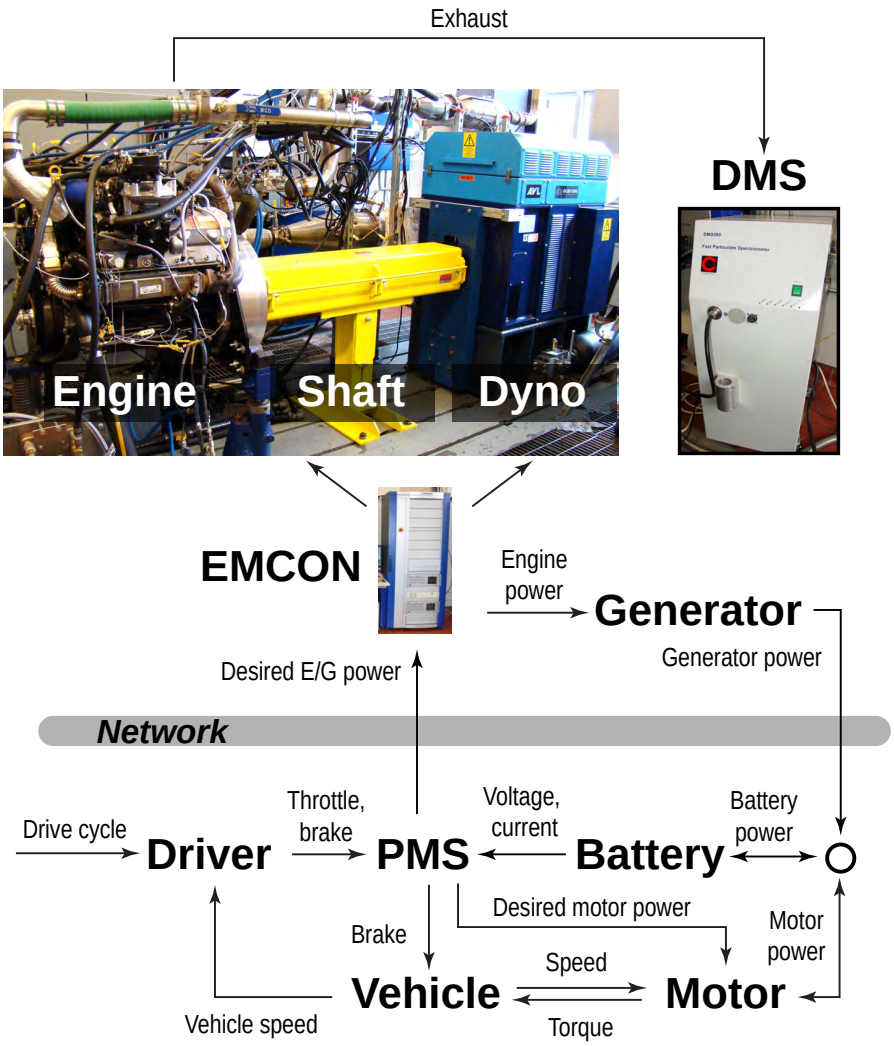

Figure A.5: The overview of the engine-in-the-loop vehicle system simulation architecture used in this case study. The engine model used for MPC development is replaced with an actual engine.

sizes by identifying the mobility of particles with a sampling frequency of 10 Hz and a response time of 200 ms. Therefore, the DMS 500 makes it possible to analyze the time evolution of the soot emissions.

A.4.2 Experimental results and discussion

The MPC-based power management strategy with the power rate constraint map is implemented in the SHEV model and evaluated via the engine-in-the-loop test setup. The constraint map obtained from the simulation-based design is directly utilized in the experiments without any further tuning. Since the electrometer detectors are sensitive and show drift when the detectors are exposed to high concentrations for long time period (e.g. four minutes), only the middle part of the UAC, the most

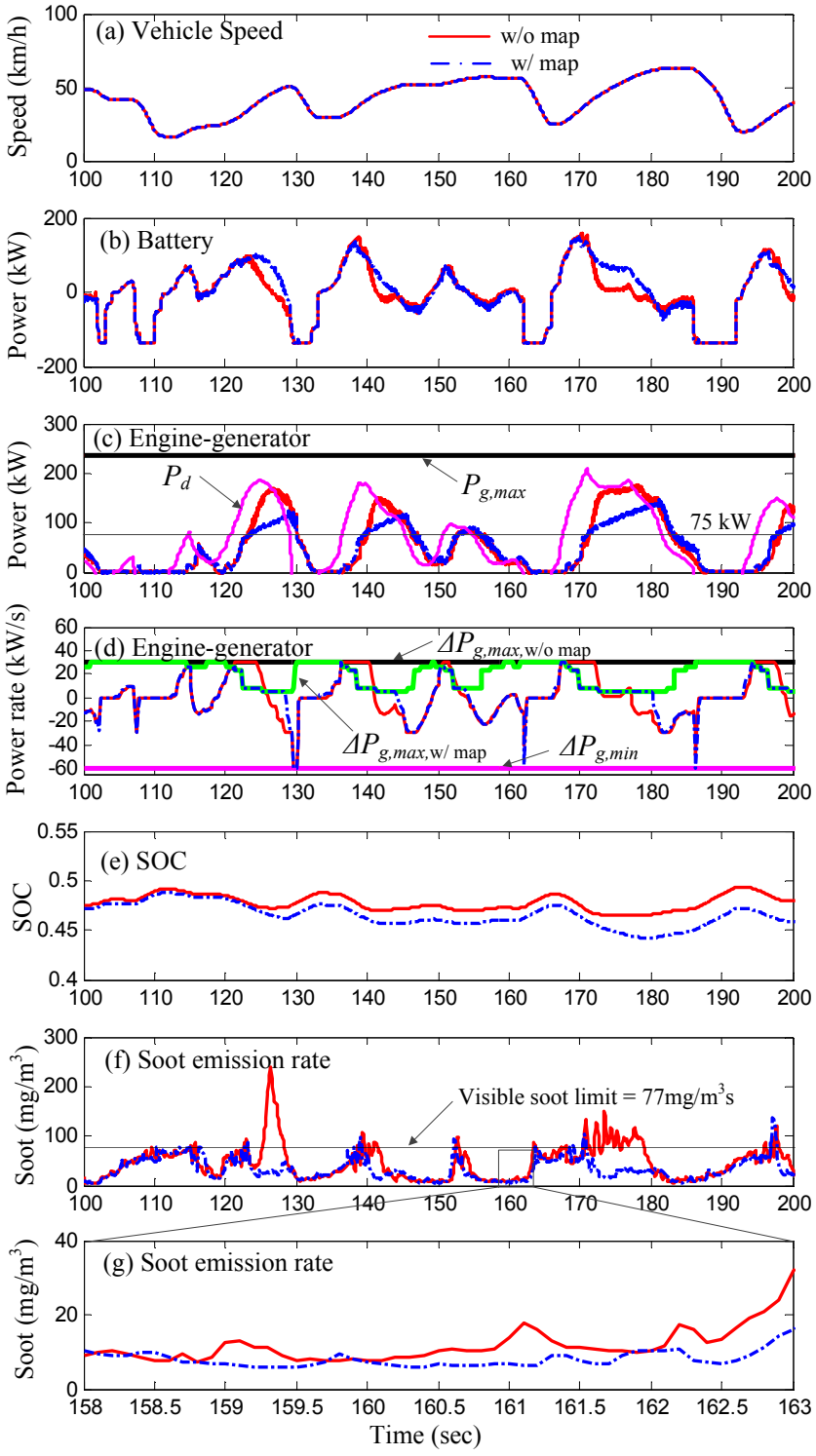

Figure A.6: Transient behaviors with and without the optimized power rate constraint map over UAC: (a) vehicle speed, (b) battery power, (c) engine-generator power, (d) engine-generator power rate, (e) battery SOC, (f) soot emissions rate, and (g) soot emissions rate (from 158 to 163 seconds)

aggressive part, is used for the measurement of soot emissions. Fuel consumption is measured over the entire UAC. It was found that the total numbers of SOC sustainability satisfaction, N_s's, for the baseline and optimal solution are 70 and 250, respectively.

To highlight the performance of the strategy, specific time periods from 100 to 200 seconds are shown in Fig. A.6. As seen from Fig. A.6(a), there is no difference in vehicle speed with and without the power rate constraint map, implying that the vehicle performance in this drive cycle is not deteriorating when the map is introduced. The responses of the battery and the engine-generator are influenced by the power rate constraint map as shown in Fig. A.6(b) and A.6(c). Above the power level of 75 kW, the map enforces the engine-generator to provide power gradually; i.e., over 75 kW, the maximum power rate becomes an active constraint. Figure A.6(f) shows that soot emissions are dramatically reduced whenever the power rate is limited: 75% of peak value of soot emissions can be reduced by smooth engine-generator operations. When the engine-generator power rate is limited, soot emissions are implicitly controlled within an upper bound which is around 77 mg/m^3 – the minimum concentration at which soot emissions are visible [104].

The benefit of the power rate constraint map is observed not only during aggressive increase of power demand, but also during the near idle regions following the peak demands. In the high power demand regions, since the engine-generator power is increased slowly, the remainder of the power demand needs to be satisfied by the battery, resulting in lower battery SOCs as shown in Fig. A.6(b) and A.6(e). Consequently, the engine-generator has to charge the battery for SOC regulation when vehicle power demand is not high, avoiding high soot emissions near the engine idling condition as seen from Fig. A.6(g).

As a result of the power rate constraint map, the total soot emission is reduced by 44.5% without significantly compromising fuel economy: fuel economy is reduced from 3.150 km/l (7.41 mpg) to 3.142 km/l (7.39 mpg) by 0.3% only. Results for the fuel economy and total soot emission obtained in simulations and experiments are compared and summarized in Fig. A.7(a) and (b). As expected, the soot emissions reduction performance observed in the experiments exceeds the prediction of the simulations, because the quasi-static soot emissions map used in the simulations does not fully capture the magnitude of soot emissions during transients. These results could lead to additional benefits that are beyond the scope of this study. For example, a reduction in engine-out soot emissions could positively affect the design and control

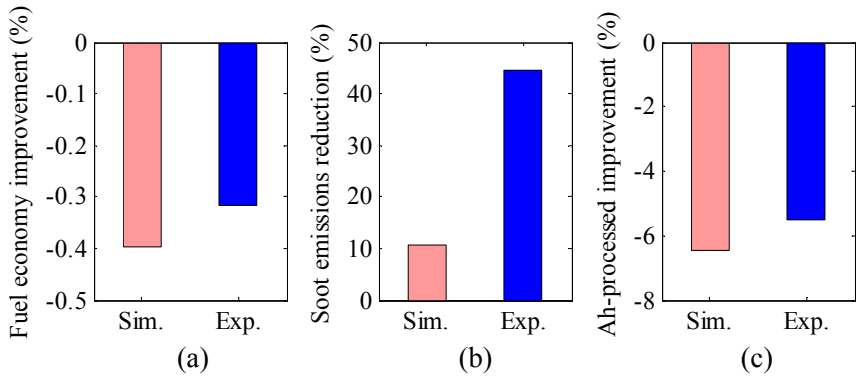

Figure A.7: Comparison of percentage improvement in performance from simulations and experiments using the power rate constraint map: (a) fuel economy, (b) soot emissions, and (c) effective Ah-processed; soot emissions in experiments are measured for 240 seconds in the middle part of military cycle since the electrometer detectors show drift when they are exposed to high concentrations for long time period.

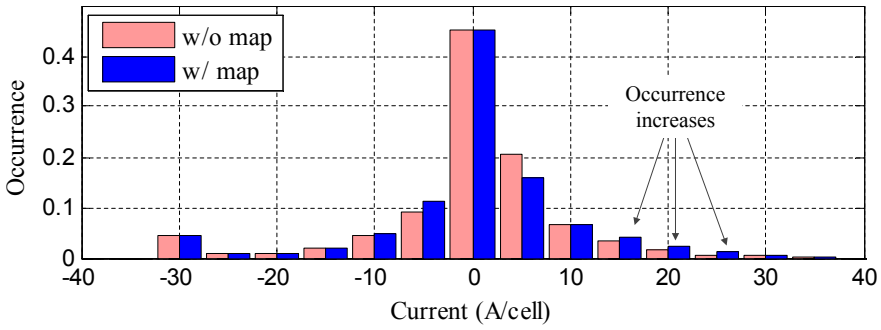

Figure A.8: Histogram of current of the battery cell: using the power rate constraint map leads to a increase in the occurrence of current rates between 15 and 25 A/cell as a tradeoff.

of the Diesel Particulate Filter in the aftertreatment system.

This significant reduction in soot emissions with only a minor compromise in fuel economy is not achieved without a cost. Figure A.8 highlights the cost in terms of the battery usage. Since the battery provides propulsion power when the engine power is actively limited by the power rate constraint map, the occurrence of current rates between 15 A/cell and 25 A/cell increases, which could translate to an increase in battery degradation as a tradeoff.

To estimate the additional battery degradation over the driving cycle due to the power rate constraint map, the effective Ah-processed model in [141] is used. This approach is based on the fatigue analysis under the assumption of linear cumulative

damage. The effective accumulated Ah-processed is calculated by

$$\mathrm{Ah}_{\mathrm{eff}} = \int_0^{t_f} \kappa(T_{\mathrm{b}}, \mathrm{SOC})|I_{\mathrm{b}}|dt, \tag{A.3}$$

where the severity factor κ is a nonlinear function of operating temperature T_{b} and SOC. The severity factor collapses in our case to a constant due to the narrow operating range of the battery SOC and assumed perfect battery cooling. As shown in Fig. A.7(c), the effective accumulated Ah-processed increases from 3.51 Ah to 3.71 Ah by 5.5% by using the optimized power rate constraint map. This increase in Ah-processed could lead to a corresponding decrease in battery life.

A.5 Conclusion

An MPC-based power management strategy is developed to reduce soot emissions in a diesel SHEV with a minimal compromise in fuel economy. This objective is achieved through an optimized constraint map for adjusting the maximum allowable power rate of the engine-generator unit. A quadratic programming was used to solve the MPC problem for splitting power demand between the engine-generator unit and the battery. To obtain the power rate constraint map for minimal soot emissions, a three-step discrete optimization process has been conducted by sequentially utilizing Genetic Algorithm and Exhaustive Search.

The engine performance with respect to soot emissions and fuel economy using the power rate constraint map has been experimentally evaluated. Experimental results show that the regulated engine operation using the proposed power rate constraint map results in reduced soot emissions. Quantitatively, the total soot emission is reduced by 44.5% while fuel economy is compromised by only 0.3%. Battery statistics show that optimized MPC-based power management strategy increases the medium-level current operations as a tradeoff. Specifically, the Ah-processed increases by 5.5%, and a corresponding decrease could be expected in the battery capacity.

As a first step to consider fuel economy and soot emissions simultaneously in an MPC-based supervisory control framework, this work utilized a quasi-static soot emissions map. A transient soot emissions model could improve the performance even further. Therefore, developing such a model and evaluating its performance within the methodology presented in this paper is an important direction for future research. In addition, the influence of the power demand prediction on the performance will be investigated.

APPENDIX B

Series Hybrid Electric Vehicle Modeling

This appendix presents the SHEV system model.

Figures B.1 and B.2 show the engine torque and soot emission maps obtained from a Navistar 6.4L V8 diesel engine [143]. The engine torque map is augmented by a PI fuel controller sub-model generating the engine rack position ($\zeta(t) \in [0, 1]$), given by

$$\zeta(t) = k_{\mathrm{P}} \Delta\tau_{\mathrm{e}} + k_{\mathrm{I}} \int \Delta\tau_{\mathrm{e}} dt, \tag{B.1}$$

where $\Delta\tau_{\mathrm{e}}$ is the error between the desired and actual engine torque; k_{P} and k_{I} are proportional and integral gains, respectively. To represent the effect of turbocharger lag on transient response during rapid increases of engine rack positions, the fuel mass is filtered by a first-order filter. The engine-generator unit is assumed to be fully warmed up so that the effects of temperature are ignored. Figure B.3 illustrates the efficiency of the generator in [150].

Figure B.4 shows the efficiency of the motor η_{m} is expressed as a function of motor torque τ_{m} and motor speed ω_{m}. Maximum output torque of the motor $\tau_{\mathrm{m,max}}$ is governed between the continuous torque $\tau_{\mathrm{m,cont}}$ and the peak torque $\tau_{\mathrm{m,peak}}$ accounting for the heat index γ as follows:

$$\tau_{\mathrm{m,max}} = \tau_{\mathrm{m,cont}} + (1 - \gamma)\tau_{\mathrm{m,peak}}, \tag{B.2}$$

$$\frac{d\gamma}{dt} = -\frac{0.3}{180}\left(\frac{\tau_{\mathrm{m}}}{\tau_{\mathrm{m,cont}}} - 1\right), \gamma(0) = 0.3, \tag{B.3}$$

where $\tau_{\mathrm{m,cont}}$ and $\tau_{\mathrm{m,peak}}$ are a function of the motor speed ω_{m}. The heat index γ emulates the change in the torque limit based on operating temperature as introduced

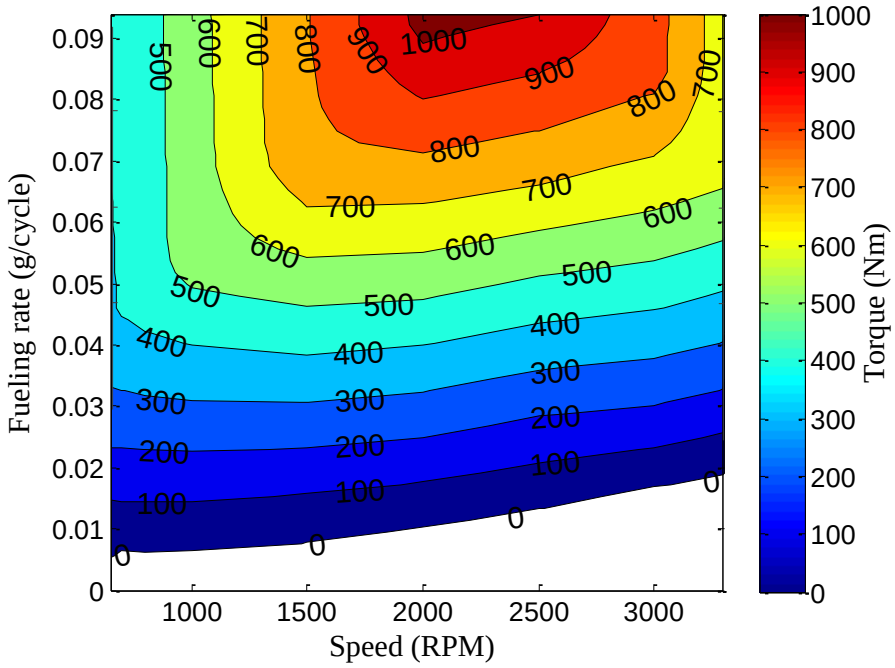

Figure B.1: Engine torque map as a function of speed and fuel rate

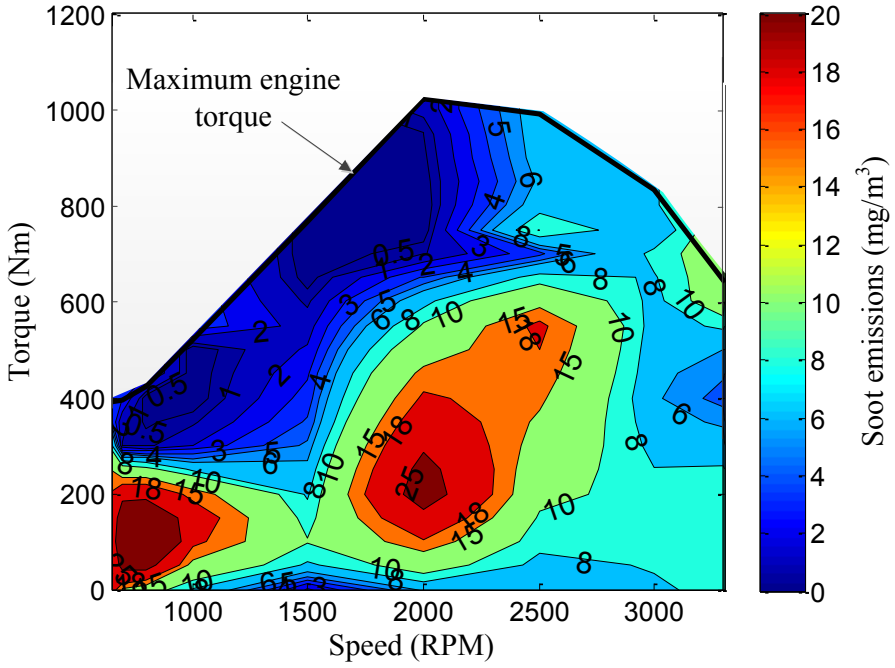

Figure B.2: Soot emissions map as a function of speed and torque

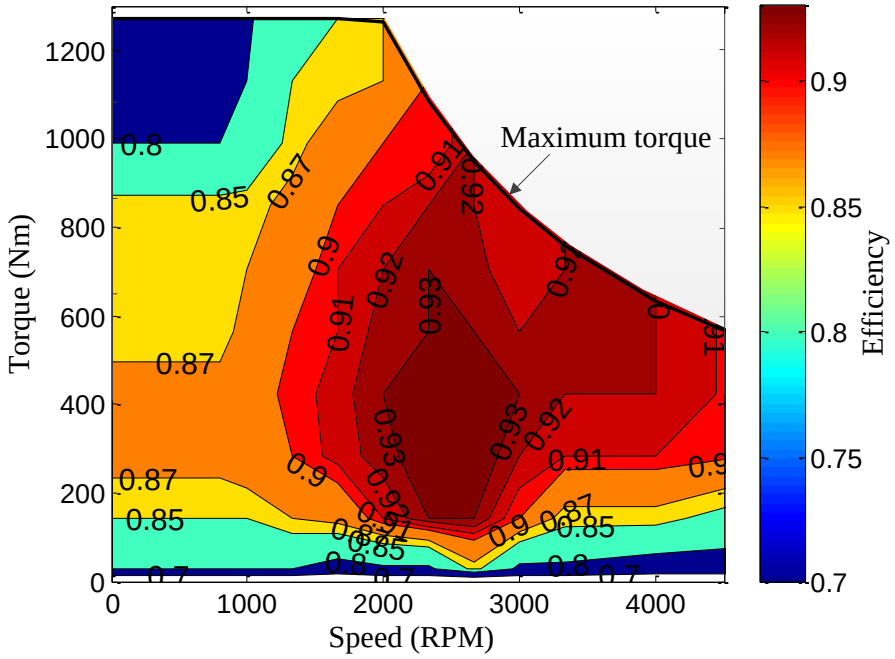

Figure B.3: Generator efficiency map as a function of speed and torque

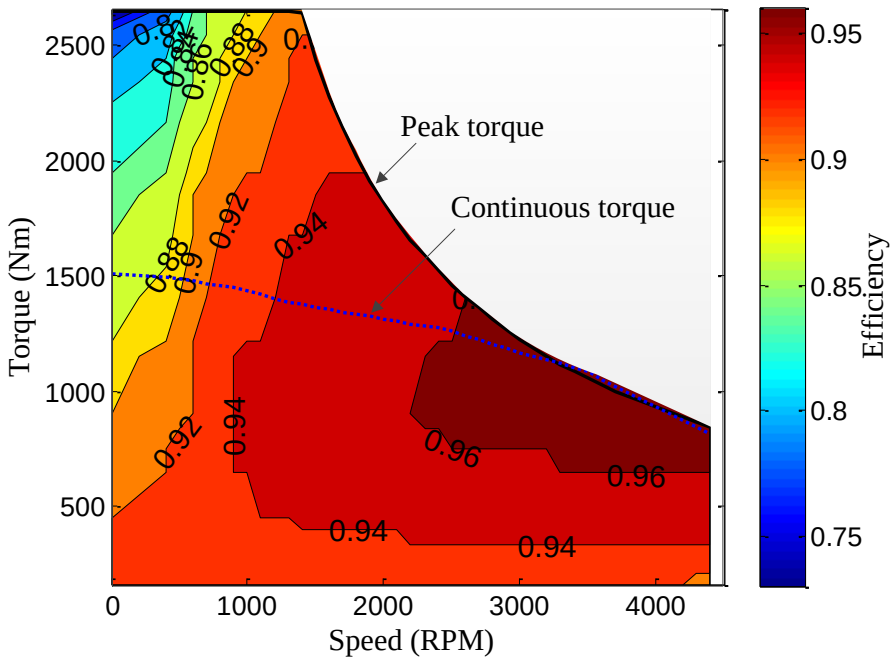

Figure B.4: Motor efficiency map superimposed by peak and continuous torques

Table B.1: Battery cell and pack specifications

Parameter	Value	Unit
Nominal Voltage	3.3	V
Minimum Voltage	3.3	V
Maximum Voltage	3.3	V
Nominal Capacity	2.3	Ah
Number of Cells in Series	130	-
Number of Cells in Parallel	10	-

in Powertrain Systems Analysis Toolkit (PSAT) developed by Argonne National Laboratory [150].

A 9.27 kWh (281 Ah) lithium ion battery pack with Lithium-Iron-Phosphate ($LiFePO_4$ or LFP) cells by A123 is considered and the battery is modeled using an OCV-R-RC-RC equivalent-circuit approach. The open circuit voltage $V_{\rm oc}$, internal resistances (R_s, R_1, and R_2) and capacitances (C_1 and C_2) during discharging and charging are determined using the parameter identification technique presented in [49]. The specifications for the LFP battery are summarized in Table B.1.

Terminal voltage $V_{\rm t}$ of the battery is calculated by using

$$V_{\rm t} = V_{\rm oc} - V_1 - V_2 - I_{\rm b} R_s, \tag{B.4}$$

where V_1 and V_2 are polarization voltages across the capacitances C_1 and C_2, respectively, and calculated based on the following dynamic equations:

$$\frac{dV_i}{dt} = \frac{1}{C_i}\left(I - \frac{V_i}{R_i}\right), \quad i = 1, 2. \tag{B.5}$$

The sign convention is such that positive current denotes battery discharging.

A point-mass representation is used for the vehicle. The longitudinal dynamics of the vehicle is calculated through the equation

$$M_{\rm veh}\frac{dv_{\rm veh}}{dt} = F_{\rm prop} - F_{\rm brk} - F_{\rm rr} - F_{\rm wr}, \tag{B.6}$$

where M_{veh} is the mass of the vehicle, respectively, F_{prop} is the propulsion force, F_{brk} is the braking force, and F_{rr} is the rolling resistance force expressed by

$$F_{\text{rr}} = f_{\text{r}} M_{\text{veh}} a_{\text{g}}, \tag{B.7}$$

where f_{r} is the rolling resistance, a_{g} is the gravitational acceleration. The wind resistance force F_{wr} is calculated by using

$$F_{\text{wr}} = \frac{1}{2} \rho_{\text{air}} C_{\text{d}} A_{\text{veh}} v_{\text{veh}}^2, \tag{B.8}$$

where ρ_{air} is the air density, C_{d} is the drag coefficient, and A_{veh} is the frontal area of the vehicle. The road grade is not considered in the driving cycles in this study.

The driver model, which takes the desired and actual vehicle velocities as inputs and provides propulsion or braking power demands, is adopted from [137] and is a PI controller.

APPENDIX C

Formulation of Model Predictive Control

C.1 The choice of L1 norm cost function

Let the sum of fueling rate $\dot{m}_f$ over the finite horizon N_s to be

$$\Lambda = \sum_{i=1}^{N_\mathrm{s}} \dot{m}_f(i). \tag{C.1}$$

Then, the sum of the squares of fueling rate can be expressed by

$$\sum_{i=1}^{N_\mathrm{s}} \dot{m}_f(i)^2 = \frac{\Lambda^2}{N_\mathrm{s}} + N_\mathrm{s}\sigma^2, \tag{C.2}$$

where σ is the standard deviation of fueling rate over the finite horizon. The variance is included as a penalty term in Eq. (C.2), resulting in that the minimization problem (C.2) finds an optimal solution minimizing not only the sum of fueling rate but also the variation of fueling rate. Thus, the output $\dot{m}_f^{0.5}$ is used in this study since the total fuel consumption is of interest in power management.

C.2 Matrix-vector form for Model Predictive Control

Equation (5.7) is iterated in order to predict outputs over the future horizon as it follows:

$$\begin{bmatrix} \hat{\underline{x}}_{k+1|k} \\ \vdots \\ \hat{\underline{x}}_{k+N_\mathrm{p}|k} \end{bmatrix} = \mathbf{A}\underline{x}_k + \mathbf{B}\Delta\underline{U} + \mathbf{B_1} + \mathbf{G_1},$$

$$\begin{bmatrix} \hat{\underline{y}}_{k|k} \\ \vdots \\ \hat{\underline{y}}_{k+N_\mathrm{p}|k} \end{bmatrix} = \mathbf{C}\begin{bmatrix} \hat{\underline{x}}_{k|k} \\ \vdots \\ \hat{\underline{x}}_{k+N_\mathrm{p}|k} \end{bmatrix} + \mathbf{H}\begin{bmatrix} \hat{\underline{v}}_{k|k} \\ \vdots \\ \hat{\underline{v}}_{k+N_\mathrm{p}|k} \end{bmatrix} + \mathbf{G_2} \tag{C.3a}$$

where

$$\mathbf{A} = \begin{bmatrix} A_d \\ \vdots \\ A_d^{N_\mathrm{p}} \end{bmatrix}, \tag{C.4a}$$

$$\mathbf{B} = \begin{bmatrix} I & \cdots & 0 \\ \vdots & \ddots & \vdots \\ \sum_{i=0}^{N_\mathrm{p}-1} A_d^i & \cdots & \sum_{i=0}^{N_\mathrm{p}-N_\mathrm{c}} A_d^i \end{bmatrix} B_d, \tag{C.4b}$$

$$\mathbf{B_1} = \begin{bmatrix} I \\ \vdots \\ \sum_{i=0}^{N_\mathrm{p}-1} A_d^i \end{bmatrix} B_d\underline{u}_{k-1}, \tag{C.4c}$$

$$\mathbf{G_1} = \begin{bmatrix} I \\ \vdots \\ \sum_{i=0}^{N_\mathrm{p}-1} A_d^i \end{bmatrix} G_1, \tag{C.4d}$$

$$\mathbf{C} = diag\underbrace{\begin{bmatrix} C & \cdots & C \end{bmatrix}}_{(N_\mathrm{p}+1)\times\dim C}, \tag{C.4e}$$

$$\mathbf{H} = diag\underbrace{\begin{bmatrix} H & \cdots & H \end{bmatrix}}_{(N_\mathrm{p}+1)\times\dim H}, \tag{C.4f}$$

$$\mathbf{G_2} = \underbrace{\begin{bmatrix} G_2^T & \cdots & G_2^T \end{bmatrix}^T}_{(N_\mathrm{p}+1)\times\dim G_2^T}. \tag{C.4g}$$

The sequences of the engine-generator are given by

$$\begin{bmatrix} \hat{\underline{v}}_{k|k} \\ \vdots \\ \hat{\underline{v}}_{k+N_\mathrm{p}|k} \end{bmatrix} = \mathbf{P}_\mathrm{d} - \underline{\mathbf{u_0}} - \mathbf{K_1}\Delta\underline{U} \tag{C.5}$$

with

$$\mathbf{P}_\mathrm{d} = \begin{bmatrix} P_{\mathrm{d},k|k} & \cdots & P_{\mathrm{d},k+N_\mathrm{p}|k} \end{bmatrix}^T, \tag{C.6a}$$

$$\underline{\mathbf{u_0}} = \underbrace{\begin{bmatrix} \underline{u}_{k-1} & \cdots & \underline{u}_{k-1} \end{bmatrix}^T}_{(N_\mathrm{p}+1)\times 1}, \tag{C.6b}$$

$$\mathbf{K_1} = \begin{bmatrix} 1 & 0 & \cdots & 0 \\ \vdots & \ddots & \vdots & \vdots \\ 1 & 1 & 1 & 1 \\ \vdots & \vdots & \vdots & \vdots \\ 1 & \cdots & \cdots & 1 \end{bmatrix}_{(N_\mathrm{p}+1)\times N_\mathrm{c}}. \tag{C.6c}$$

The outputs over the prediction horizon $\mathbf{Y} = [\underline{y}_{k|k}, \cdots, \underline{y}_{k+N_\mathrm{p}|k}]^T$ can be expressed by

$$\mathbf{Y} = \mathbf{C_1}\underline{x}_k + \mathbf{\Phi_1}\Delta\underline{U} + \mathbf{\Phi_2} \tag{C.7}$$

where

$$\mathbf{C_1} = \mathbf{C}\begin{bmatrix} I \\ \mathbf{A} \end{bmatrix}, \tag{C.8a}$$

$$\mathbf{\Phi_1} = \mathbf{C}\begin{bmatrix} 0 \\ \mathbf{B} \end{bmatrix} - \mathbf{K_1}, \tag{C.8b}$$

$$\mathbf{\Phi_2} = \begin{bmatrix} 0 \\ \mathbf{B_1} \end{bmatrix} + \mathbf{H} + \begin{bmatrix} 0 \\ \mathbf{G_1} \end{bmatrix} + \mathbf{G_2}. \tag{C.8c}$$

Finally, matrices for the Quadratic Programming, Eq. (5.9) are expressed as following:

$$\mathbf{\Psi_1} = 2(\mathbf{\Phi_1}^T W_1 \mathbf{\Phi_1} + \mathbf{K_1}^T W_2 \mathbf{K_1} + W_3), \tag{C.9a}$$

$$\begin{aligned}\mathbf{\Psi_2} = {} & 2\Big(\underline{x}_{\mathrm{o}}^T \mathbf{C_1}^T + \mathbf{\Phi_2}\Big) W_1 \mathbf{\Phi_1} \\ & - 2\Big((\mathbf{K_1}^T \mathbf{K_1})^{-1} \mathbf{K_1} (\mathbf{P_d} - \underline{\mathbf{u}}_{\mathrm{o}} - \underline{\mathbf{v}}_{\mathrm{o}})\Big)^T W_2 + 2\underline{\mathbf{u}}_{\mathrm{o}} W_3 \mathbf{K_1},\end{aligned} \tag{C.9b}$$

$$\mathbf{\Gamma_1} = \Big[\mathbf{K_2}^T \quad -\mathbf{K_2}^T \quad \mathbf{K_2}^T \quad -\mathbf{K_2}^T \quad \mathbf{I}^T \quad -\mathbf{I}^T \quad -\mathbf{B}^T \quad \mathbf{B}^T\Big]^T, \tag{C.9c}$$

$$\mathbf{\Gamma_2} = \begin{bmatrix} \mathbf{P_{b,max}} - \underline{\mathbf{u}}_{\mathrm{o}} \\ -\mathbf{P_{b,min}} + \underline{\mathbf{u}}_{\mathrm{o}} \\ \mathbf{P_d} - \underline{\mathbf{u}}_{\mathrm{o}} \\ \mathbf{P_{g,max}} - \mathbf{P_d} + \underline{\mathbf{u}}_{\mathrm{o}} \\ \mathbf{K_2}^{-1}(\underline{\mathbf{u}}_{\mathrm{o}} + \underline{\mathbf{v}}_{\mathrm{o}} - \mathbf{P_d}) + \mathbf{\Delta P_{g,max}} \\ \mathbf{K_2}^{-1}(\mathbf{P_d} - \underline{\mathbf{u}}_{\mathrm{o}} - \underline{\mathbf{v}}_{\mathrm{o}}) - \mathbf{\Delta P_{g,min}} \\ \mathbf{A}\underline{x}_{\mathrm{o}} + \mathbf{B_1} + \mathbf{G_1} - \mathbf{Y_{1,min}} \\ -\mathbf{A}\underline{x}_{\mathrm{o}} - \mathbf{B_1} - \mathbf{G_1} + \mathbf{Y_{1,max}} \end{bmatrix}, \tag{C.9d}$$

where

$$\mathbf{K_2} = \begin{bmatrix} 1 & 0 & \cdots & 0 \\ \vdots & \ddots & \vdots & \vdots \\ 1 & 1 & 1 & 1 \end{bmatrix}_{N_{\mathrm{c}} \times N_{\mathrm{c}}}, \tag{C.10}$$

$$\mathbf{P_{b,max}} = \begin{bmatrix} P_{\mathrm{b,max}} & \cdots & P_{\mathrm{b,max}} \end{bmatrix}^T, \tag{C.11}$$

$$\mathbf{P_{b,min}} = \begin{bmatrix} P_{\mathrm{b,min}} & \cdots & P_{\mathrm{b,min}} \end{bmatrix}^T, \tag{C.12}$$

$$\mathbf{\Delta P_{g,max}} = \begin{bmatrix} \Delta P_{\mathrm{g,max}} & \cdots & \Delta P_{\mathrm{g,max}} \end{bmatrix}^T, \tag{C.13}$$

$$\mathbf{\Delta P_{g,min}} = \begin{bmatrix} \Delta P_{\mathrm{g,min}} & \cdots & \Delta P_{\mathrm{g,min}} \end{bmatrix}^T, \tag{C.14}$$

$$\mathbf{Y_{1,min}} = \begin{bmatrix} \mathrm{SOC}_{\min} & \cdots & \mathrm{SOC}_{\min} \end{bmatrix}^T, \tag{C.15}$$

$$\mathbf{Y_{1,max}} = \begin{bmatrix} \mathrm{SOC}_{\max} & \cdots & \mathrm{SOC}_{\max} \end{bmatrix}^T. \tag{C.16}$$

BIBLIOGRAPHY

BIBLIOGRAPHY

[1] M. Sivak, "Has motorization in the us peaked?." http://deepblue.lib.umich.edu/bitstream/handle/2027.42/98098/102947.pdf, 2013. [Online; accessed 19-Nov-2013].

[2] U.S. Energy Information Administation, "Spot prices." http://www.eia.gov/petroleum/data.cfm#prices, 2013. [Online; accessed 19-Nov-2013].

[3] S. Davis, S. Diegel, and R. Boundy, *Transportation Energy Data Book: Edition 32*. Oak Ridge National Laboratory, 2013.

[4] BBVA, "The future of world car fleet: The road ahead." http://www.bbvaresearch.com/KETD/fbin/mult/The_Future_of_the_World_Car_Fleet_The_Road_Ahead_BBVA_Research_tcm348-362804.pdf, 2012. [Online; accessed 19-Nov-2013].

[5] N. Tanaka, "Transport, energy and environment: Where are we going and how do we change it?," in *The Ministerial Conference on Global Environment and Energy in Transport*, (Tokyo, Japan), Jan 14-16 2009.

[6] S. Barsali, C. Miulli, and A. Possenti, "A control strategy to minimize fuel consumption of series hybrid electric vehicles," *Energy Conversion, IEEE Transactions on*, vol. 19, no. 1, pp. 187–195, 2004.

[7] H. Yoo, S.-K. Sul, Y. Park, and J. Jeong, "System integration and power-flow management for a series hybrid electric vehicle using supercapacitors and batteries," *Industry Applications, IEEE Transactions on*, vol. 44, no. 1, pp. 108–114, 2008.

[8] Y. Kim, T. Ersal, A. Salvi, A. G. Stefanopoulou, and Z. Filipi, "Engine-in-the-loop validation of a frequency domain power distribution strategy for series hybrid powertrains," in *Proceedings of the IFAC Workshop on Engine and Powertrain Control Simulation and Modeling*, pp. 432–439, Oct 23-25 2012.

[9] S. Di Cairano, W. Liang, I. V. Kolmanovsky, M. L. Kuang, and A. M. Phillips, "Power smoothing energy management and its application to a series hybrid powertrain," *Control Systems Technology, IEEE Transactions on*, vol. 21, no. 6, pp. 2091–2103, 2012.

[10] M. Ehsani, K. Rahman, and H. Toliyat, "Propulsion system design of electric and hybrid vehicles," *Industrial Electronics, IEEE Transactions on*, vol. 44, no. 1, pp. 19–27, 1997.

[11] C.-C. Lin, H. Peng, J. Grizzle, and J.-M. Kang, "Power management strategy for a parallel hybrid electric truck," *Control Systems Technology, IEEE Transactions on*, vol. 11, no. 6, pp. 839–849, 2003.

[12] A. Sciarretta, M. Back, and L. Guzzella, "Optimal control of parallel hybrid electric vehicles," *Control Systems Technology, IEEE Transactions on*, vol. 12, no. 3, pp. 352–363, 2004.

[13] J. Liu and H. Peng, "Modeling and control of a power-split hybrid vehicle," *Control Systems Technology, IEEE Transactions on*, vol. 16, no. 6, pp. 1242–51, 2008.

[14] S. Moura, H. Fathy, D. Callaway, and J. Stein, "A stochastic optimal control approach for power management in plug-in hybrid electric vehicles," *Control Systems Technology, IEEE Transactions on*, vol. 19, no. 3, pp. 545–555, 2011.

[15] H. Borhan, A. Vahidi, A. Phillips, M. Kuang, I. Kolmanovsky, and S. Di Cairano, "MPC-based energy management of a power-split hybrid electric vehicle," *Control Systems Technology, IEEE Transactions on*, vol. 20, no. 3, pp. 593–603, 2012.

[16] Z. Rao and S. Wang, "A review of power battery thermal energy management," *Renewable and Sustainable Energy Reviews*, vol. 15, no. 9, pp. 4554–4571, 2011.

[17] J. Sullivan and L. Gaines, "A review of battery life-cycle analysis: state of knowledge and critical needs," tech. rep., Argonne National Laboratory, 2010.

[18] R. Huggins, *Advanced Batteries: Materials Science Aspects, first edition.* Springer, 2008.

[19] J. Shim, R. Kostecki, T. Richardson, X. Song, and K. Striebel, "Electrochemical analysis for cycle performance and capacity fading of a lithium-ion battery cycled at elevated temperature," *Journal of Power Sources*, vol. 112, no. 1, pp. 222–230, 2002.

[20] S. Tobishima and J. Yamaki, "A consideration of lithium cell safety," *Journal of Power Sources*, vol. 81-82, no. 0, pp. 882–886, 1999.

[21] R. Spotnitz and J. Franklin, "Abuse behavior of high-power, lithium-ion cells," *Journal of Power Sources*, vol. 113, no. 1, pp. 81–100, 2003.

[22] Y. Zhang and C.-Y. Wang, "Cycle-life characterization of automotive lithium-ion batteries with linio2 cathode," *Journal of The Electrochemical Society*, vol. 156, no. 7, pp. A527–A535, 2009.

[23] L. Tan, L. Zhang, Q. Sun, M. Shen, Q. Qu, and H. Zheng, "Capacity loss induced by lithium deposition at graphite anode for $LiFePO_4$/graphite cell cycling at different temperatures," *Electrochimica Acta*, vol. 111, no. 0, pp. 802–808, 2013.

[24] G. Pistoia, *Battery operated devices and systems: From portable electronics to industrial products*. Elsevier Science Limited, 2009.

[25] G. Plett, "High-performance battery-pack power estimation using a dynamic cell model," *Vehicular Technology, IEEE Transactions on*, vol. 53, no. 5, pp. 1586–1593, 2004.

[26] M. Verbrugge and B. Koch, "Generalized recursive algorithm for adaptive multiparameter regression: Application to lead acid, nickel metal hydride, and lithium-ion batteries," *Journal of The Electrochemical Society*, vol. 153, no. 1, pp. A187–A201, 2006.

[27] K. Smith, C. Rahn, and C.-Y. Wang, "Model-based electrochemical estimation and constraint management for pulse operation of lithium ion batteries," *Control Systems Technology, IEEE Transactions on*, vol. 18, no. 3, pp. 654–663, 2010.

[28] R. D. Anderson, Y. Zhao, X. Wang, X. G. Yang, and Y. Li, "Real time battery power capability estimation," in *Proceedings of the American Control Conference*, pp. 592–597, June 2012.

[29] R. Xiong, H. He, F. Sun, X. Liu, and Z. Liu, "Model-based state of charge and peak power capability joint estimation of lithium-ion battery in plug-in hybrid electric vehicles," *Journal of Power Sources*, vol. 229, no. 0, pp. 159–169, 2013.

[30] S. Moura, J. Stein, and H. Fathy, "Battery-health conscious power management in plug-in hybrid electric vehicles via electrochemical modeling and stochastic control," *Control Systems Technology, IEEE Transactions on*, vol. 21, no. 3, pp. 679–694, 2013.

[31] D. Andrea, *Battery management systems for large lithium-ion battery packs*. Artech House Publishers, 2010.

[32] T. F. Fuller, M. Doyle, and J. Newman, "Simulation and optimization of the dual lithium ion insertion cell," *Journal of The Electrochemical Society*, vol. 141, no. 1, pp. 1–10, 1994.

[33] P. Ramadass, B. Haran, R. White, and B. N. Popov, "Mathematical modeling of the capacity fade of li-ion cells," *Journal of Power Sources*, vol. 123, no. 2, pp. 230–240, 2003.

[34] K. A. Smith, C. D. Rahn, and C.-Y. Wang, "Control oriented 1d electrochemical model of lithium ion battery," *Energy Conversion and Management*, vol. 48, no. 9, pp. 2565–2578, 2007.

[35] J. C. Forman, S. Bashash, J. L. Stein, and H. K. Fathy, "Reduction of an electrochemistry-based li-ion battery model via quasi-linearization and padé approximation," *Journal of The Electrochemical Society*, vol. 158, no. 2, pp. A93–A101, 2011.

[36] G. Ning and B. N. Popov, "Cycle life modeling of lithium-ion batteries," *Journal of The Electrochemical Society*, vol. 151, no. 10, pp. A1584–A1591, 2004.

[37] B. S. Haran, B. N. Popov, and R. E. White, "Determination of the hydrogen diffusion coefficient in metal hydrides by impedance spectroscopy," *Journal of Power Sources*, vol. 75, no. 1, pp. 56–63, 1998.

[38] V. R. Subramanian, V. D. Diwakar, and D. Tapriyal, "Efficient macro-micro scale coupled modeling of batteries," *Journal of the Electrochemical Society*, vol. 152, no. 10, pp. A2002–A2008, 2005.

[39] D. Di Domenico, A. G. Stefanopoulou, and G. Fiengo, "Lithium-ion battery state of charge and critical surface charge estimation using an electrochemical model-based extended kalman filter," *Journal of Dynamic Systems, Measurement, and Control*, vol. 132, no. 6, pp. 0613021–11, 2010.

[40] T.-K. Lee, Y. Kim, A. Stefanopoulou, and Z. Filipi, "Hybrid electric vehicle supervisory control design reflecting estimated lithium-ion battery electrochemical dynamics," in *Proceedings of the American Control Conference*, pp. 388–395, 2011.

[41] T.-K. Lee, Y. Kim, D. M. Rizzo, and Z. S. Filipi, "Battery power management in heavy-duty hevs based on the estimated critical surface charge," *International Journal of Vehicle Design*, vol. 61, no. 1, pp. 108–127, 2013.

[42] J. C. Forman, S. J. Moura, J. L. Stein, and H. K. Fathy, "Genetic identification and fisher identifiability analysis of the doyle–fuller–newman model from experimental cycling of a lifepo4 cell," *Journal of Power Sources*, vol. 210, no. 0, pp. 263–275, 2012.

[43] B. Y. Liaw, G. Nagasubramanian, R. G. Jungst, and D. H. Doughty, "Modeling of lithium ion cells – simple equivalent-circuit model approach," *Solid State Ionics*, vol. 175, no. 1-4, pp. 835–839, 2004.

[44] M. Verbrugge, "Adaptive, multi-parameter battery state estimator with optimized time-weighting factors," *Journal of Applied Electrochemistry*, vol. 37, no. 5, pp. 605–616, 2007.

[45] M. Dubarry, N. Vuillaume, and B. Y. Liaw, "From single cell model to battery pack simulation for li-ion batteries," *Journal of Power Sources*, vol. 186, no. 2, pp. 500–507, 2009.

[46] D. Andre, M. Meiler, K. Steiner, H. Walz, T. Soczka-Guth, and D. Sauer, "Characterization of high-power lithium-ion batteries by electrochemical impedance spectroscopy. ii: Modelling," *Journal of Power Sources*, vol. 196, no. 12, pp. 5349–5356, 2011.

[47] Y. Hu and S. Yurkovich, "Linear parameter varying battery model identification using subspace methods," *Journal of Power Sources*, vol. 196, no. 5, pp. 2913–2923, 2011.

[48] Y. Hu, S. Yurkovich, Y. Guezennec, and B. Yurkovich, "Electro-thermal battery model identification for automotive applications," *Journal of Power Sources*, vol. 196, no. 1, pp. 449–457, 2011.

[49] H. E. Perez, J. B. Siegel, X. Lin, A. Stefanopoulou, Y. Ding, and M. P. Castanier, "Parameterization and validation of an integrated electro-thermal LFP battery model," in *Proceedings of the ASME Dynamic Systems Control Conference*, (Fort Lauderdale, Florida, USA), pp. 41–50, Oct 17-19 2012.

[50] G. K. Prasad and C. D. Rahn, "Development of a first principles equivalent circuit model for a lithium ion battery," in *Proceedings of ASME 2012 5th Annual Dynamic Systems and Control Conference joint with the JSME 2012 11th Motion and Vibration Conference*, pp. 369–375, 2012.

[51] X. Hu, S. Li, and H. Peng, "A comparative study of equivalent circuit models for li-ion batteries," *Journal of Power Sources*, vol. 198, pp. 359–367, 2012.

[52] C.-C. Lin, H. Peng, and J. Grizzle, "A stochastic control strategy for hybrid electric vehicles," in *Proceedings of the American Control Conference*, vol. 5, pp. 4710–4715, 2004.

[53] D. Bernardi, E. Pawlikowski, and J. Newman, "General energy balance for battery systems," *Journal of the Electrochemical Society*, vol. 132, no. 1, pp. 5–12, 1985.

[54] K. E. Thomas and J. Newman, "Heats of mixing and of entropy in porous insertion electrodes," *Journal of Power Sources*, vol. 119-121, no. 1, pp. 844–849, 2003.

[55] C. R. Pals and J. Newman, "Thermal modeling of the lithium/polymer battery: I . discharge behavior of a single cell," *Journal of The Electrochemical Society*, vol. 142, no. 10, pp. 3274–3281, 1995.

[56] C. R. Pals and J. Newman, "Thermal modeling of the lithium/polymer battery: Ii . temperature profiles in a cell stack," *Journal of The Electrochemical Society*, vol. 142, no. 10, pp. 3282–3288, 1995.

[57] K. Smith and C.-Y. Wang, "Power and thermal characterization of a lithium-ion battery pack for hybrid-electric vehicles," *Journal of Power Sources*, vol. 160, no. 1, pp. 662–673, 2006.

[58] M. Guo, G. Sikha, and R. White, "Single-particle model for a lithium-ion cell: Thermal behavior," *Journal of the Electrochemical Society*, vol. 158, no. 2, pp. 122–32, 2011.

[59] M. Guo, G. Sikha, and R. E. White, "Single-particle model for a lithium-ion cell: Thermal behavior," *Journal of The Electrochemical Society*, vol. 158, no. 2, pp. A122–A132, 2011.

[60] W. B. Gu and C. Y. Wang, "Thermal-electrochemical modeling of battery systems," *Journal of The Electrochemical Society*, vol. 147, no. 8, pp. 2910–2922, 2000.

[61] K. Kumaresan, G. Sikha, and R. E. White, "Thermal model for a li-ion cell," *Journal of The Electrochemical Society*, vol. 155, no. 2, pp. A164–A171, 2008.

[62] M. Muratori, N. Ma, M. Canova, and Y. Guezennec, "A model order reduction method for the temperature estimation in a cylindrical li-ion battery cell," in *Proceedings of the ASME Dynamic Systems and Control Conference*, vol. 1, pp. 633–640, 2010.

[63] M. Muratori, M. Canova, and Y. Guezennec, "A spatially-reduced dynamic model for the thermal characterisation of li-ion battery cells," *International Journal of Vehicle Design*, vol. 58, no. 2-4, pp. 134–158, 2012.

[64] C. W. Park and A. K. Jaura, "Dynamic thermal model of li-ion battery for predictive behavior in hybrid and fuel cell vehicles," *SAE Transactions, Journal of Engines*, vol. 112, no. 3, pp. 1835–1842, 2003.

[65] C. Forgez, D. Vinh Do, G. Friedrich, M. Morcrette, and C. Delacourt, "Thermal modeling of a cylindrical $LiFePO_4$/graphite lithium-ion battery," *Journal of Power Sources*, vol. 195, no. 9, pp. 2961–2968, 2010.

[66] X. Lin, H. Perez, J. Siegel, A. Stefanopoulou, Y. Li, R. Anderson, Y. Ding, and M. Castanier, "Online parameterization of lumped thermal dynamics in cylindrical lithium ion batteries for core temperature estimation and health monitoring," *Control Systems Technology, IEEE Transactions on*, vol. 21, no. 5, pp. 1745–1755, 2013.

[67] S. Al Hallaj, H. Maleki, J. Hong, and J. Selman, "Thermal modeling and design considerations of lithium-ion batteries," *Journal of Power Sources*, vol. 83, no. 1-2, pp. 1–8, 1999.

[68] D. H. Jeon and S. M. Baek, "Thermal modeling of cylindrical lithium ion battery during discharge cycle," *Energy Conversion and Management*, vol. 52, no. 8-9, pp. 2973–2981, 2011.

[69] H. Maleki, S. A. Hallaj, J. R. Selman, R. B. Dinwiddie, and H. Wang, "Thermal properties of lithium-ion battery and components," *Journal of The Electrochemical Society*, vol. 146, no. 3, pp. 947–954, 1999.

[70] J. Shi, F. Wu, S. Chen, and C. Zhang, "Thermal analysis of rapid charging nickel/metal hydride batteries," *Journal of Power Sources*, vol. 157, no. 1, pp. 592–599, 2006.

[71] K. E. Thomas and J. Newman, "Thermal modeling of porous insertion electrodes," *Journal of The Electrochemical Society*, vol. 150, no. 2, pp. A176–A192, 2003.

[72] B. R. Jayasankar, A. Ben-Zvi, and B. Huang, "Identifiability and estimability study for a dynamic solid oxide fuel cell model," *Computers & Chemical Engineering*, vol. 33, no. 2, pp. 484–492, 2009.

[73] A. Ben-Zvi, P. J. McLellan, and K. B. McAuley, "Identifiability of non-linear differential algebraic systems via a linearization approach," *The Canadian Journal of Chemical Engineering*, vol. 84, no. 5, pp. 590–596, 2006.

[74] H. Pohjanpalo, "System identifiability based on the power series expansion of the solution," *Mathematical Biosciences*, vol. 41, no. 1-2, pp. 21–33, 1978.

[75] E. Walter and L. Pronzato, "On the identifiability and distinguishability of nonlinear parametric models," *Mathematics and Computers in Simulation*, vol. 42, no. 2-3, pp. 125–134, 1996.

[76] H. Khasawneh, J. Neal, M. Canova, Y. Guezennec, R. Wayne, J. Taylor, M. Smalc, and J. Norley, "Analysis of heat-spreading thermal management solutions for lithium-ion batteries," *ASME Conference Proceedings*, vol. 4, pp. 421–428, 2011.

[77] K. Onda, H. Kameyama, T. Hanamoto, and K. Ito, "Experimental study on heat generation behavior of small lithium-ion secondary batteries," *Journal of the Electrochemical Society*, vol. 150, no. 3, pp. A285–A291, 2003.

[78] X. Lin, A. G. Stefanopoulou, H. E. Perez, J. B. Siegel, Y. Li, and R. D. Anderson, "Quadruple adaptive observer of the core temperature in cylindrical li-ion batteries and their health monitoring," in *Proceedings of the American Control Conference*, (Montreal, Canada), pp. 578–583, Jun 27-29 2012.

[79] K. Smith, G.-H. Kim, and A. Pesaran, "Modeling of nonuniform degradation in large-format li-ion batteries," in *215th Electrochemical society meeting*, (San Francisco, California, USA), May 24-29 2009.

[80] A. Saltelli, K. Chan, and E. M. Scott, *Sensitivity analysis*, vol. 134. Wiley New York, 2000.

[81] K. Z. Yao, B. M. Shaw, B. Kou, K. B. McAuley, and D. Bacon, "Modeling ethylene/butene copolymerization with multi-site catalysts: Parameter estimability and experimental design," *Polymer Reaction Engineering*, vol. 11, no. 3, pp. 563–588, 2003.

[82] H. Maleki, J. Selman, R. Dinwiddie, and H. Wang, "High thermal conductivity negative electrode material for lithium-ion batteries," *Journal of Power Sources*, vol. 94, no. 1, pp. 26–35, 2001.

[83] K. Onda, T. Ohshima, M. Nakayama, K. Fukuda, and T. Araki, "Thermal behavior of small lithium-ion battery during rapid charge and discharge cycles," *Journal of Power Sources*, vol. 158, no. 1, pp. 535–542, 2006.

[84] A. Zukauskas, "Heat transfer from tubes in crossflow," in *Advances in Heat Transfer* (J. P. Hartnett and T. F. Irvine, eds.), vol. 8, pp. 93–160, Elsevier, 1972.

[85] E. A. Wan and A. T. Nelson, *Dual Extended Kalman Filter Methods*, pp. 123–173. John Wiley & Sons, Inc., 2002.

[86] D. R. Pendergast, E. P. DeMauro, M. Fletcher, E. Stimson, and J. C. Mollendorf, "A rechargeable lithium-ion battery module for underwater use," *Journal of Power Sources*, vol. 196, no. 2, pp. 793–800, 2011.

[87] S. Chen, C. Wan, and Y. Wang, "Thermal analysis of lithium-ion batteries," *Journal of Power Sources*, vol. 140, no. 1, pp. 111–124, 2005.

[88] K. Takano, Y. Saito, K. Kanari, K. Nozaki, K. Kato, A. Negishi, and T. Kato, "Entropy change in lithium ion cells on charge and discharge," *Journal of Applied Electrochemistry*, vol. 32, pp. 251–258, 2002.

[89] J. S. Hong, H. Maleki, S. Al Hallaj, L. Redey, and J. R. Selman, "Electrochemical-calorimetric studies of lithium-ion cells," *Journal of The Electrochemical Society*, vol. 145, no. 5, pp. 1489–1501, 1998.

[90] V. V. Viswanathan, D. Choi, D. Wang, W. Xu, S. Towne, R. E. Williford, J.-G. Zhang, J. Liu, and Z. Yang, "Effect of entropy change of lithium intercalation in cathodes and anodes on li-ion battery thermal management," *Journal of Power Sources*, vol. 195, no. 11, pp. 3720–3729, 2010.

[91] K. Jalkanen, T. Aho, and K. Vuorilehto, "Entropy change effects on the thermal behavior of a lifepo4/graphite lithium-ion cell at different states of charge," *Journal of Power Sources*, vol. 243, no. 0, pp. 354–360, 2013.

[92] Y. Kim, J. B. Siegel, and A. G. Stefanopoulou, "A computationally efficient thermal model of cylindrical battery cells for the estimation of radially distributed temperatures," in *Proceedings of the American Control Conference*, (Washington, DC, USA), pp. 698–703, Jun 17-19 2013.

[93] K. Boice, A. Leo, J. Lee, J. Paulson Jr, M. Skalny, and T. Valascho, "Baseline field testing of bb-2590 lithium-ion batteries using an irobot fastac 510 robot," tech. rep., TARDEC, 2010.

[94] L. Gao, S. Liu, and R. A. Dougal, "Dynamic lithium-ion battery model for system simulation," *Components and Packaging Technologies, IEEE Transactions on*, vol. 25, no. 3, pp. 495–505, 2002.

[95] A. Hammami, N. Raymond, and M. Armand, "Lithium-ion batteries: Runaway risk of forming toxic compounds," *Nature*, vol. 424, no. 6949, pp. 635–636, 2003.

[96] R. A. Leising, M. J. Palazzo, E. S. Takeuchi, and K. J. Takeuchi, "A study of the overcharge reaction of lithium-ion batteries," *Journal of Power Sources*, vol. 97-98, no. 0, pp. 681–683, 2001.

[97] J. Chen, C. Buhrmester, and J. R. Dahn, "Chemical overcharge and overdischarge protection for lithium-ion batteries," *Electrochemical and Solid-State Letters*, vol. 8, no. 1, pp. A59–A62, 2005.

[98] T. W. Asmus, "A manufacturer's perspective on ic engine technology at century's end," in *Proceedings of the Fall Technical Conference of the ASME Internal Combustion Engine Division*, vol. 1, pp. 1–10, 1999.

[99] F. Tavares, R. Johri, A. Salvi, S. Baseley, and Z. S. Filipi, "Hydraulic hybrid powertrain-in-the-loop integration for analyzing real-world fuel economy and emissions improvements," *in SAE 2011-01-2275*, 2011.

[100] J. Leuchter, V. Refucha, Z. Krupka, and P. Bauer, "Dynamic behavior of mobile generator set with variable speed and diesel engine," in *Proceedings of the Power Electronics Specialists Conference*, pp. 2287–2293, Jun 17-21 2007.

[101] M. Duoba, H. Ng, and R. Larsen, "Characterization and comparison of two hybrid electric vehicles (hevs) - honda insight and toyota prius," *in SAE 2001-01-1335*, 2001.

[102] L. B. Lave and H. L. MacLean, "An environmental-economic evaluation of hybrid electric vehicles: Toyota's prius vs. its conventional internal combustion engine corolla," *Transportation Research Part D: Transport and Environment*, vol. 7, no. 2, pp. 155–162, 2002.

[103] Oshkosh Defense, "HEMTT A3 diesel electric product sheet." `http://www.oshkoshdefense.com/products/12/hemtt-a3-diesel-electric#lit`. [Online; accessed 19-Nov-2013].

[104] Z. Filipi and Y. J. Kim, "Hydraulic hybrid propulsion for heavy vehicles: Combining the simulation and engine-in-the-loop techniques to maximize the fuel economy and emission benefits," *Oil & Gas Science and Technology - Revue d'IFP Energies nouvelles*, vol. 65, no. 1, pp. 155–178, 2010.

[105] M. Sorrentino, G. Rizzo, and I. Arsie, "Analysis of a rule-based control strategy for on-board energy management of series hybrid vehicles," *Control Engineering Practice*, vol. 19, no. 12, pp. 1433–1441, 2011.

[106] S. Yang, C. Qi, D. Guo, Y. Wang, and Z. Wei, "Topology optimization of a parallel hybrid electric vehicle body in white," *Applied Mechanics and Materials*, vol. 148-149, pp. 668–671, 2012.

[107] Z. Wei, Z. Qianfan, and C. Shumei, "Research on the dynamic performance and parameter design of parallel hybrid electric vehicle," *Advanced Materials Research*, vol. 108-111, pp. 613–618, 2010.

[108] J. Liu, J. Hagena, H. Peng, and Z. S. Filipi, "Engine-in-the-loop study of the stochastic dynamic programming optimal control design for a hybrid electric hmmwv," *International Journal of Heavy Vehicle Systems*, vol. 15, no. 2-4, pp. 309–326, 2008.

[109] Y. Li and N. Kar, "Advanced design approach of power split device of plug-in hybrid electric vehicles using dynamic programming," in *Proceedings of the IEEE Vehicle Power and Propulsion Conference*, pp. 1–6, Sep 6-9 2011.

[110] A. Ramasamy, A. M. Hill, A. E. Hepper, A. M. J. Bull, and J. C. Clasper, "Blast mines: Physics, injury mechanisms and vehicle protection," *JR Army Med Corps*, vol. 155, no. 4, pp. 258–264, 2009.

[111] A. Konev, L. Lezhnev, and I. Kolmanovsky, "Control strategy optimization for a series hybrid vehicle," *in SAE 2006-01-0663*, 2006.

[112] Y. Kim, T.-K. Lee, and Z. Filipi, "Frequency domain power distribution strategy for series hybrid electric vehicles," *SAE International Journal of Alternative Powertrains*, vol. 1, no. 1, pp. 208–218, 2012.

[113] G. Ripaccioli, D. Bernardini, S. Di Cairano, A. Bemporad, and I. Kolmanovsky, "A stochastic model predictive control approach for series hybrid electric vehicle power management," in *Proceedings of the American Control Conference*, pp. 5844–5849, Jun 30-Jul 2 2010.

[114] D. Rotenberg, A. Vahidi, and I. Kolmanovsky, "Ultracapacitor assisted powertrains: Modeling, control, sizing, and the impact on fuel economy," *Control Systems Technology, IEEE Transactions on*, vol. 19, no. 3, pp. 576–589, 2011.

[115] G. L. Plett, "Extended kalman filtering for battery management systems of lipb-based {HEV} battery packs: Part 3. state and parameter estimation," *Journal of Power Sources*, vol. 134, no. 2, pp. 277–292, 2004.

[116] Y. Kim, S. Mohan, J. B. Siegel, A. G. Stefanopoulou, and Y. Ding, "The estimation of radial temperature distribution in cylindrical battery cells under unknown cooling conditions," in *IEEE Conference on Decision and Control*, (Firenze, Italy), Dec 10-13 2013.

[117] M. C. VanDyke, J. L. Schwartz, and C. D. Hall, "Unscented kalman filtering for spacecraft attitude state and parameter estimation," in *Proceedings of the 14th AAS/AIAA Space Flight Mechanics Meeting*, pp. 217–228, Feburary 2004.

[118] G. Nagasubramanian, "Electrical characteristics of 18650 li-ion cells at low temperatures," *Journal of Applied Electrochemistry*, vol. 31, no. 1, pp. 99–104, 2001.

[119] S. Zhang, K. Xu, and T. Jow, "The low temperature performance of li-ion batteries," *Journal of Power Sources*, vol. 115, no. 1, pp. 137–140, 2003.

[120] J. Fan, "On the discharge capability and its limiting factors of commercial 18650 li-ion cell at low temperatures," *Journal of Power Sources*, vol. 117, no. 1–2, pp. 170–178, 2003.

[121] L. Liao, P. Zuo, Y. Ma, X. Chen, Y. An, Y. Gao, and G. Yin, "Effects of temperature on charge/discharge behaviors of lifepo4 cathode for li-ion batteries," *Electrochimica Acta*, vol. 60, no. 0, pp. 269–273, 2012.

[122] C. K. Huang, J. S. Sakamoto, J. Wolfenstine, and S. Surampudi, "The limits of low-temperature performance of li-ion cells," *Journal of The Electrochemical Society*, vol. 147, no. 8, pp. 2893–2896, 2000.

[123] Y. Ji and C. Y. Wang, "Heating strategies for li-ion batteries operated from subzero temperatures," *Electrochimica Acta*, vol. 107, no. 0, pp. 664–674, 2013.

[124] Q. Zhang and R. E. White, "Capacity fade analysis of a lithium ion cell," *Journal of Power Sources*, vol. 179, no. 2, pp. 793–798, 2008.

[125] K. S. Ng, C.-S. Moo, Y.-P. Chen, and Y.-C. Hsieh, "Enhanced coulomb counting method for estimating state-of-charge and state-of-health of lithium-ion batteries," *Applied Energy*, vol. 86, no. 9, pp. 1506–1511, 2009.

[126] Y. Zhang, C.-Y. Wang, and X. Tang, "Cycling degradation of an automotive lifepo4 lithium-ion battery," *Journal of Power Sources*, vol. 196, no. 3, pp. 1513–1520, 2011.

[127] M. Verbrugge and E. Tate, "Adaptive state of charge algorithm for nickel metal hydride batteries including hysteresis phenomena," *Journal of Power Sources*, vol. 126, no. 1-2, pp. 236–249, 2004.

[128] J. Kim and B. H. Cho, "State-of-charge estimation and state-of-health prediction of a li-ion degraded battery based on an ekf combined with a per-unit system," *Vehicular Technology, IEEE Transactions on*, vol. 60, no. 9, pp. 4249–4260, 2011.

[129] M. Ecker, J. B. Gerschler, J. Vogel, S. Käbitz, F. Hust, P. Dechent, and D. U. Sauer, "Development of a lifetime prediction model for lithium-ion batteries based on extended accelerated aging test data," *Journal of Power Sources*, vol. 215, no. 0, pp. 248–257, 2012.

[130] U. Tröltzsch, O. Kanoun, and H.-R. Tränkler, "Characterizing aging effects of lithium ion batteries by impedance spectroscopy," *Electrochimica Acta*, vol. 51, no. 8-9, pp. 1664–1672, 2006.

[131] J. Li, E. Murphy, J. Winnick, and P. Kohl, "Studies on the cycle life of commercial lithium ion batteries during rapid charge–discharge cycling," *Journal of Power Sources*, vol. 102, no. 1-2, pp. 294–301, 2001.

[132] D. Abraham, E. Reynolds, E. Sammann, A. Jansen, and D. Dees, "Aging characteristics of high-power lithium-ion cells with $LiNi_{0.8}Co_{0.15}Al_{0.05}O_2$ and $Li_{4/3}Ti_{5/3}O_4$ electrodes," *Electrochimica Acta*, vol. 51, no. 3, pp. 502–510, 2005.

[133] R. Kostecki and F. McLarnon, "Microprobe study of the effect of li intercalation on the structure of graphite," *Journal of Power Sources*, vol. 119-121, no. 0, pp. 550–554, 2003.

[134] J. Christensen and J. Newman, "Stress generation and fracture in lithium insertion materials," *Journal of Solid State Electrochemistry*, vol. 10, no. 5, pp. 293–319, 2006.

[135] J. Cho, Y. J. Kim, T.-J. Kim, and B. Park, "Zero-strain intercalation cathode for rechargeable li-ion cell," *Angewandte Chemie*, vol. 113, no. 18, pp. 3471–3473, 2001.

[136] J. Cannarella and C. B. Arnold, "Stress evolution and capacity fade in constrained lithium-ion pouch cells," *Journal of Power Sources*, vol. 245, no. 0, pp. 745–751, 2014.

[137] T. Ersal, M. Brudnak, A. Salvi, J. L. Stein, Z. Filipi, and H. K. Fathy, "Development and model-based transparency analysis of an internet-distributed hardware-in-the-loop simulation platform," *Mechatronics*, vol. 21, no. 1, pp. 22–29, 2011.

[138] T. Ersal, M. Brudnak, J. L. Stein, and H. K. Fathy, "Statistical transparency analysis in internet-distributed hardware-in-the-loop simulation," *Mechatronics, IEEE/ASME Transactions on*, vol. 17, no. 2, pp. 228–238, 2012.

[139] T. Ersal, R. B. Gillespie, M. Brudnak, J. L. Stein, and H. Fathy, "Effect of coupling point selection on distortion in internet-distributed hardware-in-the-loop simulation," *International Journal of Vehicle Design*, vol. 60, 2012.

[140] Y. Kim, A. Salvi, A. G. Stefanopoulou, and T. Ersal, "Reducing soot emissions in a diesel series hybrid electric vehicle using a power rate constraint map," *Vehicular Technology, IEEE Transactions on, submitted*.

[141] S. Onori, P. Spagnol, V. Marano, Y. Guezennec, and G. Rizzoni, "A new life estimation method for lithiumion batteries in plugin hybrid electric vehicles applications," *International Journal of Power Electronics*, vol. 4, no. 3, pp. 302–319, 2012.

[142] J. R. Hagena, Z. S. Filipi, and D. N. Assanis, "Transient diesel emissions: Analysis of engine operation during a tip-in," *in SAE 2006-01-1151*, 2006.

[143] R. Johri, A. Salvi, and Z. Filipi, "Real-time transient soot and NOx virtual sensors for diesel engine using neuro-fuzzy model tree and orthogonal least squares," *Journal of Engineering for Gas Turbines and Power*, vol. 134, no. 9, 2012.

[144] Y. Zhu, Y. Chen, G. Tian, H. Wu, and Q. Chen, "A four-step method to design an energy management strategy for hybrid vehicles," in *Proceedings of the American Control Conference*, vol. 1, pp. 156–161, Jun 30-Jul 2 2004.

[145] M. Montazeri-Gh, A. Poursamad, and B. Ghalichi, "Application of genetic algorithm for optimization of control strategy in parallel hybrid electric vehicles," *Journal of the Franklin Institute*, vol. 343, no. 4-5, pp. 420–435, 2006.

[146] V. Paladini, T. Donateo, A. de Risi, and D. Laforgia, "Super-capacitors fuel-cell hybrid electric vehicle optimization and control strategy development," *Energy Conversion and Management*, vol. 48, no. 11, pp. 3001–3008, 2007.

[147] Z. Wang, B. Huang, Y. Xu, and W. Li, "Optimization of series hybrid electric vehicle operational parameters by simulated annealing algorithm," in *Proceedings of the IEEE International Conference on Control and Automation*, pp. 1536–1541, May 30-Jun 1 2007.

[148] J. Ryu, Y. Park, and M. Sunwoo, "Electric powertrain modeling of a fuel cell hybrid electric vehicle and development of a power distribution algorithm based on driving mode recognition," *Journal of Power Sources*, vol. 195, no. 17, pp. 5735–5748, 2010.

[149] L. Fang, S. Qin, G. Xu, T. Li, and K. Zhu, "Simultaneous optimization for hybrid electric vehicle parameters based on multi-objective genetic algorithms," *Energies*, vol. 4, no. 3, pp. 532–544, 2011.

[150] Argonne National Laboratory, "Powertrain systems analysis toolkit." `http://www.transportaion.anl.gov/software/PSAT`, 2002. [Online; accessed 19-Nov-2013].